Multiphase Flow Measurement with Electrical Capacitance Tomography and Microwave Sensors

A thesis submitted to The University of Manchester for the degree of Doctor of Philosophy

in the Faculty of Science and Engineering

2017

Mimi Faisyalini Ramli

School of Electrical and Electronic Engineering

Table of contents

List of figures

List of tables

Acronyms and symbols

Acronyms:

AC	Alternating Current
ADC	Analog Digital Converter
CAPM	Computer Aided Permittivity Measurement
CFB	Circulating Fluidised Bed
DC	Direct Current
ECT	Electrical Capacitance Tomography
EIT	Electrical Impedance Tomography
EMT	Electromagnetic Tomography
ERT	Electrical Resistance Tomography
FDA	Food and Drug Administration
FDM	Finite Different Method
FEM	Finite Element Method
GUI	Graphic User Interface
GPU	Graphic Processing Unit
GVF	Gas-Volume-Fraction
IET	Institute of Engineering Thermophysics
LBP	Linear Back Projection
MFM	Multiphase Flow Metering
MRS	Microwave Cavity Resonant Sensor
MWT	Microwave Tomography
NEL	National Engineering Lab
PDE	Partial Differential Equation
PVC	Polyvinyl chloride
SMB	Sub Miniature version B
SNA	Scalar Network Analyser
SNR	Signal-to-noise ratio
SVD	Singular Value Decomposition
TE	Transverse Electric
TM	Transverse Magnetic

TV	Total Variation
UHF	Ultra-High Frequency
VHF	Very High Frequency
VNA	Vector Network Analyser
WLR	Water-in-Liquid Ratio

Symbols:

M	number of independent measurement
N	number of electrodes
ε	permittivity of the material
$\varepsilon(x, y)$	permittivity distribution at (x,y)
$\phi(x, y)$	potential distribution at (x,y)
Γ	electrode surface
C	inter-electrode capacitance
Q	electric charge
V	voltage between excitation and detection electrode
$S_{i,j}(x, y)$	sensitivity map between electrode i and j at (x,y)
$E(x, y)$	electric field distribution at (x,y)
V_i	excitation voltage
$p_{(x,y)}$	area of the pixel at (x,y)
C_{norm}	normalised capacitance
S	normalised sensitivity matrix
g	normalised permittivity distribution
C_H	capacitance of the sensor filled with high permittivity material
C_L	capacitance of the sensor filled with low permittivity material
C_m	measured capacitance (sensor filled with test material/test flow regime)
S^{-1}	inverse sensitivity matrix
S^T	transpose sensitivity matrix
$\hat{g}$	estimated permittivity distribution
$u_{C_{norm}}$	identity vector
$\hat{g}_k$	estimated permittivity distribution at k-th iteration

$\hat{g}_0$	initial estimated permittivity distribution
k, k+1	iteration number
α	relaxation factor
μ	permeability of material
c	speed of light (3x10^8 m/s)
f_r	resonant frequency
$f_{r(th)}$	threshold value for resonant frequency
m,n,l	number of variations in the standing wave pattern in x, y and z directions
p'_{nm}	cut-off wavenumber of TE_{nm} wave mode in cylindrical waveguide
p_{nm}	cut-off wavenumber of TM_{nm} wave mode in cylindrical waveguide
χ	dielectric contrast
χ_k	dielectric contrast, χ at k-th iteration
E^S	scattered electric field
$F(\chi)$	complex nonlinear vector function of χ
E^S_{meas}	measured scattered electric field
E^S_k	scattered electric field at k-th iteration
$\delta\chi_k$	incremental of χ at k-th iteration
$\tilde{g}$	normalised real permittivity distribution
$\bar{\tilde{g}}$	mean values of $\tilde{g}$
$\bar{g}$	mean values of $\hat{g}$
N_p	number of pixel
$d(r,m), d(m,r)$	Euclidean distance between point m and r
m, r	points in Euclidean space
t	number of measurement between the points in the Euclidean space
T_x	transmitter
R_x	receiver
σ	conductivity

Abstract

As electrical capacitance tomography (ECT) is inexpensive, non-invasive and non-intrusive, it has become one of the most established tomography modalities. However, ECT is currently being used only for low permittivity dielectric and non-conductive material in the oil-continuous flow. This is the first time in research that the capacitance sensor is proposed to be integrated with a microwave sensor to measure the parameters of a multiphase flow. The two presented dual-modality systems are (1) ECT and microwave cavity resonant sensor (MRS) and (2) ECT and microwave tomography (MWT).

For oil and gas application, a dual modality system of 8-electrode ECT and MRS has been developed for two purposes to (1) identify flow pattern and (2) estimate water-in-liquid ratio (WLR). Rather than using a tomographic reconstruction, a simpler technique of signal processing and characterisation based on the capacitance and resonant frequency data is implemented. The system demonstrates a 100% compliance of detecting stratified and annular flows for 18 tested conditions. The initial estimation of WLR is reasonable with the majority of the conditions resulted in less than 5% error. This dual-modality is advantageous as it works for both oil-continuous and water-continuous flows and minimises flow-regime-dependency. In addition, this new dual-modality system is non-radiation, non-intrusive and non-invasive.

A 12-electrode ECT sensor and an MWT have been designed for the fluidised bed application to (1) image permittivity distribution and (2) investigate the effects of higher moisture content on solids concentration images. For image reconstruction with ECT, sensitivity map evaluation was first conducted to justify whether a sensitivity map according to the test material should be updated. The results show that a generic sensitivity map generated with an empty background is appropriate to reconstruct images for most defined distributions except for an annular flow with a thin layer. Experiments with a dual-modality system of ECT and MWT were then carried out to image gas, powder and liquid. The result shows 50% complementary function of ECT and MWT, indicating that good images can be obtained with MWT at higher moisture content.

Declaration

No portion of the work referred to in the thesis has been submitted in support of an application for another degree or qualification of this or any other university or other institute of learning.

Copyright statement

Acknowledgements

This work was written in faith, and with advice and help from many people.

First of all, I would like to express my heartfelt gratitude to my supervisor, Professor Wuqiang Yang for all the knowledge, time, continuous guidance and encouragement.

Thank you to Professor Haigang Wang from the Institute of Engineering Thermophysics (IET), Chinese Academy of Sciences, Beijing, China and to Professor Fernando Rangel de Sousa from the Federal University of Santa Catarina , Brazil for the generous help and collaborations.

Special thanks to my colleagues and dear friends for the fruitful discussions, and for being with me through thick and thin.

I also gratefully thank Majlis Amanah Rakyat Malaysia (MARA) for the funding.

Last but not least, my deepest appreciation goes to my beloved parents, Pn. Hjh. Rosemini Joji and Tn. Hj. Ramli Hambali, and to my brothers and sisters, for their unconditional love and endless support. I could not have done it without you.

Thank you.

Publications from this work

[1] Ramli M F, Tian W and Yang W Q (2016), Image Reconstruction with Different Sensitivity Maps Generated with Different Background, *in 2016 IEEE International Conference on Imaging Systems and Techniques*, 4-6 October, Chania, Greece, pp. 543-548 (Best Student Paper Presentation)

[2] Wang H G, Zhang J L, Ramli M F, Mao M X, Ye J M, Yang W Q and Wu Z P (2016), Imaging wet granules with different flow patterns by electrical capacitance tomography and microwave tomography, *Meas. Sci. Technol.,* (27), pp. 1-12

[3] Wang H G, Zhang J L, Mao M X, Ye J M, Ramli M F, Yang W Q and Wu Z P (2015), Image reconstruction for wet granules by electrical capacitance and microwave tomography, *in IEEE International Conference on Imaging Systems and Techniques*, 16-18 Sept., Macau, China, pp. 1-6

[4] Tian W, Sun J, Ramli M F and Yang W Q (2016), An Electrical Capacitance Tomography Sensor with Variable Diameter, *IEEE Sensors Journal*, 17(7), pp. 2089-2099

[5] Tian W, Sun J, Ramli M F and Yang W Q (2016), Effect of electrode-to-gap ratio on electrical capacitance tomography images, *in 2016 IEEE International Conference on Imaging Systems and Techniques*, 4-6 October, Chania, Greece, pp. 294-299

Chapter 1: Introduction

This thesis is to explore the potential of the dual-modality systems of electrical capacitance tomography (ECT) and microwave sensors, in particular for the oil and gas, and pharmaceutical industries. This Chapter aims to briefly introduce the background and the motivations for the research. The aims and objectives are presented in a later section, and the organisation of the research is given in the final section.

1.1 Multiphase flow

Prior to commencing the investigation of the multiphase metering techniques and capabilities, it was necessary to first have a clear understanding of the essence of the multiphase flow. Multiphase flow occurs ubiquitously, in nature or in many industrial fields. The blood flow in the human body, the existence of bubbles and sand in river stream and steam condensation on windows are examples of multiphase flow that occur naturally. It is also widely encountered in the petroleum industry, medicines and pharmaceutical, food, chemical, cosmetics, nuclear reactor industry and geothermal energy plants.

Typically, multiphase flow in petroleum industry is composed of three components: gas, liquid and solid. The most common classes of the multiphase flow are the two-phase flow and three-phase flow, which occur with the two and three combinations of the above-mentioned single phases. In reality, the behaviour and shape of the phases in multiphase flow determine the flow pattern, known as the 'flow regime'. There are various types of flow regimes, but some of the usual ones are stratified, annular, bubbles, slug or plug flow. In general, there are several common factors that dictate the flow patterns such as phase properties, fractions, velocities and whether a flow is in a steady-state, pseudo steady-state or transient multiphase flow. The flow regime is also strongly influenced by the flow structure, i.e. the pipe layout, diameter, shape, inclination, bends and junctions. For example, a two-phase flow of gas-liquid in a horizontal pipe can change from stratified to annular flow with an upward pipe inclination of -80^{o}. The formation of flow regime is also affected by the operation setup, such as pressure or temperature (Falcone *et al.*, 2010).

The transition of multiphase flow can occur at any point in a production process, regardless of whether the formation is desired or not. Therefore, in many applications, it is crucial to measure and keep the flow under control so that the efficiency of the process and the quality of the products are assured. The types of multiphase flow which are of interests in this research are gas-liquid, gas-solid, liquid-solid (two-phase flow) and gas-liquid-liquid (three-phase flow) for the oil and gas, and pharmaceutical industries.

1.2 Multiphase flow metering (MFM) for oil and gas industry

In the oil and gas industry, the most common phase to consider is gas, oil and water since sand has been normally filtered during the early stage of the process. The behaviour of this multiphase flow travelling in the pipe is complicated; therefore, it remains the greatest challenge in multiphase flow metering to accurately determine the flow regime and its parameters. Some typically used MFM techniques are based on electrical properties (impedance), microwaves, gamma-ray attenuation, differential pressures and cross-correlation. For a multiphase flow, one technique or a single modality on its own is not sufficient to determine the flow rates, therefore a dual-modality must be used.

To understand multiphase flow, the flow regime must first be identified. Only then, other related parameters such as flow rate, phase fraction and velocity can be derived. An industrial high-speed camera can be used to define the flow regime, but this visual method does not work with non-transparent conduits or pipes. A more recent solution is the tomography technique that displays the cross-sectional image of a test area without the need of a 'can-see-through' envelope (Pradeep, 2015). The system can be either a radiation or non-radiation based. Some mature tomography techniques can also be used to estimate phase fraction measurements such as the water-in-liquid ratio (WLR) and gas-volume-fraction (GVF). These parameters are important for operational purposes. The electrical capacitance tomography (ECT), electrical resistance tomography (ERT) and microwave tomography (MWT) are a few examples of non-radiation tomography systems, while gamma-ray and X-ray are examples of radiation-based methods. The fact that the process tomography is non-invasive has made it very attractive.

For the phase fraction measurement, most commercialised instruments implement the gamma-ray and impedance-based techniques. The impedance technique is safe, simple and robust but very sensitive to change in flow regime. It normally requires a specific calibration for a specific range of measurement; therefore a new calibration is always required if the permittivity or conductivity of the monitored phase is changed. A few microwave-based flow meters are reported available to estimate water fraction. However, they require partial separation as a part of the measurement process.

Each of the multiphase flow meters has their own constraints and limitations. The capacitive meter (including the ECT) works very well in oil-continuous flow but not in water-continuous flow in contrary to the way that resistive-based (including the ERT) works. An extended microwave-based technique that measures resonant frequency was reported of having the capability to measure WLR of the oil-water mixture in a full-phase range by (Thorn *et al.*, 2013; Xie, 2007); however, it serves only as a water-cut meter and is not able to detect the flow pattern. Gamma-ray has been a widely used technique in inline MFM, but these days, using a nucleonic/radiation-based instrumentation has become difficult as some countries have restricted the use of radioisotope due to health and safety concerns (Thorn *et al.*, 2013).

One approach that researchers have proposed to improve the performance of MFM is by developing a dual-modality system. Analyses in this research are based on the electrical capacitance and microwave sensors. The ECT in this research is proposed to be used alongside with the microwave cavity resonant sensor (MRS) as a dual-modality system to identify the flow pattern and to measure WLR. Other than being used as a tomographic system, a simpler signal processing method is implemented to analyse and make full use of the capacitance and resonant frequency data. The combination of these two systems, which provide complementary information, is foreseen to enhance the overall system to be more attractive and useful.

1.3 Multiphase flow metering (MFM) for pharmaceutical industry

The pharmaceutical industry discovers, develops, produces and markets drugs for medical purposes. The development and production of drugs are complex, expensive and must comply with strict regulations and standards set by professional bodies such as the Food and Drug Administration (FDA) and the Medicines and Healthcare Products

Regulatory Agency, UK. Drugs are commonly produced in liquid or tablet forms. In this research, the focus is on the process of producing the tablet form that is manufactured using a sophisticated machine called the fluidised bed. The two leading manufacturers supplying the fluidised bed and the services are the Glatt, Deutschland and GEA, Germany. Figure 1.1 shows an example of the fluidised bed available in the market.

The fluidised bed is commonly used for batch processing of solid particles for drying, coating and granulating. The main advantage of using the fluidised bed is that it provides efficient heat and mass transfer and is able to mix excipients and active materials to produce a uniformed blend of particles (Walker *et al.*, 2009). Granulation or agglomeration is a process to produce granules from powder using liquid bridges. Water or organic solvent is sprayed on the powder to wet and agglomerate the particles and turns them into granules. The moistened granules are then dried to increase their shelf-life. It is also a normal practice to get the granules coated. The coating process involves liquid spraying and crystallisation to form a protective film on the surface of the granules, and the coating must absolutely seal the granules without any cracks or mechanical damages (Wang *et al.*, 2016, Glatt, 2014).

Figure 1.1 GLATT WS Combo (Glatt, 2014)

Currently, the most serious problem encountered in the fluidised bed process is the occurrence of undesired agglomeration. This occurs because, at a high temperature and moisture, particles tend to adhere to each other and form larger entities (Naelapa *et al.*, 2007). The undesired entities can also stick easily onto the hot wall, and this causes faulty drying which leads to over-wetting or over-drying of products. Hence, it is crucial to implement a technology to monitor the distribution not only for fault diagnosis but also to control the fluidised bed conditions. The moisture content of granules in fluidised bed drying, granulating and coating processes can typically be between

1%~25%, resulting in the change of the permittivity and conductivity during the process. An ECT can be used to measure the change in permittivity but not to measure the change in conductivity in the gas-solid two-phase flow (Yang, 2010, Wang *et al*., 2016, Thamae and Wu, 2010). An ERT may be used to measure conductivity; however, as the metallic electrodes of the ERT are required to be in contact with the object to image, this method is not approved by the FDA. Therefore, a new approach to measure complex permittivity needs to be developed. One possibility proposed in this research is to develop a dual-modality of ECT and microwave tomography (MWT) to image permittivity distribution of different materials, and also to image solid distribution at low and high water contents, in particular in between 1% and 30% for the fluidised bed operation.

1.4 Aim and objectives

The research aims to explore the potential of ECT and microwave sensors with different flow regimes and on different materials for different kind of application. The ultimate goal is to integrate both functions to become a powerful dual-modality system that works for both oil-continuous and water-continuous flow so that the system can provide more useful information. The specific objectives of the research are as follows:

Dual-modality of ECT and MRS

1. to design the ECT sensor;
2. to evaluate the individual systems (ECT and MRS) in;
    a. identifying flow pattern, stratified or annular;
    b. estimating water-in-liquid ratio (WLR);
3. to integrate both functions (ECT and MRS);
4. to evaluate the performance of the new dual-modality system;

Appraisal of the sensitivity maps

5. to evaluate sensitivity maps generated with different backgrounds and their effects on the image reconstruction. This is a prior justification for using ECT for the dual-modality of ECT and MWT;

Dual-modality of ECT and MWT

6. to reconstruct different flow patterns of materials with ECT and MWT;
7. to study the effects of moisture on image reconstruction;
8. to compare the quality of images between the two systems.

1.5 Contributions

The main contributions of this work are as follows:

Dual-modality of ECT and MRS

This Chapter presents the first integration of ECT and MRS functions in identifying flow regime and estimating WLR of gas and liquid (emulsion) multiphase flow. The major benefit of this work is that it improves the measurement capabilities of the traditional single modality sensor (ECT or MRS) system. The results demonstrate the feasibility of developing a dual-modality system that is non-intrusive, non-invasive and non-radiation, to identify flow regime and estimate WLR in full range, from oil-continuous to water-continuous flow.

Appraisal of the sensitivity maps

This Chapter describes the generation of sensitivity maps with different backgrounds (different permittivity) and evaluates their effect on image reconstructions in comparison to the generic sensitivity map obtained with an empty background. The work is important as it helps in making a decision as to whether or not different sensitivity maps should be used for imaging different materials and flow regimes. There are more options of sensitivity maps to suit the applications rather than only one generic sensitivity map for all cases.

Dual-modality of ECT and MWT

This Chapter proposes a new method of imaging complex solids distribution at low and high moisture by combining ECT and MWT functions. The results can be used to develop a process control in fluidised bed drying, coating and granulating process to improve operational efficiency.

1.6 Organisation of the thesis

In the beginning of this Chapter, the background, motivation, objectives and contributions from this work to the research field are briefly introduced.

Chapter 2 reviews the fundamentals of ECT including the basic principles, features, solutions for the problems presented and the reconstruction of algorithms.

Chapter 3 presents the theoretical background and operation of microwave sensors, focusing on MRS and MWT.

Chapter 4 explores the potential of the dual-modality system of ECT and MRS in identifying flow regimes and estimating WLR in oil-continuous and water-continuous flows.

Chapter 5 evaluates sensitivity maps generated with different backgrounds and the impact on image reconstruction.

Chapter 6 investigates the effects of flow regimes and moisture on images reconstructed by ECT and MWT

Chapter 7 provides the conclusions drawn from this research and suggestions for future work.

Chapter 2: Electrical capacitance tomography

ECT has been developed for many years and has become the most established electrical tomographic technique compared to other modalities such electrical resistance/impedance tomography (ERT/EIT) and electromagnetic tomography (EMT). Unlike other conventional tomographic techniques, ECT is low cost, non-radiation, non-invasive and non-intrusive.

Research into ECT has been actively conducted in academic institutions such as at the University of Manchester (formerly UMIST), the University of Bergen in Norway, Tsinghua University in China, the Delft University of Technology in Netherlands, Hannover University in Germany, Warsaw University in Poland, Institute Mexico Petroleum in Mexico, and Morgantown in the USA (Yang, 1996; Yang and Peng, 2003). The University of Manchester has been leading the research in ECT since the early 1980s with remarkable findings and inventions. The first real-time ECT system that successfully generated images of gas/oil flows in a pipeline was developed in collaboration with Schlumberger Cambridge Research Ltd (Yang *et al*., 2011). The research on ECT has also been extensively carried out in research centres, for example, the TUV NEL in the UK. TUV NEL is a world-class provider of technical consultancy**,** research, testing, flow measurement and programme management services. Under DTI Flow Programme (1999-2002), TUV NEL did a project of evaluating new technology for high accuracy multiphase flow measurement involving ECT (TUV NEL, 2003).

ECT can provide spatial distribution and measure two-phase flows for many applications, such as gas/oil flows in pipelines. (Xie *et al.*, 1992) designed a 12-electrode ECT sensor and used finite-element model to calculate capacitance field sensitivity and to reconstruct images for various gas/oil flow distribution. This research introduced adaptive threshold operation for its linear back projection algorithm, that can reduce the artefacts of the grey level thus a good quality of images can be obtained. In another research conducted by (Yang *et al.*,1995), a PC-based 8-electrodes and a transputer-based 12-electrodes ECT systems were described. The comparison between the two systems showed that the 12-electrodes system is fast, and can improve the image resolution. An example of more recent research was conducted by (Li *et al.,*

2013). Their work presented a model-based image reconstruction for the ECT system to measure liquid fraction and to derive WLR of an annular liquid layer. The result from this research showed that the ECT is capable to accurately estimate WLR up to only 35%, with an uncertainty ≤ ±3%.

ECT has also been used for wet gas separator process. For the first time in research, (Yang *et al.,* 2002) in collaboration with Shell Global Solutions Ltd (UK) and Twister B.V presented the first experimental results, showed that water droplets distribution in the gas stream can be imaged by ECT. An 8-electrode LCR meter based ECT system was developed and used for static test and on Twister simulator. Although at this point, the obtained images were still qualitative but the robustness of the ECT system offers the possibility of field application on Twister. Another research on visualising water droplet distribution was carried out with an impedance analyser based ECT system. This research used adaptive calibration and adjacent electrode pair correction techniques to image very low concentration profile. It was demonstrated that the ECT is capable of reconstructing clear image. The sensor was very sensitive that changes as small as 1 gWater/kgAir was detectable (Yang *et al.*, 2004).

In the pharmaceutical industry, the ECT was employed to measure gas/solids flows in fluidised beds. (Liu *et al*., 2005) discovered a non-intrusive technique for measuring axial and angular velocities for circulating fluidised bed (CFB) and cyclone separator. They introduced velocity measurement by cross-correlation that was non-invasive, simple, fast and inexpensive. The system used an algorithm for 3D images and performed online image reconstruction. The material near the wall where the ECT was installed was easier to be detected than the material in the centre region. This is concluded due to uneven distribution of the sensitivity. The first attempt to use ECT for online solid moisture measurement was done by (Wang *et al.*, 2009). A twin-plane ECT with 8 electrodes in each plane was mounted on the fluidised bed dryer. The measured moisture was used as an input to a feedback control system and the results revealed that measurement of solids moisture by ECT is feasible with ECT. Other examples of research on ECT for fluidised bed are carried out by (Wang and Yang, 2010) and (Wang *et al.*, 2008). However, none of the above research used ECT to measure materials with high water content.

Some other applications that use ECT are such as in pneumatic conveyors, combustion flame in a car engine (Waterfall *et al.*, 1997), food processing, paper and plastic production, solids waste treatment and chemical engineering (Yang and Liu, 2000).

2.1 Overall system and measurement strategy

Figure 2.1 shows a typical set-up for an ECT system that consists of an ECT sensor, a measurement circuit and a computer. The ECT sensor is connected to the measurement circuit with individual cable for each of the electrodes surrounding the sensing area. The measurements are gathered by the measuring circuit and the capacitance data are then used for image reconstruction performed by the computer.

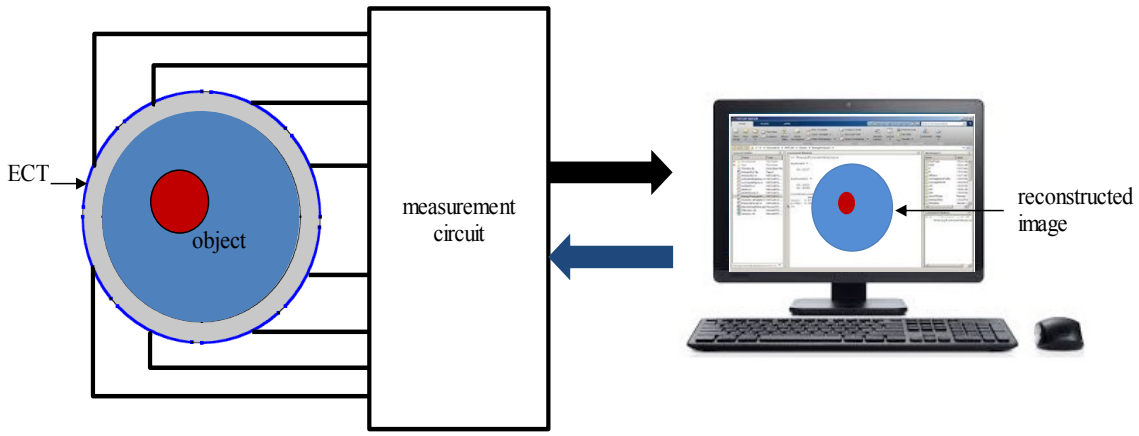

Figure 2.1: ECT System

ECT uses capacitance data obtained between excitation and detection electrode to visualise material distribution and hence flow patterns. Figure 2.2 illustrates the cross section of an ECT sensor with 8 electrodes mounted circumferentially on the external wall of a pipe or vessel. The material of the pipe must be non-conductive, such as glass, Perspex or PVC. The capacitance is measured for all possible electrode pairs. Normally, one electrode is assigned as an excitation electrode while the rest electrodes are in ground or virtual ground as detection electrodes. The corresponding capacitance is measured from each detection electrode. As an example, when electrode 1 is excited, electrodes 2 to 8 are in ground. The capacitance is measured for individual pairs between electrode 1 and the grounded electrodes (electrode 2,3….8). This process is repeated until electrode 7 is selected as excitation electrode and electrode 8 as detection electrode. In this way, an 8-electrode ECT sensor has a maximum 28 independent

measurements (Yang *et al.*, 1995). The total number of independent measurement is expressed by

$$M = \frac{N(N-1)}{2} \tag{2.1}$$

where N is the number of electrodes.

The matrix of the electrode pair measurement is shown in Table 2.1.

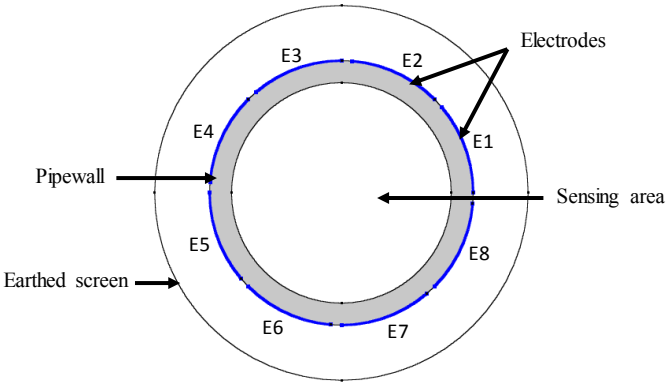

Figure 2.2: Cross section of 8-electrode ECT sensor

Table 2.1: Electrode pair measurement

E1 - E2	**E2 - E3**	**E3 - E4**	**E4 - E5**	**E5 - E6**	**E6 - E7**	**E7 - E8**
E1 - E3	**E2 - E4**	**E3 - E5**	**E4 - E6**	**E5 - E7**	**E6 - E8**	
E1 - E4	**E2 - E5**	**E3 - E6**	**E4 - E7**	**E5 - E8**		
E1 - E5	**E2 - E6**	**E3 - E7**	**E4 - E8**			
E1 - E6	**E2 - E7**	**E3 - E8**				
E1 - E7	**E2 - E8**					
E1 - E8						

2.2 ECT sensor design

The design of the ECT sensor plays an important role to ensure successful measurement. There are several key guidelines on how to choose the most appropriate design parameters to fit in with a specific application, such as the characteristic of the electrodes, the sensor shape, the driven guard and the earthed screen.

2.2.1 Electrodes

The electrodes are the main components of the sensor. The electrodes are used to measure change in capacitance with the change of permittivity. Therefore, one must carefully design the electrodes and consider its main character, such as the number of electrodes, the length of electrodes and location of electrodes to obtain useful results. The electrodes can be made of many types of metallic material, such as brass plate (Huang *et al.*,1989) and copper adhesive tape (Xie *et al.*, 1989).

a. ***Number of electrodes***

In ECT design, the number of electrodes affects the capacitance value, spatial resolution, data acquisition rate, circuitry complexity, and the cost of the hardware (Yang, 1997). The number of electrodes determines the number of independent measurements, as expressed by equation (2.1). A large number of electrodes can produce more independent measurements. Hence, on a fixed pipe circumference with the increased number of electrodes, an improved image resolution can be expected. However, too many electrodes would cause difficulties, such as (1) too small inter-electrode capacitance, (2) less sensitivity due to huge eigenvalues of the sensitivity matrix, (3) a slower rate of data acquisition and (4) expensive hardware. A smaller number of electrodes has the advantageous of (1) simpler hardware, (2) faster data acquisition and (3) suitable for shorter electrodes for limited space or thin measurement area due to the increased cover angle. Obviously, a smaller number of electrodes results in a smaller number of independent measurements. Therefore, a good image cannot be expected. (Peng *et al.,* 2012) worked on the effect of the number of electrodes on the sensor system. Currently, the most applicable number of electrodes used in ECT systems are 8 or 12 (Yang, 2010).

b. Length of electrodes

This parameter plays a major role in the success of image reconstruction with ECT. To decide the length of the electrodes, one has to consider two factors: (1) the sensitivity of the measuring circuit and (2) the fringe effect. Basically, for a fixed permittivity and diameter, the capacitance value is directly proportional to the length of electrodes, i.e. longer electrodes give larger capacitance. However, too long electrodes will reduce the axial resolution and narrow bandwidth. To detect smaller objects, shorter electrodes are preferred. On the other hand, too short electrodes can cause too small inter-electrode

capacitance, which then requires a more sensitive measuring circuit. There is a limit on how short the electrodes could be, as at a certain point the length of the electrodes could just saturate the measurement. In addition, the fringe effect is more prominent and cannot be neglected with shorter electrodes because it will affect image reconstruction. In common practice, it is recommended that the length of the electrodes is chosen greater than the sensor diameter (say twice) so that it is possible to reduce serious fringe effect (Yang, 2010; Yan *et al.,* 1999).

c. Location of electrodes

When a container, e.g. pipe, vessel or tank is non-conducting, both external and internal electrodes are permissible in ECT. In practical, it is standard to have electrodes mounted outside the pipe because it makes the sensor easier to build. An ECT sensor with only external electrodes is both non-intrusive and non-invasive, which is often required by industry. Being outside the pipe avoids the electrodes to be exposed to the harsh in-process environment. However, if the pipe wall is too thick, the capacitance of the pipe wall needs to be taken into consideration to avoid measurement error.

Electrodes can also be mounted inside the pipe or else a combination of both, external and internal. Some examples of ECT with internal electrodes are by (Liu *et al.,* 2001; Jaworski and Bolton, 2000; Ye and Yang, 2013). With internal electrodes, an ECT sensor is more sensitive because of the direct physical contact between the electrodes and the material. In addition, it removes the effect of pipe wall on capacitance measurement. Despite the advantageous, there are still many limitations with having internal electrodes, not only as a disruption to the flow but also it affects the lifespan and reliability of the ECT sensor. Internal electrodes have high risk of being damaged as they are exposed to harsh environment and becoming more fragile (Yang, 1997; Yang, 2010).

2.2.2 Sensor shape

Currently, in most laboratories and industry, their facilities, such as pipes, boilers, vessels and tanks, are circular. Accordingly, circular ECT sensors have been extensively investigated and well established. However, for some applications, e.g. the fluidised bed, different shape of ECT is required. The first feasibility study of ECT with a square sensor for circulating fluidised bed was reported by (Yang and Liu, 1999). The results

indicated that for a specific condition, the square sensor improved the sensitivity in the centre area and provided better image resolution. In (Liu *et al.*, 2001), the design of square ECT was extended with internal-external electrodes, i.e. 12 externals and 4 internals. It was found that the combination can improve the images, but the internal electrodes can cause disruption to the fluid flow.

An open end 16-electrode square sensor was developed for a feasibility study by (Ren and Yang, 2012). In their work, 8 electrodes were arrayed opposite of each other and used to image three plastic bars with an impedance analyser system and a MATLAB GUI. In recent years, there are more advanced machines with more complicated processes, structures and flows. It is foreseen that the shape of ECT sensors would be more diverse to cope up with the complexities. Some examples are the Wurster fluidised bed and the supersonic wet gas separator, which possibly requires a conical ECT sensor (Twister, 2017; Glatt, 2014)

2.2.3 Driven guard electrodes

Some researchers propose driven guard electrodes to improve the axial resolution and measurement sensitivity. The aim is to allow the use of shorter electrodes. The driven guard electrodes are mounted symmetrically at both ends of the measurement electrodes. These driven guard electrodes are excited with the same electrical potentials as the measurement electrodes. This arrangement will reduce the fringe effect because the electric field is not diverted to earth or to axial directions. Therefore, a stronger signal can be obtained. However, this is valid if only the sensor is fully filled with a single material, which is not beneficial to multiphase flow measurement. In addition, the shortcoming of using driven guard electrodes is that they interrupt with the capacitance measurement. In other words, the measured capacitance is actually between the three electrodes i.e. the measurement and the two driven guard electrodes (Yang, 2010; Process Tomography Ltd, 2001).

2.2.4 Earthed screen

There are three types of the earthed screen used in ECT sensor: (1) the outer screen, (2) two axial end screen and (3) radial screen. In general, all of them are used to protect the ECT sensor from external noise (Yang, 2010). The outer screen covers the whole external pipe circumference and is effective in shielding the sensor from the interference

and surrounding noise. In practice, it is common to use the second type not only for noise reduction but also minimising the fringe effect (Sun and Yang, 2014). The construction of the first two types of the screen is simple, but the latter is more complicated. However, if the standing capacitance between adjacent electrodes is a concern, the radial screen might need to be taken into consideration (Yang, 1997).

2.3 Measuring circuits

An ECT sensor is connected to a measuring circuit. The hardware of the measuring circuit was reviewed by (Yang, 1996) and (Yang and Peng, 2003). There are three common types of measuring circuit for ECT: (1) the charge/discharge circuit (Huang *et al.*, 1992), (2) AC-based circuit and (3) impedance analyser. The charge/discharge and AC-based circuits are for real-time imaging while the impedance analyser is for offline imaging (Li, 2008). These three circuits are the preferred options for their immunity to stray capacitance (Yang, 1996).

The charge/discharge circuit operates in the DC mode and it works in phases, by charging and discharging the measured capacitance. The operation of the circuit is controlled by a clock signal with a programmable frequency up to 2.5 MHz (Yang, 1996). Other than stray immune, this circuit has benefits of being simple and low cost. However, several disadvantages of this charge/discharge circuit are: (1) charge injection from the CMOS switches causes problem, (2) drift problem due to the DC operation and (3) loss conductance problem (Huang *et al.,* 1988; Huang *et al.*, 1989; Yang, 1996).

The AC-based circuit works with sine-wave excitation and phase-sensitive demodulation. This circuit measures impedance or with a phase-shift-demodulation, it measures capacitance or conductance. The excitation frequency is up to 1 MHz. An AC-based circuit reduces the measurement noise, has a high signal-to-noise ratio (SNR) with low drift, other than being stray-immune. However, this circuit is complicated and more expensive, especially for high-frequency operation (Yang, 1996).

The impedance analyser-based ECT system developed at the University of Manchester is shown in Figure 2.3. The system consists of: (1) an ECT sensor, (2) a multiplexer box, (3) impedance analyser and (4) a host PC. A PCI IEEE 488 board and National

Instrument (NI) PCI-6024E data acquisition board are used to control the impedance analyser HP 4192A and the multiplexer respectively (Yang, 2007).

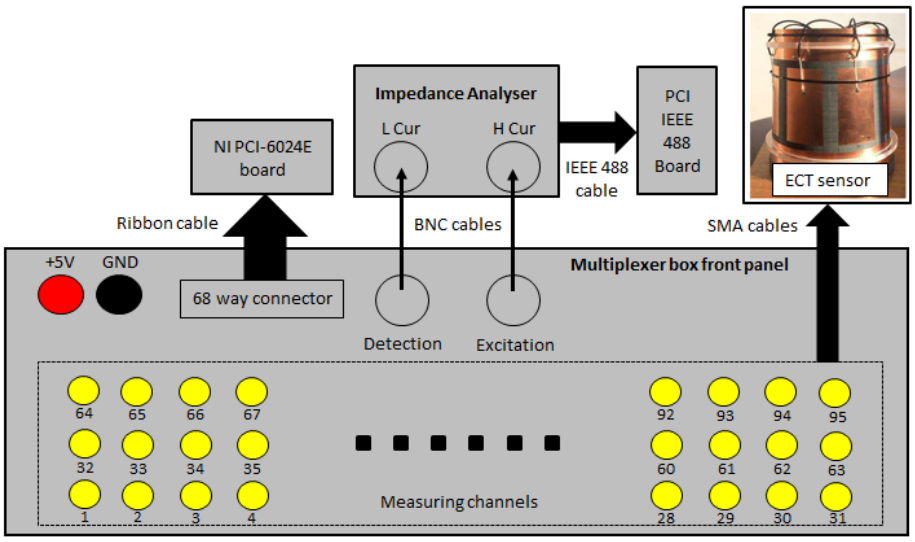

Figure 2.3: Impedance analyser system (Yang, 2007)

The impedance analyser is a fully automatic, high-performance test instrument that has been designed to measure electrical properties, i.e. the capacitance, resistance and conductance (Agilent, 2000). Because of its high accuracy, high resolution and good reliability, the impedance analyser has been used to measure electrical property measurement for some ECT applications (Chrondronasios, 2003; Hu *et al.*, 2008). A difficulty with impedance analyser is that it has a limited channel, therefore a multiplexer is required. The H Cur (high current) and L Cur (low current) of the impedance analyser are connected to the detection channel and the excitation channel of the multiplexer via a pair of BNC cables. The impedance analyser uses a sine-wave excitation voltage with programmable amplitude and frequency. The range of the frequency is from 1 kHz to 10 MHz. The multiplexer has a total of 96 programmable channels, which can be configured to three different operation modes: (1) excitation, (2) detection and (3) ground. The ECT sensor is connected to the multiplexer by SMB cables according to the number of electrodes. By alternating the status of each electrode, independent measurements can be taken for different electrode pairs. The measurements are transferred to the host PC for data analysis and image reconstruction (Yang, 2007). Despite all the advantages, the impedance analyser has limited speed, hence only offline imaging is applicable (Li, 2008).

2.4 Forward problem

The forward problem is to estimate the inter-electrode capacitance from a known permittivity distribution. There are three reasons of solving forward problem: (1) to evaluate ECT sensor design (2) to obtain sensitivity maps and (3) for iteration (Ren, 2015). There are two ways of solving the forward problem, either by direct experiment or by simulation (Yang *et al.*, 1995). Since the capacitance difference is very small, the first method requires tedious procedure and very sensitive transducers. Hence, the latter is preferable.

There are two most relevant numerical approaches of solving the forward problem for the industrial applications (1) finite-different method (FDM) (Fang, 2004) and (2) finite-element method (FEM) (Yang and Conway, 1998). Both methods are described by partial differential equations (PDEs) to obtain the potential distribution.

FDM is the oldest method based on Taylor's polynomial to approximate the partial differential equation. Basically, FDM uses a topologically square network of lines to construct a mesh. This factor is limiting the geometry design, thus the application is more suitable for rectangular shapes and simple design.

FEM is a more sophisticated and flexible method, which can find approximate solutions to the partial differential equation, PDE as well as the integral equations. In general, FEM does not rely on any specific mesh structure (Peiro and Sherwin, 2005). The integral formulation does not require the element boundary to be too sharp to assure accuracy. FEM has been developed successfully for computer simulation used in engineering application, for example in multiphase flows, heat transfer and electromagnetism. A few examples of available software packages in the market are COMSOL, ANSOFT, CAMPOM or the MATLAB-based virtual ECT. In this project, COMSOL is selected for FEM simulation because of its valuable features, such as GUI tools for creating geometry and domains, automatic mesh generation and capability of solving equations. The equation solves the unknown values using linear algebra or a nonlinear numerical scheme, such as 2^{nd} order algebra approximation. In general, the software performs in 3 steps: (1) pre-processing, which defines the modelling and factors, (2) solving a finite element model and (3) post-processing results, with data or visualisation tools. Examples of FEM mesh and potential distribution on COMSOL are

shown in Figure 2.4. The FEM-based calculation is definitely more complicated than FDM but provides good accuracy. In addition, FEM is a good option for most types of analysis in structural mechanics with high capability of handling complex geometries and boundaries.

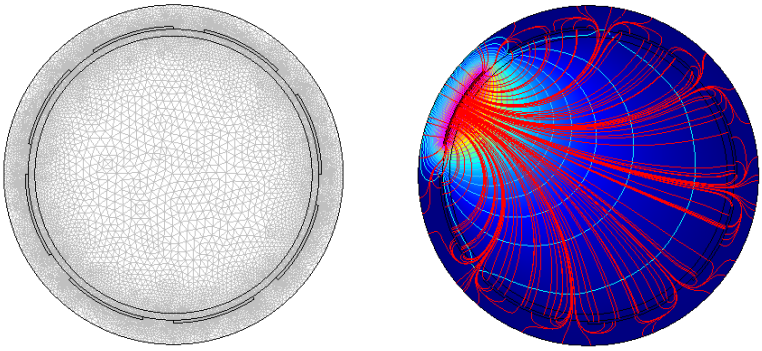

(a) FEM mesh (b) Potential distribution

Figure 2.4: Examples of FEM mesh and potential distribution on COMSOL

Once the potential distribution is solved using the solver, which in this research is using COMSOL, the electric charge Q can be calculated by means of the Gauss Law (Kim *et al.*, 2007)

$$Q = -\oint_{\Gamma} \varepsilon(x,y)\nabla\phi(x,y)d\Gamma \tag{2.2}$$

where Γ is the electrode surface, $\phi(x,y)$ is the potential distribution and $\varepsilon(x,y)$ is the permittivity distribution at coordinate x and y. Then, the inter-electrode capacitance can be calculated by (Kim *et al.*, 2007)

$$C = \frac{Q}{V} = -\frac{1}{V}\oint_{\Gamma} \varepsilon(x,y)\nabla\phi(x,y)d\Gamma \tag{2.3}$$

where V is the voltage between the excitation and detection electrode.

2.5 Sensitivity map

The sensitivity map is the sensitiveness measurement of the region in detecting the change of the permittivity of the medium that will affect the capacitance value (Isaksen and Nordtvedt, 1993). The number of sensitivity maps is determined by the number of electrodes of an ECT sensor. Generating sensitivity maps is commonly carried out by dot multiplication. A recent study shows that perturbation method by simulation can be done (Frias, 2015). Both methods use FEM software, COMSOL to obtain the electric potential and MATLAB to simulate the sensitivity maps.

The dot multiplication method uses electric fields between an excitation (*i*) and detection (*j*) electrodes to calculate a sensitivity map. In this case, one electrode is set as an excitation electrode, while the rest are grounded. When the voltage, *Vi* is applied on the excitation electrode *i*, the sensitivity between electrode pair $i-j$ is defined as (Liu, 2001)

$$S_{i,j}(x,y) = -\oint_{p(x,y)} \frac{E_i(x,y)}{V_i} \cdot \frac{E_j(x,y)}{V_j} dxdy \tag{2.4}$$

where $E_i(x,y)$ is the electric field distribution at (*x,y*) when electrode *i* is the excitation electrode at potential V_i, whilst other electrodes remain at ground, and $p_{(x,y)}$ is the area of the pixel at (*x,y*).

As an alternative, equation (2.4) can be expressed as gradient format of the electric field in Laplace equation.

$$S_{i,j}(x,y) = -\oint_{p(x,y)} \left(\frac{\partial \phi_i}{\partial x}\frac{\partial \phi_j}{\partial x} + \frac{\partial \phi_i}{\partial y}\frac{\partial \phi_j}{\partial y} \right) dxdy \tag{2.5}$$

where $\partial\phi_i/\partial x$ and $\partial\phi_i/\partial y$ are gradient of potential value with electrode *i* in *x* vector and *y* vector, respectively (Li, 2008).

Examples of common sensitivity maps with the empty background for 8-electrode ECT sensor are shown in Figure 2.5.

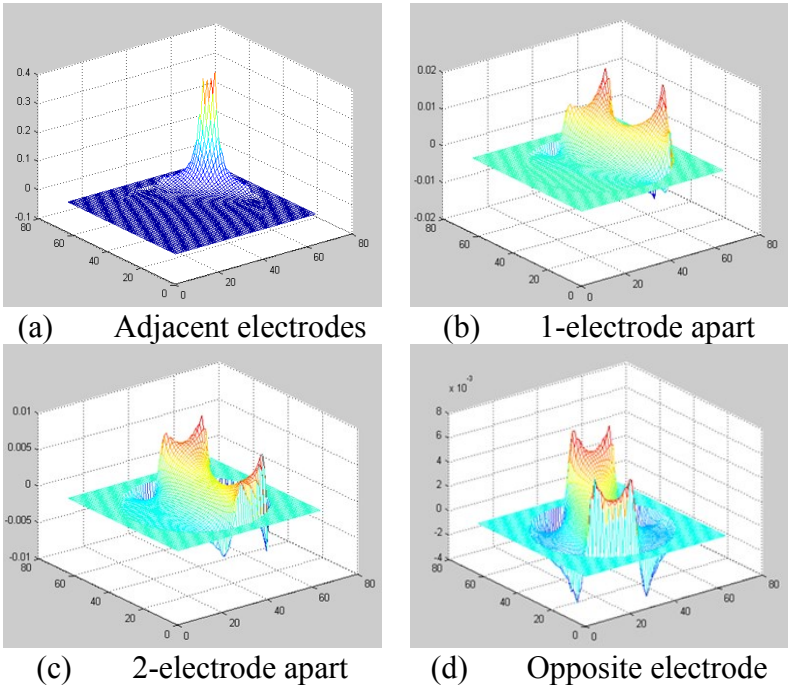

Figure 2.5: Examples of common sensitivity maps for 8-electrode ECT sensor

2.6 Inverse problem

The goal of solving the inverse problem is to visualise the component's permittivity in the sensing area from the variation of capacitance between the two electrodes. The relationship between capacitance and permittivity can be defined as (Ren, 2015)

$$C_{norm} = Sg \tag{2.6}$$

where C_{norm} is the normalised capacitance, S is the normalised sensitivity matrix and g is the normalised permittivity distribution. The C_{norm} can be calculated by using (Ren, 2015)

$$C_{norm} = \frac{C_m - C_L}{C_H - C_L} \tag{2.7}$$

where C_m is the measured capacitance when the sensor filled with test material or test flow regime, and C_H and C_L are the capacitances with the sensor filled with high and low permittivity material respectively.

There are two major difficulties related to equation (2.6): (1) the ill-posed and (2) ill-conditioned. Ill-posed is a condition of a limited number of independent measurements compared to the unknown variables such as the number of pixels, which creates various possible images or solutions. Ill-conditioned makes equation (2.6) sensitive to small perturbations of C_{norm}, causing high potential of measurement and numerical error in image reconstruction (Yang and Peng, 2003; Yang *et al.,* 1999).

For the past three decades, there is tremendous development of algorithms reported for ECT to solve inverse problem, including non-iterative such as the linear-back-projection (LBP) (Xie *et al.*, 1992), Tikhonov regularisation (Tikhonov and Arsenin, 1977) and singular value decomposition (SVD) (Peng *et al.*, 2000). The iterative algorithms are like the Landweber (Yang *et al.*, 1999; Liu *et al.*, 1999; Li and Yang, 2007; Li and Yang, 2008), Newton-Raphson method (Hansen, 1997) and total variation method (TV) (Wang *et al.*, 2007; Soleimani and Lionheart, 2005) . There are also some other iterative unconventional algorithms proposed, such as the model-based iterations (Isaksen *et al.*, 1994; Banasiak and Soleimani, 2010; Ren *et al.*, 2014). The suitability of algorithms based on many factors but the accuracy and speed are the main concerns. In practice, many researchers prefer LBP because it is simple and fast, but with Landweber a good image quality is expected.

LBP is a straightforward non-iterative algorithm, which uses linear approximation. If inverse sensitivity matrix, S^{-1} exists, then equation (2.6) can be simply rewritten as

$$g = S^{-1}C_{norm} \tag{2.8}$$

However, S^{-1} does not exist because it is a non-square matrix. Therefore, an alternative method must be used. If S is assumed as a linear mapping from the permittivity vector space to the capacitance vector space, then transpose sensitivity matrix, S^T can be considered as a related mapping from the capacitance vector space to a permittivity vector space. This assumption gives an approximated solution as follows (Yang and Peng, 2003)

$$\hat{g} = S^T C_{norm} \tag{2.9}$$

where $\hat{g}$ is the estimated permittivity distribution. Equation (2.9) can be normalised to

$$\hat{g} = \frac{S^T C_{norm}}{S^T u_{C_{norm}}} \tag{2.10}$$

where $u_{C_{norm}} = [1,1 \ldots 1]$ is an identity vector.

Landweber algorithm was first initiated to solve the ill-posed problem of Fredholm integral equation of the first kind (Landweber, 1951; Li and Yang, 2008). The iteration is based on the steepest gradient method, which is extensively used in optimisation process (Yang *et al.,* 1999; Liu *et al.,* 1999; Polydorides, 2002; Jang *et al.,* 2006). Basically, Landweber iteration still uses the LBP algorithm, but with the enhancement of being iterative and has a close-loop feedback. Landweber algorithm employs an iteration number, k and a relaxation factor, α that help with the efficiency of convergence.

With a fix α, Landweber algorithm can be represented by (Yang *et al.*, 1999)

$$\begin{cases} \hat{g}_0 = S^T C_{norm} \\ \hat{g}_{k+1} = \hat{g}_k + \alpha S^T (C_{norm} - S\hat{g}_k) \end{cases} \tag{2.11}$$

where the initial value of $\hat{g}_0$ is normally calculated using LBP.

With the Landweber, the image error decreases quickly during the earlier iterations, but it would increase after the minimal point. Despite of this flaw, Landweber algorithm is still widely used and in most cases, it can provide good quality images (Yang and Peng, 2003).

Examples of reconstructed images with LBP and Landweber algorithms are shown in Figure 2.6 using a low permittivity material, ε = 1 (blue) and high permittivity material, ε= 2.1 (red). It shows that visually, Landweber managed to image the permittivity distribution more accurate to the real phantom in comparison with the LBP.

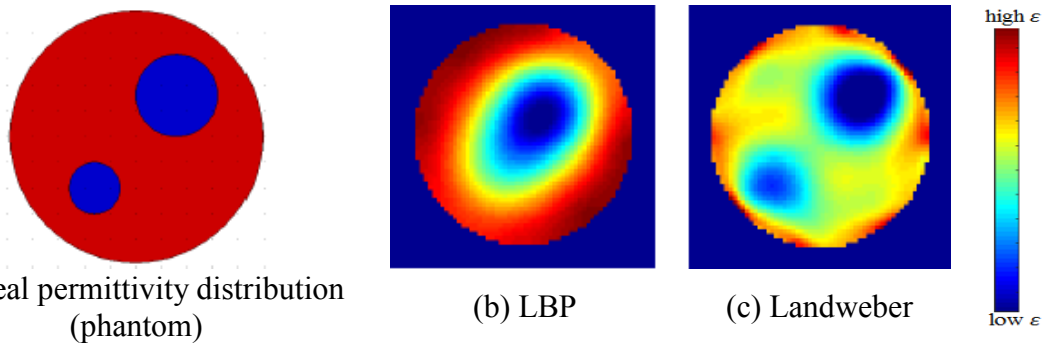

(a) Real permittivity distribution (phantom)

(b) LBP

(c) Landweber

Figure 2.6: Example of reconstructed images with LBP and Landweber algorithms

2.7 Summary

This Chapter presents fundamental knowledge of ECT, including the past and current research. The three main elements of the overall ECT system, which consists of an ECT sensor, the measuring circuit and image reconstruction algorithms, have been discussed in detail. Solutions to challenges in measurement and image reconstruction are presented.

According to the reviews, most suitable ECT sensors for this work are with 8 or 12 electrodes. An impedance analyser is chosen as the measuring circuit due to its high accuracy and high resolution. Because a circular ECT sensor is used in this research, an FEM solver with triangle element is employed to improve measurement accuracy at the boundary area. Image reconstruction will be carried out with LBP and Landweber algorithm.

Despite of all benefits that have been mentioned, there are still drawbacks in ECT. ECT is reliable and stable for an oil-continuous flow, non-conductive, low permittivity contrast materials. Research has been carried out to extend ECT functions to measure high contrast permittivity, higher conductivity material towards a water-continuous flow. However, this is still a challenge e.g. on a mixture of gas/oil/water with higher WLR, or on granules with higher moisture. To enhance the range of measurement for multiphase flows, ECT needs a complementary function. An option is to develop a dual-modality sensor. This research proposes and explores the potential of microwave sensors operated at a higher frequency to fill in the gap. Details will be discussed in the next chapters.

Chapter 3: Microwave sensors

Microwave sensors have been developed in industries since the 1950s for the measurement of the permittivity of a single material or mixture. During the 1970s and 1980s when the solid-state components and microprocessor technology were growing, microwave sensors were highly demanded. Since then, the microwave sensor technology has been advanced and been implemented for a wide range of applications, such as for measurement of distance, movement and shape, and particle size, but mostly for measurement of material properties (Nyfors, 2000).

The principle of microwave measurement is significantly different from the impedance measurement is that they operate at a higher frequency range; with a corresponding electrical wavelength between 1 mm to 1 m. Microwave sensors function based on the interaction between the waves and the object under test. The measurement is determined by the complex permittivity of the medium. As different material has different permittivity, for a mixture, the permittivity depends on the components, composition and structure of the substance. By measuring the permittivity, information about the composition can be retrieved. To measure a single or the most two phase flow, it is possible to use a single modality of sensors. However, in a case of more than two components, such as a gas/oil/water flow, dual-modality sensing is needed (Nyfors, 2000).

There are five major categories of microwave sensors: (1) transmission sensors, (2) reflection and radar sensors, (3) resonant sensors, (4) tomographic sensors and (5) radiometer sensors. Different devices can measure different properties and common parameters are for examples, the frequency of transmitted electromagnetic, the wavelength and complex permittivity. The principle for the microwave sensors and their suitability for applications have been thoroughly explained by (Nyfors and Vainikainen, 1989; Nyfors, 2000; Falcone *et al.*, 2010).

3.1 Microwave cavity resonant sensor (MRS)

The resonant cavity technique has been used for determining the dielectric properties in various applications. In 1979, at the University of Delaware, (Lakshiminarayana *et al*.,1979) designed a rectangular and cylindrical resonant sensor that operates at different frequencies, to measure the permittivity and diameter of a dielectric rod inserted through the cavity. A single Gunn oscillator system was used for coupling microwave energy into and out the cavities. They analysed the frequency shift at different modes. The result was promising with error rate 5% or lower. Research using a cylindrical cavity, but with double cut-off Gunn oscillator, to measure moisture in fibrous materials was carried out by (Hoppe *et al.*, 1980) in the Philip Research Laboratories in Hamburg. They conducted an experiment on cotton fibres and the results showed that a density-independent moisture measurement could be achieved based on two parameter microwave at fixed frequency.

There are several reports on application related to microwave treatment and measurements, i.e. heating or curing and measure with microwave, for example from (Araneta *et al.*, 1984) and (Akyel *et al.*, 1985), who used rectangular cavity for their research. The work by (Araneta *et al.*, 1984) described a technique that used cavity with single source excited by iris to simultaneously heating and characterising a dielectric rod, whilst (Akyel *et al.*, 1985) presented a computer-aided permittivity measurement (CAPM) used together with a rectangular cavity to heat and dry paper samples and concurrently measure the complex permittivity and weight of the sample. Chemical reacting materials, i.e. epoxy/amine in a single-mode cylindrical shaped cavity were diagnosed by (Jow *et al.*, 1987). They performed measurement comparison between fixed and swept frequency. It was concluded that the use of single-mode microwave resonant cavity at a single frequency in conjunction with fluoroptic temperature measurement was successful, showing a consistent result with previous work. (Kanopka and Majewski, 1980) from the Institute of Physics in Warsaw developed a method that exposed the experiment sample to strong electromagnetic fields and then measured small change in electric or magnetic change in material. Their system comprises of two microwave signal sources, a cylindrical cavity and super-heterodyne receiver. They claimed that the method was very sensitive for detecting changes in conductivity at the smallest of 10^{-10} order.

The cylindrical cavity resonator has also been used as a humidity sensor by (Toropainen *et al.*, 1987). The construction of the cavity was fully made of metal and has a partition that splits a portion of the waveguide into coaxial and smaller waveguide. At 9.5 GHz, the system measures the humidity of air from the real permittivity and temperature of the air flow. They claimed that the sensor is dirt-insensitive and can work in a wide range of temperature.

It was reported to determine water in oil emulsions with cavity resonator, e.g. by (Doughty, 1977) of Bartlesville Energy Research Centre, Oklahoma. Doughty used a rectangular cavity with a thin pipe to measure a small sample of liquid ($0.2cm^3$). The apparatus operates at 9.51 GHz and measures water content from 0% to 100%. It was concluded that the results from the experiments were confined and applicable, but the precision decreased with higher WLR (above 40%). However, it was also suggested that a larger sample can be used to overcome the problem.

Previous research also includes microwave cavity resonator to be used in automotive as a device to monitor combustion cycle (Merlo, 1970) and as a miniature temperature transponder (Baumann *et al.*, 1987).

More recent research includes the usage of the cylindrical cavity for multiphase flow measurement, specifically through pipelines in the oil and gas industry. In 2006, (Wylie *et al.*, 2006) from Liverpool John Moores University in conjunction with Solartron ISA developed a cylindrical cavity resonator with antennas to excite the resonant modes. The system works in a range of 100-350 MHz and measured resonant peaks instantaneously for detection of phase fractions. They carried out experiments with dynamic dispersed and annular flow at National Engineering Lab (NEL), East Kilburn, Scotland. The tests were done on two-phase (oil/water) and three-phase (gas/oil/water) flows with water fraction of maximum 52%. Research on determining water fraction was also carried out by (Avila *et al.*, 2013). They used a cylindrical resonant cavity sensor with a portable scalar network analyser system (SNA) to detect water fraction in a stratified two-phase flow of water/gas and water/oil. The WLR ranges from 0% to 100%, with fresh and sea water. They concluded that at their defined flow conditions, the fundamental resonance was sufficient to measure the fluid features, including the percentage of water. More examples of reported work employing cavity resonant sensor

were carried out by (Al-Hajeri *et al.*, 2007, (Gennarelli *et al.*, 2013) and (Nohlert *et al.*, 2015).

3.1.1 MRS system

Figure 3.1 shows the overall MRS system that was developed at the University of Manchester for this research. It consists of: (1) a cavity resonator, (2) a scalar network analyser (SNA) system and (3) a control PC. The electromagnetic signal is injected to and received from the sensor through 50ohm coaxial cables. The SNA system is powered and controlled using USB cables, with the graphical user interface (GUI) software (SPIKE) for display. The transmitter and receiver are connected using a BNC cable. More details of the main components will be described in the following sections.

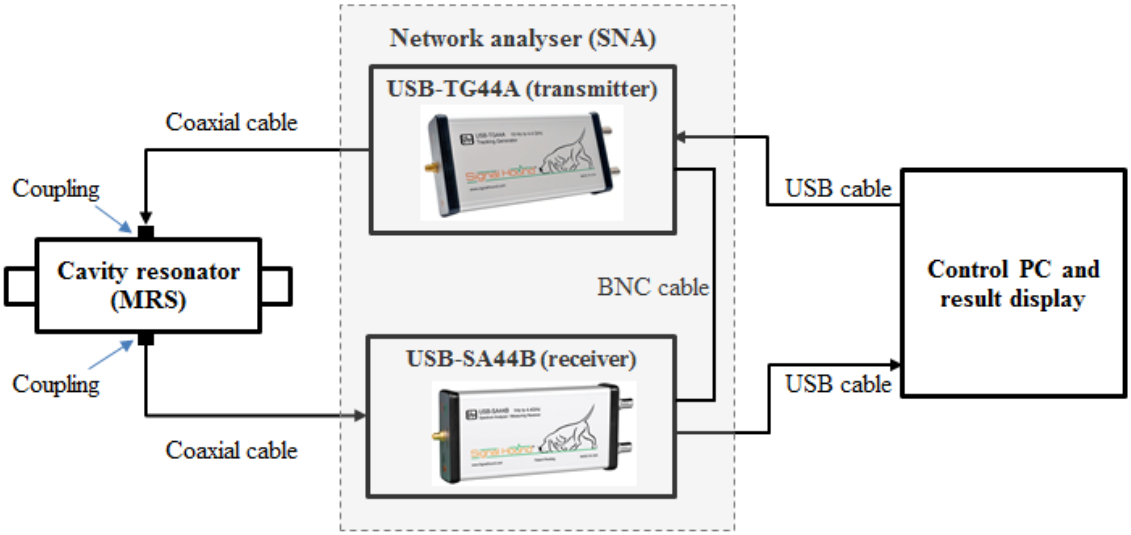

Figure 3.1: Microwave cavity resonant sensor (MRS) system.

3.1.2 Cavity resonator

Cavity resonators are closed metallic devices in which the energy is stored in the electromagnetic fields at high frequency (Avila, 2013). The most common structure of a cavity resonators is with the rectangular and cylindrical shapes, as shown in Figure 3.2 (Ishii, 1989).

In the cavity, resonance occurs when the propagation wave and reflected wave are in phase, where the interference could produce a constructive or destructive wave pattern called a standing wave pattern. This phenomenon happens at distinct frequencies called resonant frequencies, that correspond to a different propagation modes denoted as

transverse electric, TE_{mnl} and transverse magnetic, TM_{mnl}, where *m, n* and *l* are the number of variations in the standing wave pattern in *x*, *y* and *z* directions (Nyfor and Vainikainen, 1989; Pozar, 2008).

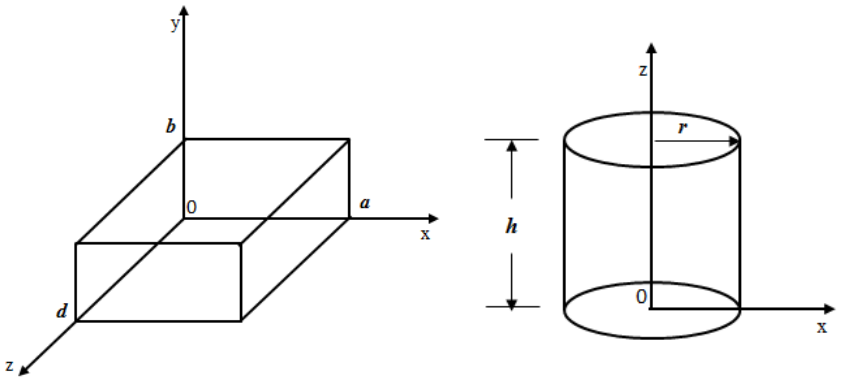

(a) Rectangular (b) Circular

Figure 3.2: Structure of cavities

The resonant frequencies of rectangular and cylindrical resonators as above structures can be expressed as equation (3.1) and (3.2), respectively (Pozar, 1998).

$$f_{r(mnl)} = \frac{c}{2\pi\sqrt{\mu\varepsilon}}\sqrt{\left(\frac{m\pi}{a}\right)^2 + \left(\frac{n\pi}{b}\right)^2 + \left(\frac{l\pi}{d}\right)^2} \tag{3.1}$$

$$f_{r(nml)} = \frac{c}{2\pi\sqrt{\mu\varepsilon}}\sqrt{\left(\frac{p'_{nm}}{r}\right)^2 + \left(\frac{l\pi}{h}\right)^2} \tag{3.2}$$

where *c* is the speed of light (3 x 10^8 m/s), μ and ε are the permeability and permittivity of the material filling the cavity, respectively. p'_{nm} is the cut-off wavenumber of TE_{nml} wave mode in cylindrical cavity. For TM_{nml} mode, p'_{nm} should be replaced by p_{nm} as derived by (Nyfors, 2000) and (Pozar, 1998). *a*, *b*, *d*, *r* and *h* are the cavity's geometrical parameters as shown in Figure 3.2.

3.1.3 Coupling devices

A resonant sensor needs to be coupled with an external electronic circuit to perform the measurement. To obtain the maximum transmission power, the resonator must be critically coupled to the feed. There are many kinds of coupling devices to be used, but

in common they can be classified as: (1) probe, (2) loop and (3) aperture. The structure and principle of each coupling devices have been described by (Nyfors, 2000; Nyfors and Vainikainen, 1989).

A probe is a coaxial cable that is extended to become a coupling probe. The current flow is small but the voltage is enough to create an electric field. The energy propagates like a small monopole antenna, between the probes and the wall of the resonant sensor. This coupling probe is easy to tune and suitable for very-high-frequency (VHF) and ultra-high-frequency (UHF) band microwave.

A loop is basically an extended probe coupling, with bent centre conductor grounded to the wall of the resonant sensor. The grounding creates a short circuit to the feeding line. The voltage becomes negligible but the current creates a strong magnetic field. The magnetic field radiates along the loop tangential to the resonator wall. A loop coupling is more rugged than the probe coupling but more difficult in tuning.

Aperture coupling is normally a small round hole in the waveguide or at the shorted end. It can be magnetic or electric coupling aperture, depending on the resonance mode. The electric field or magnetic field can penetrate through the aperture and coupled with the resonance mode. The location of the aperture influences the coupling with reference to the resonance mode and field lines (Nyfors and Vainikainen, 1989).

3.1.4 Network analyser

A network analyser measures scattering parameters of linear microwave element as a function of frequency. There are two types of network analyser in common: (1) scalar network analyser (SNA) and (2) vector network analyser (VNA). The major difference between a VNA and SNA is that the VNA measures both amplitude and phase whilst the SNA only measures the amplitude.

In this research, a Signal Hound tracking generator (USB-TG44A) and a spectrum analyser (USB-SA44B) from Test Equipment Plus is programmed as an SNA to measure scattering parameter, S_{21} as a function of frequency. The principle of scattering parameters can be referred to (Kurokawa, 1965; Eisenstadt and Eo, 1992; Pozar, 1998). With this system, the detection bandwidth is narrow, usually providing a large dynamic

range, and hence spurious harmonic signal can be avoided. The operating frequency and temperature can be up to 4.4 GHz and 70^{o}C respectively (Test Equipment Plus, 2010). This system is chosen over a VNA because it is portable, compact and simple to use for a general lab experiment.

3.2 Microwave tomography (MWT)

In the early 1980s, the development of microwave imaging technique becomes significantly notable. It was recognised as a new area of investigation and Microwave Prize was awarded at the European Microwave Conference in Nurnberg, 1983 (Bolomey, 1989). The technology was first found medical applications, with great influence from the research of (Larsen and Jacobi, 1979). Their research was using microwave frequency at range 3.9 GHz for image projection of canine kidney. Some early extensive feasibility studies of microwave tomography in biomedical application were carried out by (Bolomey *et al.*, 1982) in collaboration with Laboratoire de Thermologie Biomedicale (Strasburg) and Societe d'Etude du Radant (Orsay), and (Pichot *et al.*, 1985; Peronnet *et al.*, 1983) from the Laboratoire des Signaux et Systemes, France, in detecting isolated organs. Microwave tomography was also proposed to be used for tissue assessment (Meaney *et al.*, 1996), detection of breast cancer (Irishina *et al.*, 2008; Xu *et al.*, 2012) and detection of thermal gradient in the brain to control hyperthermia (Broquetas *et al.*, 1987; Rius *et al.*, 1992). Some other non-medical applications of microwave tomography are research by (Olver and Cuthbert, 1988), (Chommeloux *et al.*, 1986), (Aitmehdi *et al.*, 1988) and (Dourthe *et al.*, 2000).

The investigation of microwave tomography for multiphase flow imaging started in the 1990s at UMIST (currently known as University of Manchester). Since then, there are many related research activities on microwave tomography, especially for oil and gas application. In 2009, (Wu *et al.*, 2009) developed a microwave tomography system to image static-dielectric distribution at two different frequencies i.e. 2.5 GHz and 4 GHz. The result obtained from this research was promising with images at 4 GHz giving good quality and high resolution.

3.2.1 MWT system

The objective of the MWT is to determine the complex permittivity distribution from the scattered electromagnetic field around the periphery of the substance at different angles to create multiple views, with normally uniform permittivity background (Wu *et al.*, 2009).

The MWT system used in this research was designed at the University of Manchester. The software was developed by the Sensona Ltd, UK and the whole system has been tested for the first time in the Institute of Engineering Thermophysics (IET), Chinese Academy of Sciences, Beijing. The microwave tomography system is shown in Figure 3.3. The sensor has 16 symmetrically arranged mono-pole copper antennas connected to 16 measurement channels. The antennas are 15 mm in length and are used as 8 transmitting antennas and 8 receiving antennas. Adjacent antennas are separated by 22.5^{o} and are numbered in clockwise. All the antennas are connected to the ports according to the connection arrangement e.g. antenna 1 to port 1, and antenna 2 to port 2. The Sensosoft software, which is the integral part of the system, is installed on a control laptop that is connected to the MTS-LU-16-1000 hardware via a USB hub and USB cable. The system is powered up by 24 V supply and operates at a frequency range of 1-2.5 GHz (Sensona Ltd. UK, 2013).

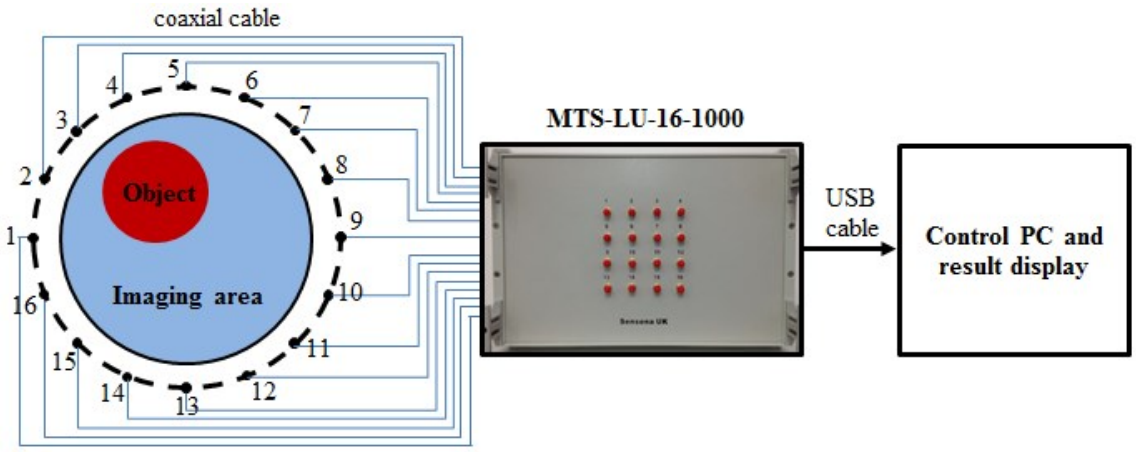

Figure 3.3: Microwave tomography (MWT) system

A comprehensive comparison between the ECT and MWT systems used in the IET for the experiments in Chapter 6 is shown as in Table 3.1 (Wang *et al.*, 2016).

Table 3.1: Comparison between ECT and MWT system at the IET for experiments in Chapter 6 (Wang *et al.*, 2016)

Features	ECT	MWT
• Operating frequency	10 kHz ~ 500 kHz	1 GHz ~ 2.5GHz
• Sampling frequency	120 f/s (12 electrodes)	20 f/s
• Measure change of permittivity	Yes	Yes
• Measure conductivity	No	Yes
• Ability to measure in low moisture	Yes	Yes
• Ability to measure in high moisture	No	Yes
• Stability	Yes	No
• Signal-to-noise ratio (SNR)	Low	High
• Cost	Low	High

3.2.2 Image reconstruction

Similar to the ECT system, to obtain images, the microwave tomography system has two main problems to solve (1) forward problem and (2) inverse problem. The objective of solving the forward problem is to determine the scattered electric field of the permittivity distribution. On the other hand, the goal of the inverse problem is to find the dielectric contrast using the measured scattered electric field data (Nugroho and Wu, 2015; Wu *et al.*, 2009). The relationship between the dielectric contrast, χ and the scattered electric field E^S can be expressed as (Franchois and Pichot, 1997)

$$F(\chi) = E^S \tag{3.3}$$

where F is a complex nonlinear vector function of χ. Due to strong nonlinear problem, a Newton iterative based on Levenberg-Marquardt method is adopted to solve equation 3.3. The derivation is described in (Nugroho and Wu, 2015; Wu *et al*., 2009; Wang *et al*., 2016). The change of scattered electric field with respect to the increment of dielectric contrast χ at k-th iteration can be written as (Wang *et al*., 2016)

$$F'(\chi_k)\delta\chi_k = \delta E_k^S = E_{meas}^S - F(\chi_k) \tag{3.4}$$

where E_{meas}^S is the measured data and $\delta\chi_k$ is the incremental of χ at k-th iteration. With the solved value of χ_k , the new solution of χ at (k+1) is given by

$$\chi_{k+1} = \chi_k + \delta\chi_k \tag{3.5}$$

The convergence of the above iteration is evaluated by equation (3.6). The iterative process stops when it meets the pre-set convergence criteria or when the number of iteration is reached.

$$error = \left\|\delta E_k^S\right\|^2 / \|E_{meas}^S\|^2 \tag{3.6}$$

3.3 Summary

In the beginning of this research, it was foreseen that using a microwave sensor can expand the working range of multiphase flow measurement because it can measure complex permittivity. The previous and current work proved some promising results in various applications. In this research, a microwave cavity resonant sensor (MRS) and microwave tomography (MWT) have been investigated as complementary functions to ECT. The major advantage of microwave sensors is that they can provide good contrast between high and low permittivity materials, i.e. between water and other dielectric materials, such as oil or powder. This feature makes them suitable for measurement of WLR or moisture in a mixture.

This Chapter has also discussed the fundamental, methodology and specification of both selected systems, MRS and MWT. The overall setup and its components for experiment have also been elaborated. MRS will be used as a water-cut meter, together with ECT for flow regime detection. On the other hand, MWT is used as another complement function of the imaging system at high moisture content, and images with a good spatial resolution are expected.

Chapter 4: Flow regime identification and WLR estimation

4.1 Introduction

The work described in this Chapter was a collaboration between the University of Manchester and the Federal University of Santa Catarina, Brazil. The aim was to develop a dual-modality of ECT and MRS system that functions in both oil-continuous and water-continuous flow. The main purposes were to (1) identify the flow pattern and (2) estimate the WLR from 10% to 90% in volume (ml). An 8-electrode ECT sensor and a cavity resonant sensor (MRS) were used to measure stratified and annular flows with oil-water emulsion as the test object. In the beginning, both ECT and MRS were individually evaluated.

4.2 Experiment setup

Figure 4.1 shows the dual-modality system of the ECT and MRS developed in the lab at the University of Manchester, UK.

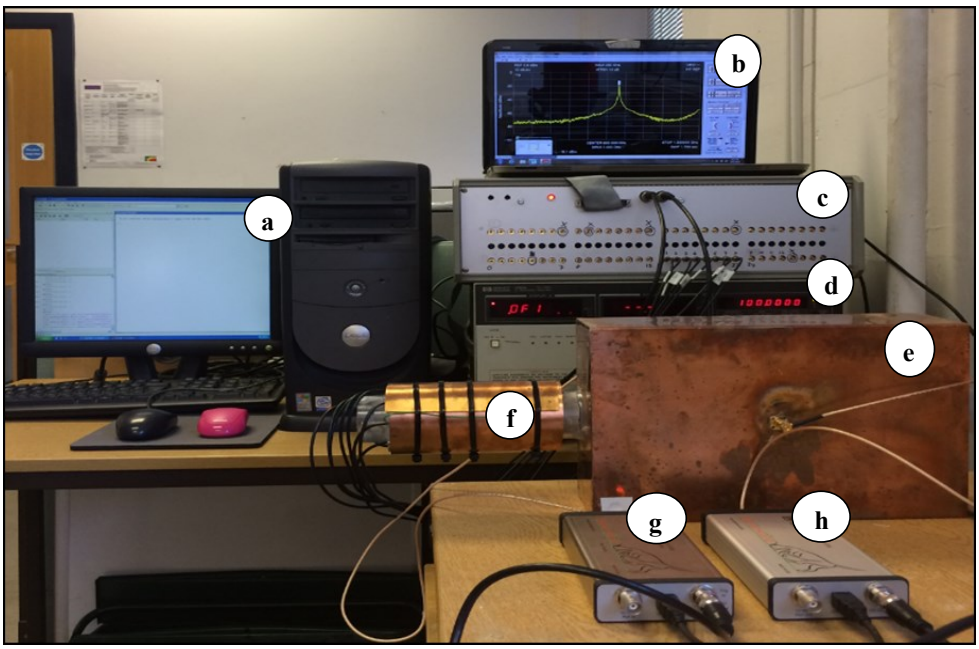

(a) PC for ECT
(b) Laptop for MRS
(c) Multiplexer
(d) HP 4192A impedance analyser
(e) Cavity resonant sensor
(f) ECT sensor
(g) USB-TG44A (Tx)
(h) USB-SA44B (Rx)

Figure 4.1: ECT-MRS overall system

Both ECT and MRS were mounted on an open end acrylic pipe. The pipe was 650 mm in length and 40 mm in inner diameter. MRS was placed at the centre of the pipe while ECT was placed at one end of the pipe. Since the acrylic pipe was almost transparent, the flow pattern could be visually observed at the other end. Both ends of the pipe can be closed with enclosures as shown in Figure 4.2 (b). To form an annular flow, the enclosures were made hollow. A thin plastic sheet and insulation tape were used to make an inner pipe, fixed to one enclosure. Once the inner pipe was inserted into the acrylic pipe, the other end was closed with a loose enclosure. A hole of 15 mm in diameter was made to serve as the liquid inlet on the acrylic pipe. Nylon tape was used to avoid leakage at both ends.

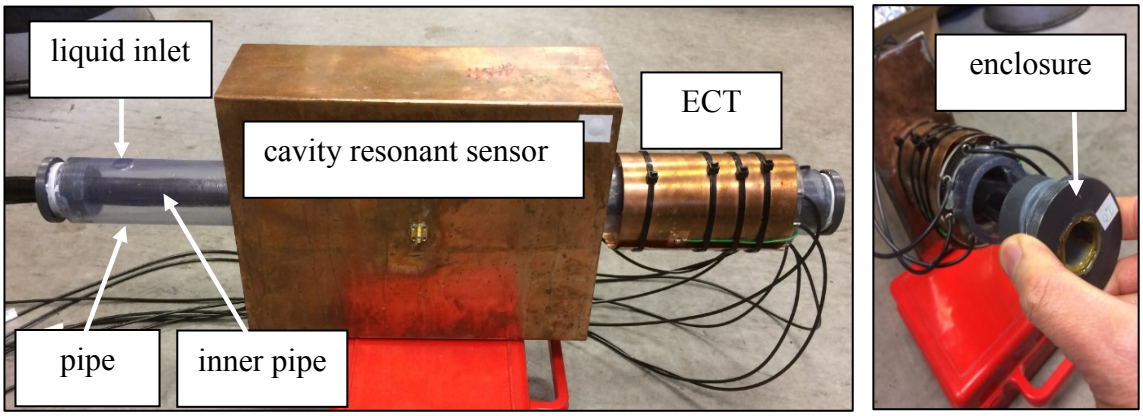

(a) Dual-modality ECT and MRS (b) Enclosure

Figure 4.2: ECT-MRS sensor

4.2.1 ECT

An ECT sensor model used for capacitance measurement is shown in Figure 4.3. It has 8 symmetrical measurement electrodes. Each of the electrodes is of 100 mm in length. A copper screen was used to prevent surrounding noise, and the gap between the screen and an electrode was 10 mm. The electrode-to-gap ratio for this ECT is 9:1, as (Tian *et al.,* 2016) suggested that a minimum ratio of 6:1 is acceptable in most cases. The sensor model was first simulated with COMSOL and MATLAB to evaluate the sensor design. The normal distribution of electric field and sensitivity within the test area, as shown in Figure 4.4, indicate that the ECT is applicable for experiments. The operation frequency for the ECT system was set at 1MHz.

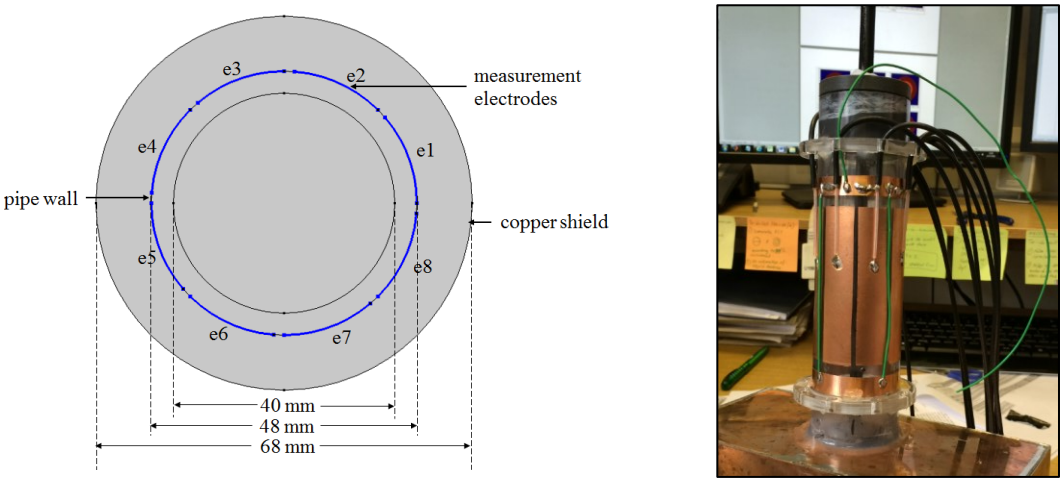

(a) 2D-cross section (b) ECT

Figure 4.3: 8-electrode ECT sensor

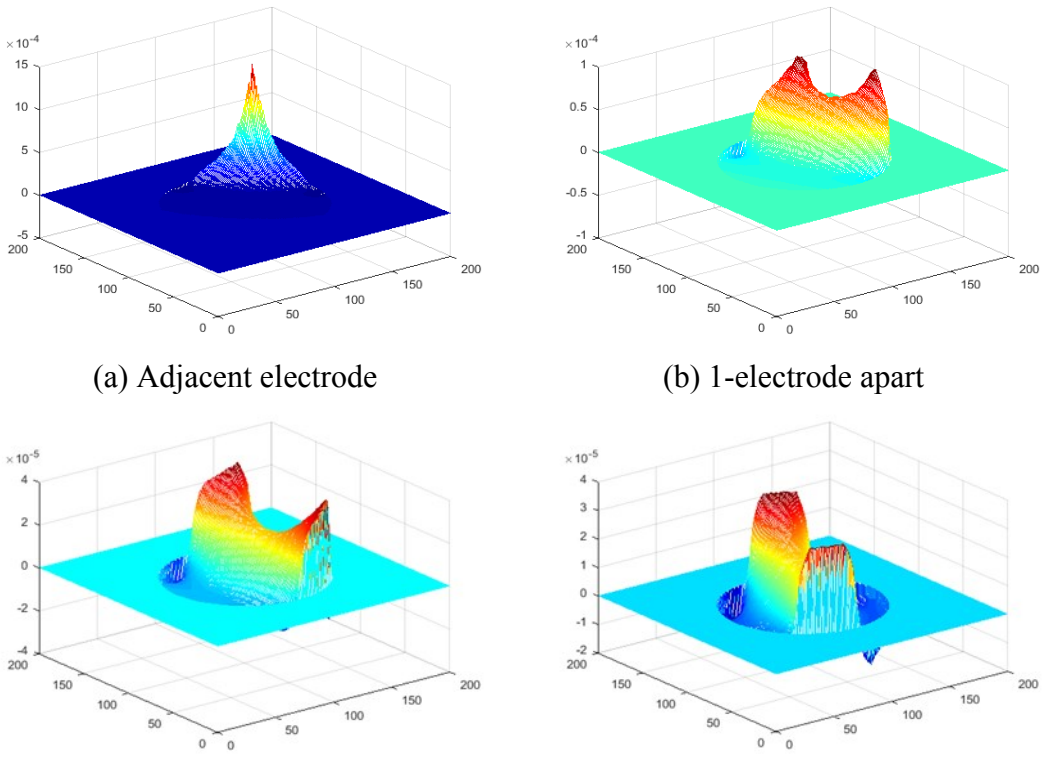

(a) Adjacent electrode (b) 1-electrode apart

(c) 2-electrode apart (d) Opposite electrode

Figure 4.4: Sensitivity maps for 8-electrode ECT sensor.

4.2.2 MRS

The geometry and connection of the MRS are shown in Figure 4.5. The rectangular resonator was made of a copper plate with two holes so that the pipe could be inserted into the cavity. The electromagnetic signal was injected to and received from the sensor through 50-ohm coaxial cables. The Signal Hound tracking generator (USB-TG44A) and spectrum analyser (USB-SA44B) were programmed as an SNA to measure the amplitude (dBm) and the resonant frequency (GHz) of the scattering parameter, S_{21}. While the ECT was measuring at a certain frequency (1 MHz), the MRS was configured to perform a frequency sweep from 0.1 GHz to 1.5 GHz.

The principle behind the design was explained in Chapter 3.1. The sensor was first tested with the vector network analyser (VNA) and then with the SNA. Figure 4.6 shows similar result of resonant peak at resonant frequency 0.9 GHz for both systems; therefore, it was concluded that the portable SNA was accurate enough to perform the measurement.

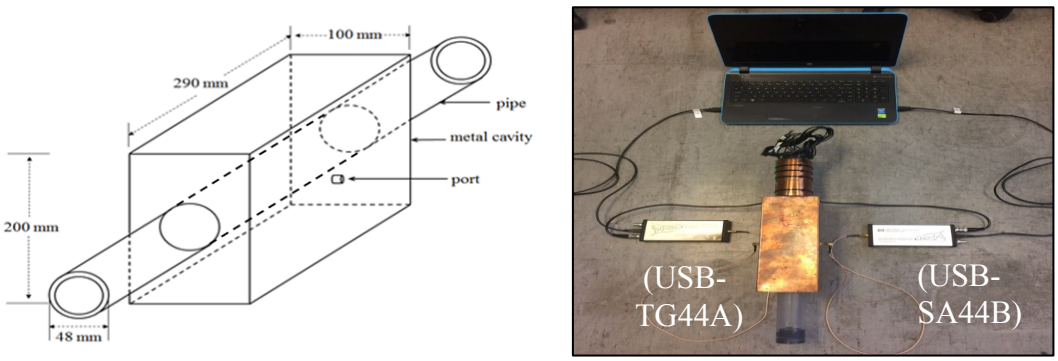

(a) Cavity (b) System connection

Figure 4.5: Individual MRS system

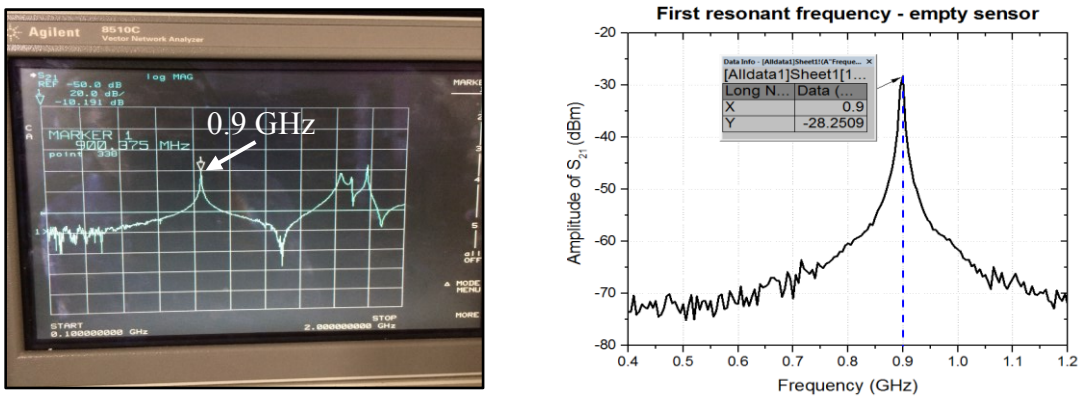

(a) From VNA (b) From SNA

Figure 4.6: MRS validation result

4.2.3 Flow regimes and test materials

For this work, the oil-water emulsion with different range of WLR was used as the test object. Stratified and annular flows were selected for the flow regime identification study, as shown in Figure 4.7. The range of the WLR for this experiment was from 10% to 90% with 10% step size.

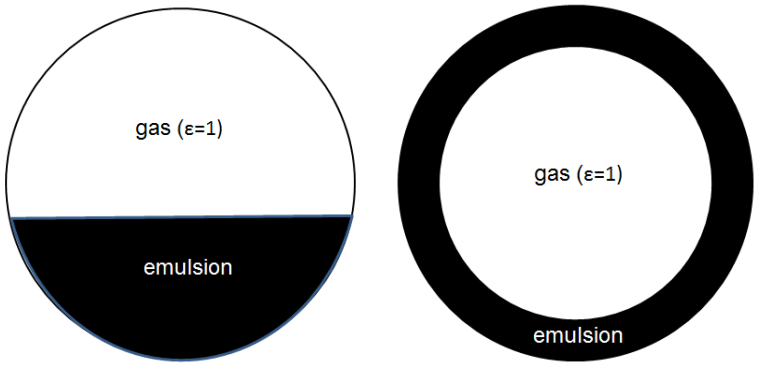

Figure 4.7: Flow regimes for identification

Tap water (ε=80) and commercial vegetable oil (ε=2.6) were used as the base liquid. For the experiments, these two types of liquid were mixed and blended with a kitchen blender to form the emulsion. Beaker scales were used to measure the amount of oil and water. Basically, an emulsion is dispersion (droplets) of one liquid in another immiscible liquid. The phase in which the droplets form is known as the dispersed phase while the phase in which the droplets are suspended in, is known as the continuous phase i.e. water-in-oil emulsions that consist of water droplets is an oil-continuous phase, and oil-in-water emulsions that consist of oil droplets is a water-continuous phase. In an oilfield industry, the amount of water that emulsifies with crude oil can vary from less than 1% to sometimes greater than 80%. Figure 4.8 shows the main classifications of the emulsions: (1) water-in-oil, (2) oil-in-water and (3) multiple or complex emulsions. Multiple emulsions are more complicated and consist of tiny droplets suspended in bigger droplets that are suspended in a continuous phase (SPE, 2016). For this research, only oil-continuous and water-continuous were considered.

The inversion point of light oil–water mixture usually occurs at 40–60% WLR. However, the point varies depending on oil viscosity. In general, the inversion process for oil-water flow can be described as in Figure 4.9 (Falcone *et al*., 2010).

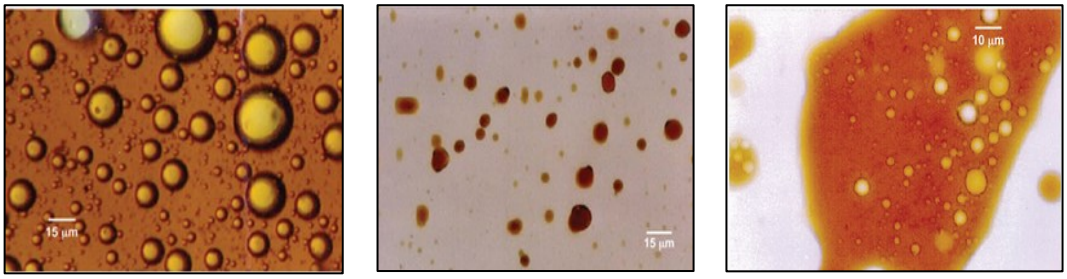

(a) Oil-continuous (b) Water-continuous (c) Complex emulsion

Figure 4.8: Emulsions (SPE, 2016)

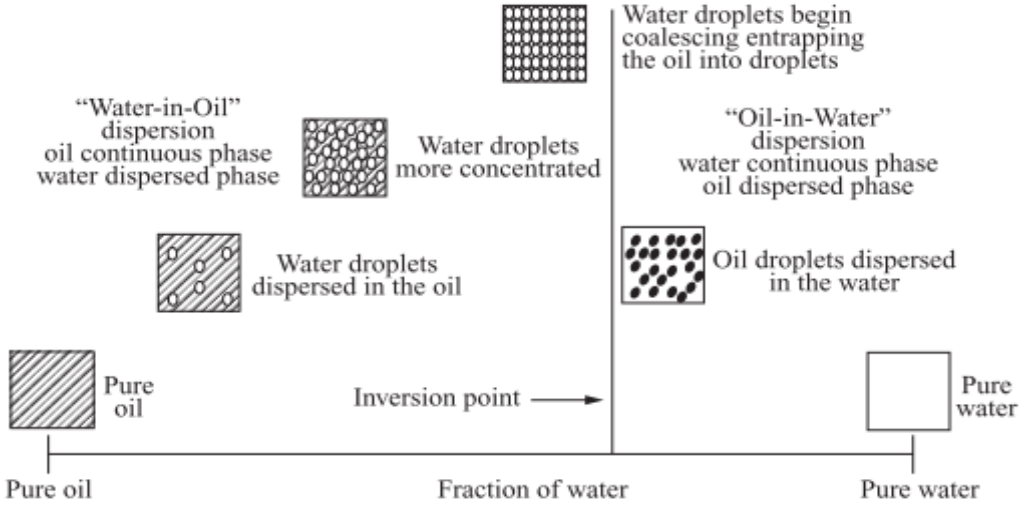

Figure 4.9: Inversion process for oil-water flow (Falcone *et al.*, 2010)

4.3 Results from ECT

In this Section, the capacitance measurement obtained by the 8-electrode ECT was analysed and processed to identify the flow regime in full phase and estimate WLR in the oil-continuous flow. All the measurements were repeated for 5 times and plotted data are based on average values.

4.3.1 Flow regime identification

An 8-electrode ECT has a total number of 28 independent measurements as expressed by equation (2.1). The typical capacitance data at the same and specific concentration with the stratified and annular flow are shown in Figure 4.10. The x-axis and y-axis represent the capacitance (pF) and the 28 independent measurements, respectively. By looking only at these two graphs, it is difficult to identify the flow regime as the trend of the graphs (oscillation of the signals) look almost identical.

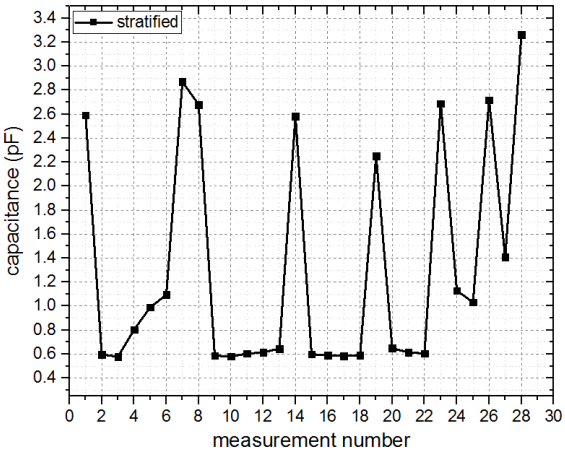

(a) Stratified

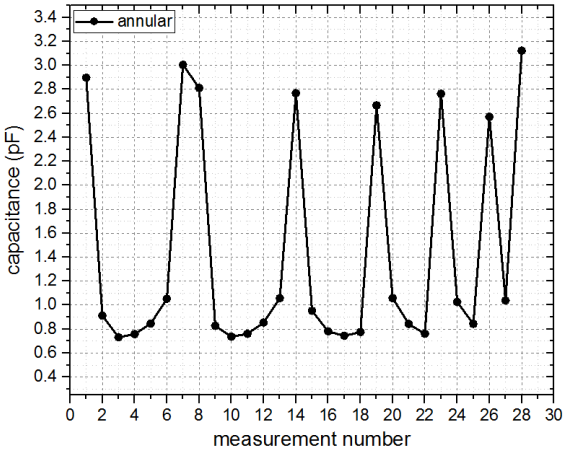

(b) Annular

Figure 4.10: Typical capacitance measurement

The data in Figure 4.10 were then analysed individually according to the electrode pairs. Figure 4.11 (a to d) shows the capacitance for adjacent electrodes, 1-electrode apart, 2-electrodes apart and opposite electrodes, respectively. From all the plots, it is observed that 1-electrode apart and 2-electrodes apart data demonstrate an obvious difference between the stratified and annular flows. Therefore, these unique individual data patterns can be used as a method to identify the flow regime from the capacitance measurement.

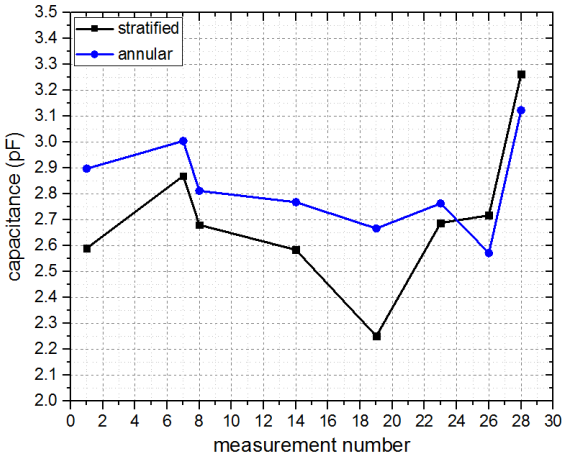

(a) Adjacent electrodes

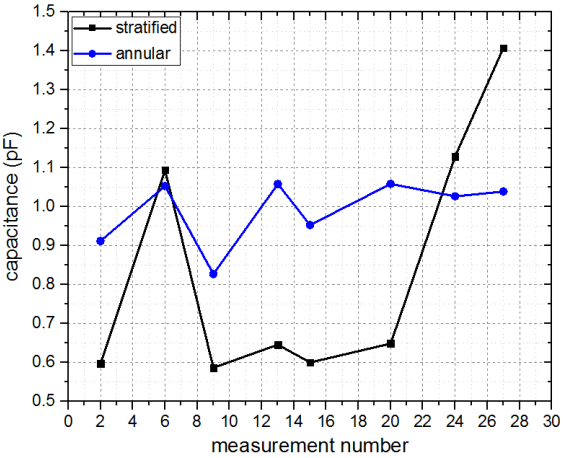

(b) 1-electrode apart

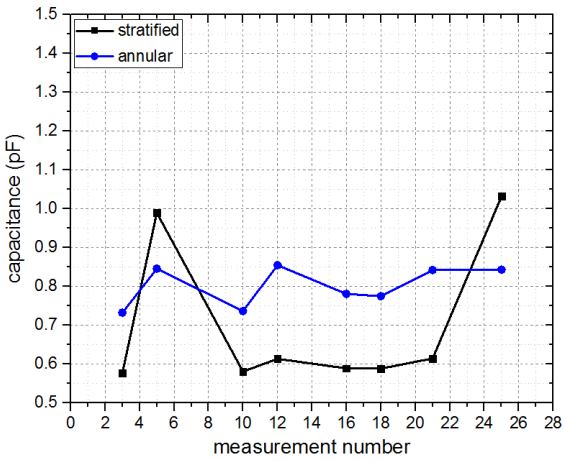

(c) 2-electrodes apart

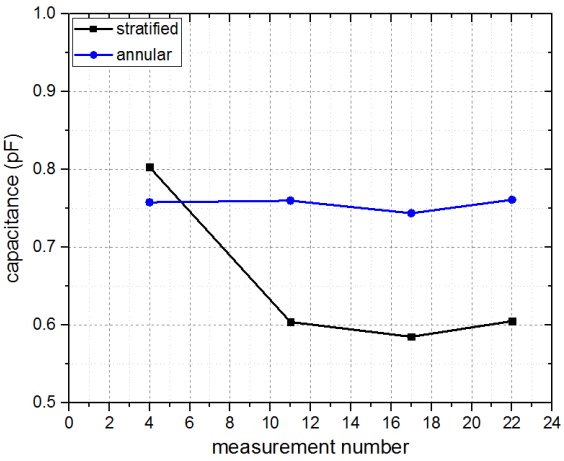

(d) Opposite electrodes

Figure 4.11: Capacitance measurement by electrode pair

Although either 1-electrode apart or 2-electrodes apart can be chosen for flow pattern identification, the selection needs to consider the sensitivity distribution of interest as well. To select only 1-electrode apart may cause low sensitivity of measurement at the centre region while selecting 2-electrode apart can provide minimal loss in the centre as it has lower measurement sensitivity at the peripheral area. Figure 4.12 illustrates both situations (1-electrode apart and 2-electrodes apart) with the possible low sensitivity region highlighted in black. Selecting both sets of data not only improves measurement sensitivity but also further signifies the difference between the stratified and annular flows.

(a) 1-electrode apart

(b) 2-electrodes apart

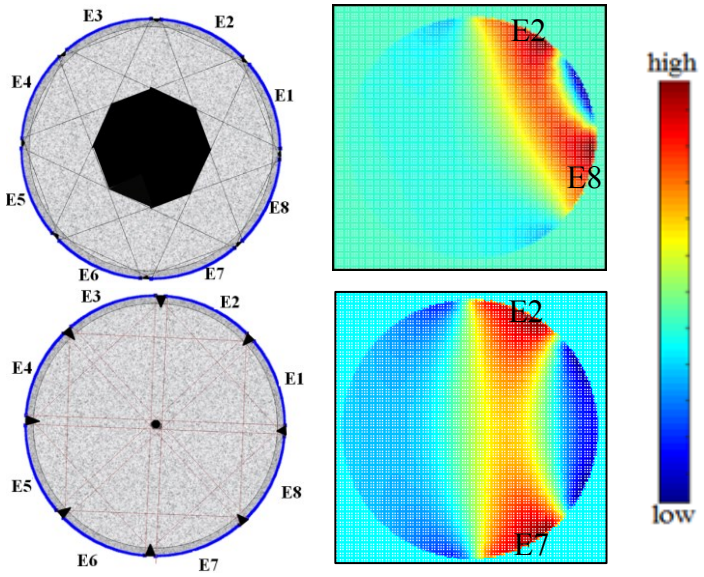

Figure 4.12: Coverage of measurement

a. *'Fingerprint' for capacitance data*

The plot of measured capacitance against WLR is shown in Figure 4.13. The WLR varies from 10% to 90%. Figure 4.13 (b) illustrates the magnified plot for measurement number 24. It shows a non-linear relationship at higher WLR (more than 50%).

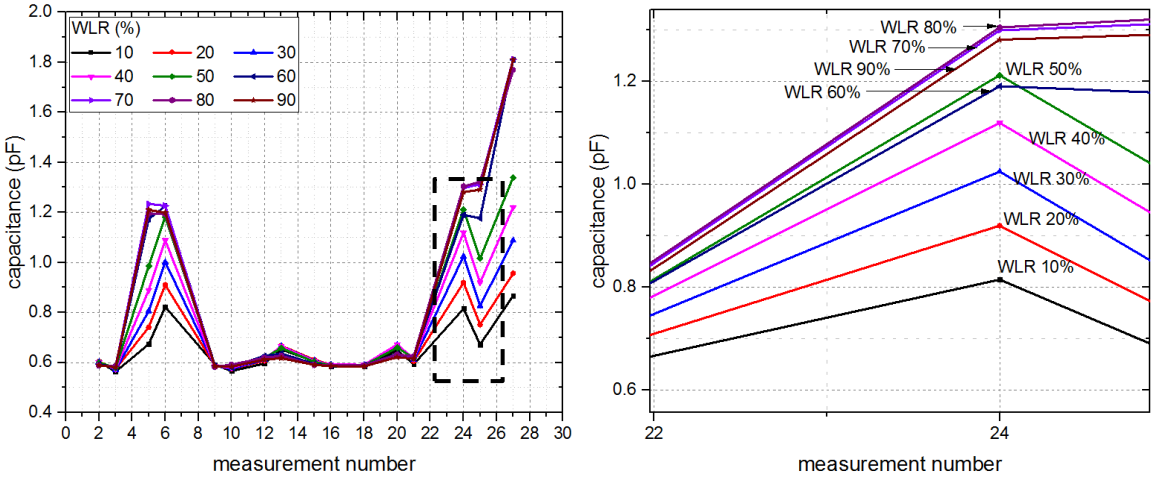

(a) 16 measurements (b) Measurement number 24

Figure 4.13: Capacitance against WLR for stratified flow

A similar behaviour is observed with the annular flow, as shown in Figure 4.14. With the WLR more than 50%, the relationship between capacitance and WLR is no longer linear. In addition, the separation between low and high WLR (considered the gap between 50% and 60%) is more obvious with the annular flow than with the stratified flow.

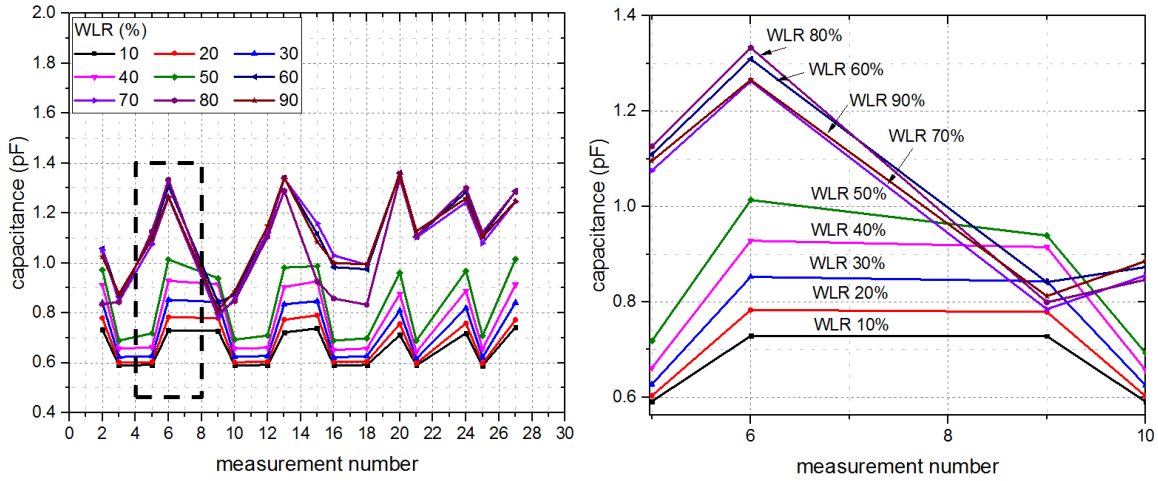

(a) 16 measurements (b) Measurement number 6

Figure 4.14: Capacitance against WLR for annular flow

As seen in Figure 4.13 and Figure 4.14, it can be confirmed that the stratified and annular flows maintain their own unique data patterns at any range of WLR. Therefore, each of the flow regimes can be represented by one set of identity data known as '*fingerprint'* (Xie *et al.*, 1989). Figure 4.15 shows the '*fingerprint'* for the stratified and annular flows obtained from the average value in Figure 4.13 and in Figure 4.14.

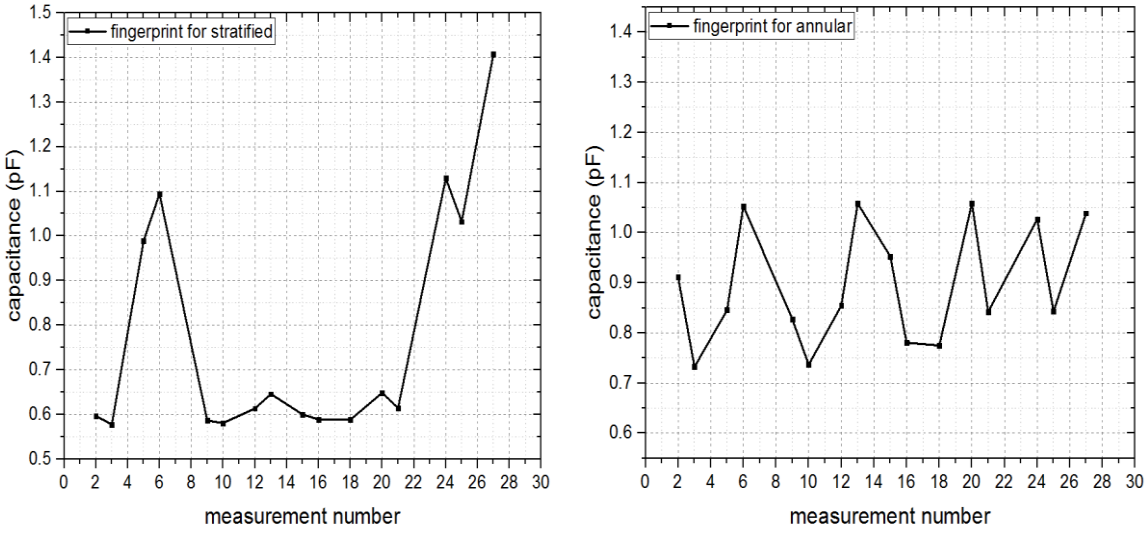

(a) Stratified (b) Annular

Figure 4.15: *'Fingerprint'* of stratified and annular flows from capacitance data

b. Euclidean distance calculation

The Euclidean distance or Euclidean metric refers to the straight distance between two points in the Euclidean space. With this distance, the Euclidean space becomes a metric space. The norm of the metric is called the Euclidean norm. In Cartesian coordinates, if $m = (m_1, m_2, \ldots, m_t)$ and $r = (r_1, r_2, \ldots, r_t)$ are the two points in the Euclidean space, then the distance (d) from m to r, or from r to m is given by the Pythagorean formula

$$d(r,m) = d(m,r) = \sqrt{(r_1 - m_1)^2 + (r_2 - m_2)^2 + \cdots + (r_t - m_t)^2} \qquad (4.1)$$

where r and m are the Euclidean vectors and t is the number of measurement between the points in the Euclidean space.

In this work, r and m represent the '*fingerprint*' and the measured capacitance C_m respectively. With the '*fingerprints'* of the standard flow patterns stored in the computer as a data bank (for stratified and annular), the identification of the flows can then

proceed by comparing any measurement capacitance, C_m with each of these '*fingerprints*'. The smaller the distance, $d_{(r,m)}$, the closer the distance between C_m and '*fingerprint*' value is. When the minimum value of $d_{(r,m)}$ is obtained, then it can be concluded that the flow pattern identification process is complete. Figure 4.16 illustrates the concept at a single point where $d_2<d_1$ (d_2 is the minimum); therefore, it is determined as an annular flow.

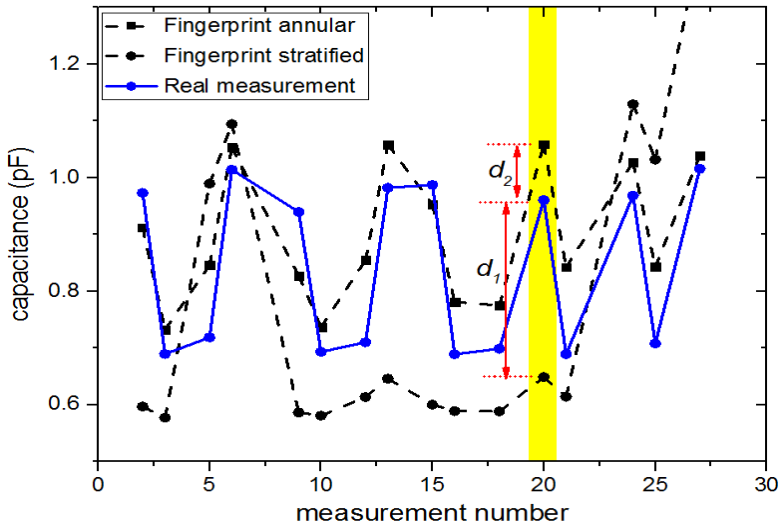

Figure 4.16: Euclidean distance for identifying stratified and annular flows

The flow chart of the flow regime identification process is shown in Figure 4.17.

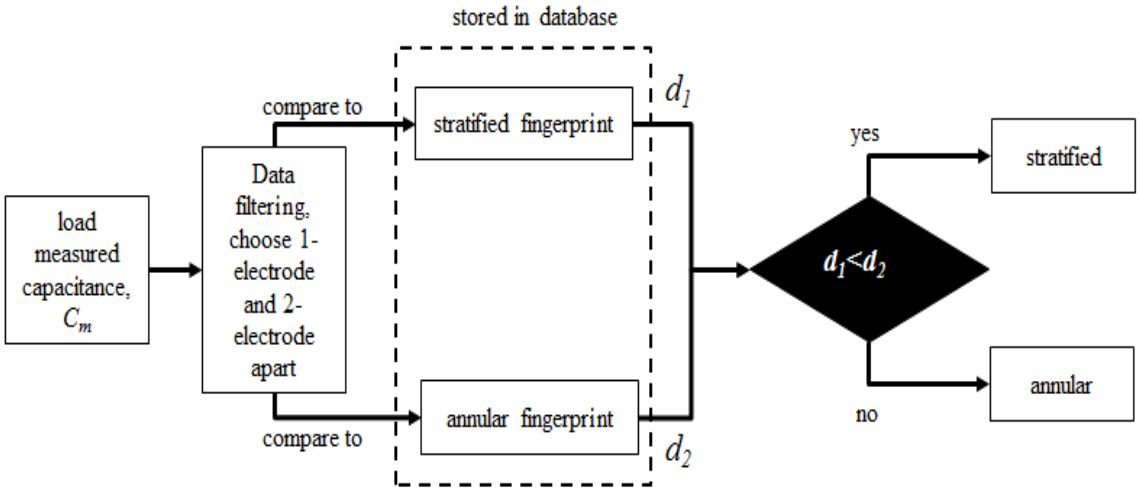

Figure 4.17: Flow regime identification process with Euclidean distance

The overall result of the flow regime identification with capacitance data is shown in Table 4.1. The compliance in detecting the stratified or annular flow of the emulsion was 100% through the adaptation of the *'fingerprint'* method and the Euclidean function.

Table 4.1: Flow regime identification result

Real flow regime	WLR (%)	d1	d2	Minimum	Predicted flow regime
Stratified	10	0.83	1.03	d1	Stratified
	20	0.65	0.93	d1	Stratified
	30	0.44	0.91	d1	Stratified
	40	0.24	0.93	d1	Stratified
	50	0.14	1.01	d1	Stratified
	60	0.48	1.32	d1	Stratified
	70	0.59	1.40	d1	Stratified
	80	0.54	1.36	d1	Stratified
	90	0.56	1.39	d1	Stratified
Annular	10	1.08	0.99	d2	Annular
	20	1.05	0.88	d2	Annular
	30	1.01	0.72	d2	Annular
	40	1.02	0.55	d2	Annular
	50	1.03	0.37	d2	Annular
	60	1.62	0.90	d2	Annular
	70	1.62	0.87	d2	Annular
	80	1.41	0.82	d2	Annular
	90	1.62	0.88	d2	Annular

4.3.2 Estimation of WLR with capacitance data

Figure 4.18 gives the corresponding mean capacitance from 28 measurements plotted against the WLR. The plot shows that for both flow regimes, the mean capacitance increases almost linearly from WLR 10% to 50%. When the WLR is greater than 50%, the relationship becomes non-linear. The possible reason for this non-linearity is that the phase has changed from oil-continuous to water-continuous flow. Therefore, the ECT is only possible to give an accurate estimation of WLR 50% and below.

To characterise ECT behaviour, the measurement data from WLR 10% to 50% were fitted. The graphs and coefficient values are shown in Figure 4.19. The estimation of WLR at maximum 50% calculated by the equations in Figure 4.19 is shown in Table 4.2. In this Chapter, the percentage of error is calculated by $(|Estimated\ WLR - Real\ WLR|/|Real\ WLR|)$X 100%. From Table 4.2, it shows that

the error rate is mainly lower with the annular flow than with the stratified flow. There is an outlier of 10% error for the stratified flow that could be due to the measurement error caused by the improper manual mixing of the emulsions.

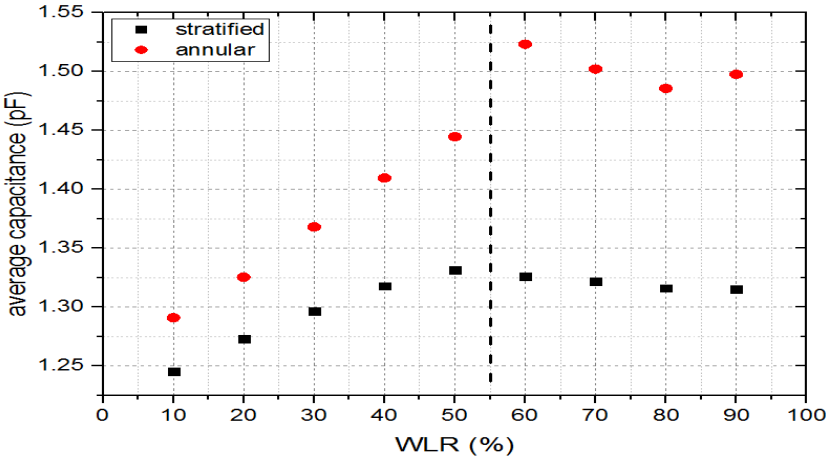

Figure 4.18: Average capacitance against WLR

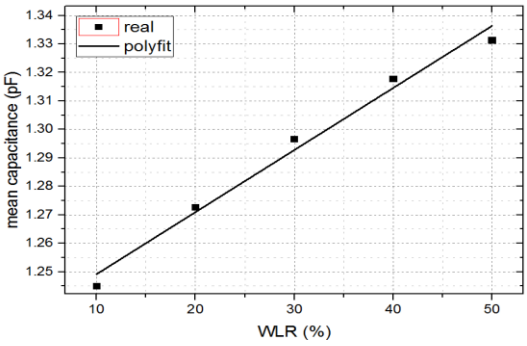

Intercept	1.2274
Slope	0.0022
Adj. R-Square	0.98
$WLR = (y - 1.2274)/0.00212$	

(a) Stratified

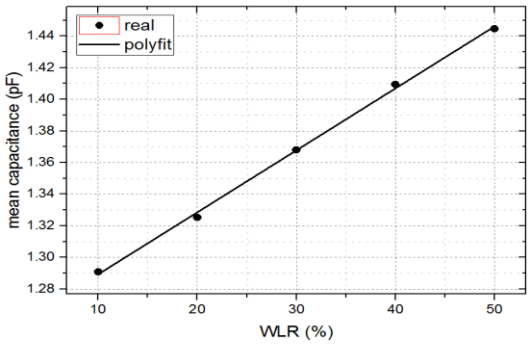

Intercept	1.2501
Slope	0.0039
Adj. R-Square	0.99
$WLR = (y - 1.2501)/0.0039$	

(b) Annular

Figure 4.19: Linear curve fit for capacitance data

Table 4.2: WLR estimation by capacitance data

Stratified			Annular		
Real WLR (%)	Estimated WLR (%)	Error %	Real WLR (%)	Estimated WLR (%)	Error %
10	9.0	10.0	10	10.4	4.0
20	20.6	3.0	20	19.2	4.0
30	31.7	5.7	30	30.1	0.3
40	41.5	3.8	40	40.6	1.5
50	47.7	4.6	50	49.6	0.8

4.4 Results from MRS

The measurement with MRS was carried out almost simultaneously with the ECT. The flow regime and the mixture ratio (water and oil) in volume (ml) are the same for both systems.

4.4.1 Resonant frequency and amplitude data analysis

The first resonant peak of emulsion with the stratified flow is shown in Figure 4.20. The amplitude of the resonant peak increases from WLR 10% to 50%, and then decreases from 60% onwards. On the other hand, the resonant frequency becomes lower as water level increases. The resonant frequency is the highest and lowest at WLR 10% and 90% respectively.

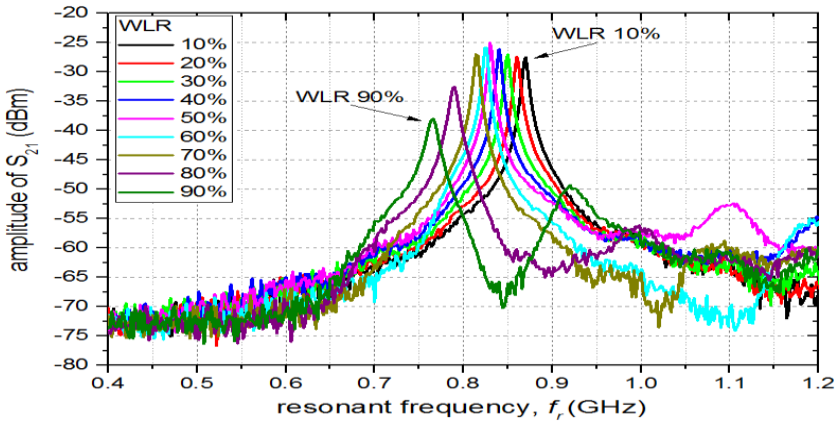

Figure 4.20: First resonant peak for stratified flow

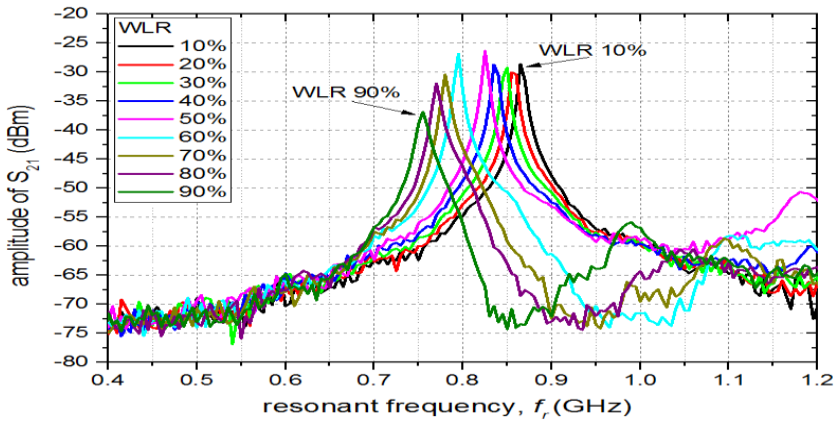

Figure 4.21: First resonant peak for annular flow

Figure 4.21 shows a similar data trend with the annular flow. The highest amplitude is found at WLR 50% while the lowest is at WLR 90%. The resonant frequency shifts to a

lower value as WLR increases. There is a noticeable gap between WLR 50% and WLR 60% in the annular flow compared to in the stratified flow.

Figure 4.22 summarises the amplitude of S_{21} plotted against WLR. It can be seen that the data trend for both flow regimes is similar. The amplitude is weakly dependent on the emulsion conductivity when the WLR is equal or less than 50%. The gradient of amplitude becomes significant with the WLR more than 50%, where a huge drop is observed (from WLR 60% to 90%). This result correlates very well with the explanation in Figure 4.9 and also with the capacitance response that shows non-linearity with the WLR of more than 50% (Figure 4.18). It can be concluded that the resonant-based measurement is capable of tracking the change of oil-continuous to water-continuous phase (Xie, 2007). For these specific types of emulsions and flow regimes, the transition phase from oil-continuous to water continuous is between WLR 50% and 60%.

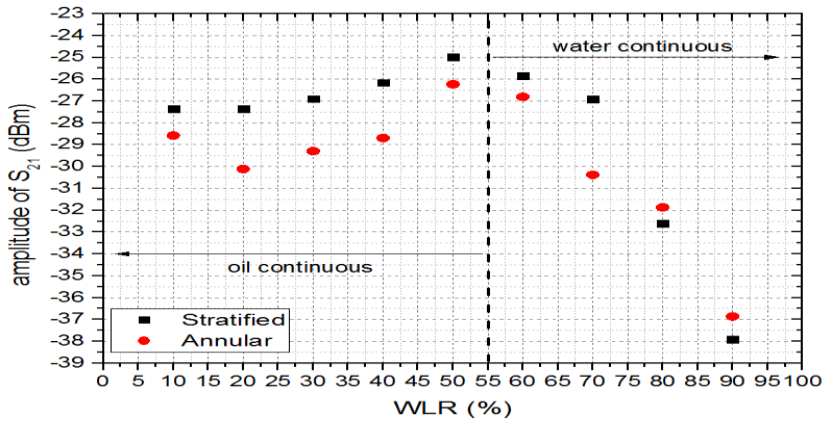

Figure 4.22: Amplitude of S_{21} against WLR

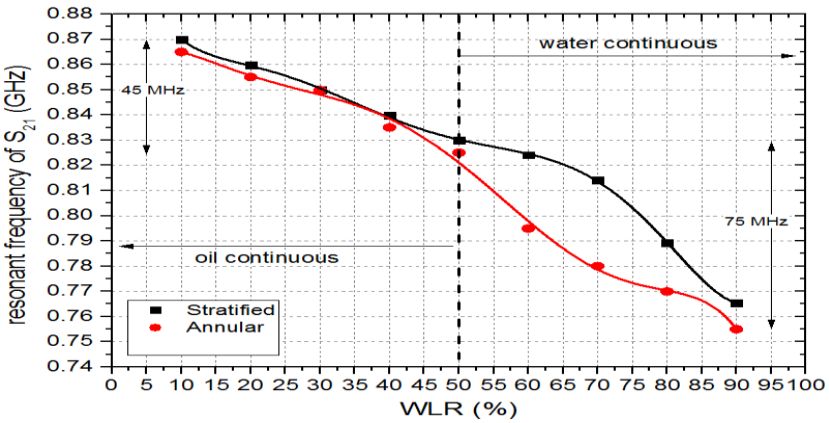

Figure 4.23: Resonant frequencies of S_{21} against WLR

The resonant frequency that corresponds to the WLR for the stratified and annular flows is shown in Figure 4.23. Overall, the resonant frequency is found to be inversely proportionate to WLR for both flow regimes. In the oil-continuous phase, the difference between the stratified and annular flows is minimal. However, the variance between the two graphs becomes more significant at water-continuous flow. The relationship can be used to characterise the sensor.

4.4.2 Estimation of WLR with resonant frequency data

In order to characterise the behaviour of the sensor, the resonant frequency data were fitted in a 4th order polynomial given by equation (4.2). The calculated coefficient values are shown in Figure 4.24 for each flow regime.

$$WLR(\%) = intercept + b_1 {f_r}^1 + b_2 {f_r}^2 + b_3 {f_r}^3 + b_4 {f_r}^4 \quad (4.2)$$

where f_r is the first resonant frequency in GHz.

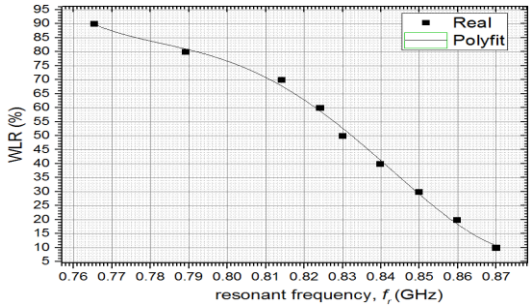

intercept	8.9721E5
b_1	-4.4303E6
b_2	8.1955E6
b_3	-6.7300E6
b_4	2.0696E6
Adj. R-Square	0.9934

(a) Stratified

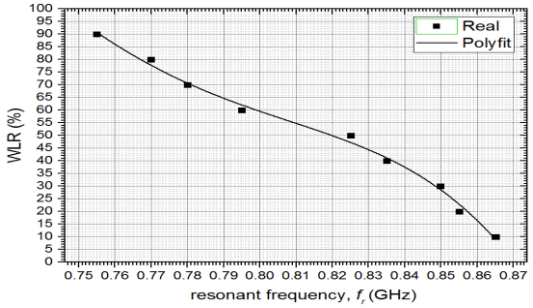

intercept	-1.2446E5
b_1	6.7431E5
b_2	-1.3574E6
b_3	1.2063E6
b_4	-3.9992E5
Adj. R-Square	0.9899

(b) Annular

Figure 4.24: Polynomial fitted graphs and coefficients with resonant frequency, f_r

Table 4.3 shows the estimation of WLR by adapting equation 4.2 and coefficients from Figure 4.24. The result shows high error of WLR from 10% to 50%, but the error rate improves when WLR is high. This could be due to the small margin of resonant frequency value in the oil-continuous flow. This phenomenon can be seen in Figure 4.23, where the range of resonant frequency (f_r) between WLR 10% and WLR 50% is

45 MHz which is small in comparison to WLR between 50% and 90% (**75** MHz). Therefore, the estimation of WLR is highly affected by the small change of frequency in the oil-continuous flow than in the water-continuous flow.

Table 4.3: WLR estimation with resonant frequency (f_r)

Stratified			Annular		
Real WLR (%)	Estimated WLR (%)	Error %	Real WLR (%)	Estimated WLR (%)	Error %
10	15.1	51.0	10	13.5	35.4
20	22.8	14.0	20	27.4	36.8
30	33.5	11.7	30	33.0	10.0
40	45.6	14.1	40	45.3	13.4
50	56.9	13.8	50	51.4	2.7
60	63.1	5.2	60	65.5	9.2
70	71.9	2.7	70	74.2	6.0
80	85.1	6.4	80	81.1	1.4
90	93.9	4.3	90	93.9	4.3

4.5 Integration of ECT and MRS

The capacitance and frequency against the WLR are plotted in one graph as shown in Figure 4.25. It can be seen that the two systems have a different trend in that with the increment of WLR, the capacitance increases, but the frequency decreases. Based on the obtained WLR shown in Tables 4.2 and 4.3, ECT and MRS work well in different phase. ECT can estimate WLR with low error percentage in an oil-continuous flow, but not performing good compared to MRS in the water-continuous flow. Therefore, a combination of both systems can optimise the WLR calculation for a more accurate estimation.

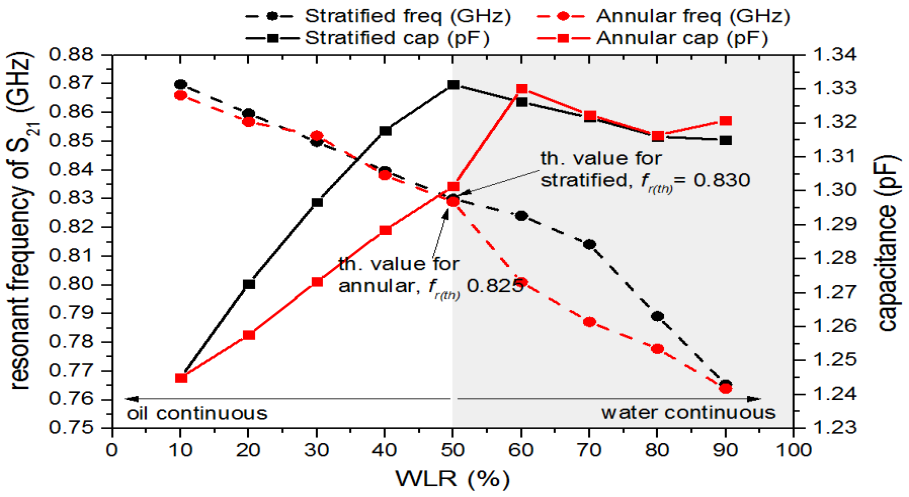

Figure 4.25: Combination of ECT and MRS

To combine ECT and MRS, this research proposes the use of a threshold value as the phase switching control parameter. The resonant frequency can be used as threshold values since there is no conflicting point within the range (WLR 10% to 90%), i.e. one WLR has only one assigned frequency. In reality, the phase transition could be anywhere between 50% and 60%, but for calculation simplicity, the value at 50% is chosen (one for each flow regime). Therefore, $f_{r(th)}$ = 0.830 GHz and $f_{r(th)}$ = 0.825 GHz are defined as the resonant frequency threshold values for the stratified and annular flow, respectively.

The flowchart of the dual-modality system is shown in Figure 4.26. There are two main tasks in this flow chart, (1) flow identification by capacitance data and (2) WLR estimation according to the defined continuous phase. The estimation of WLR with the new developed dual modality of ECT and MRS is summarised in Table 4.4.

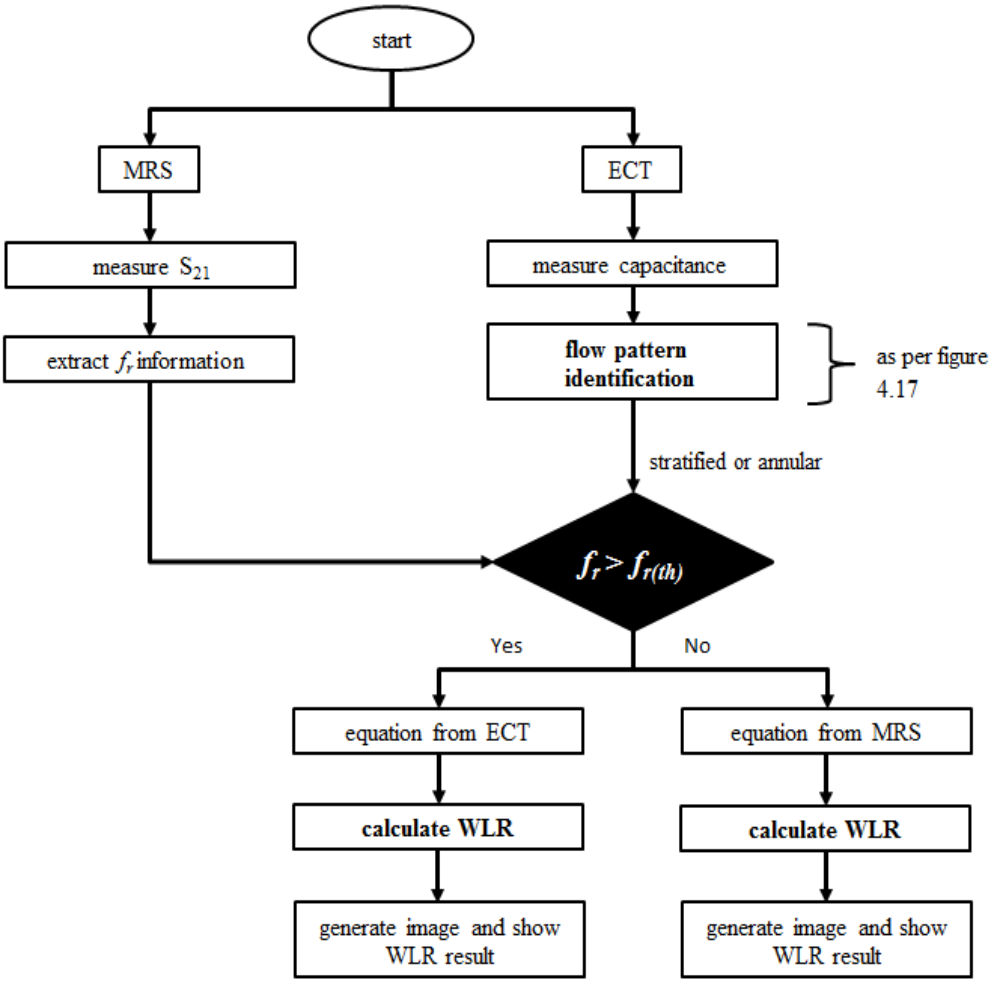

Figure 4.26: ECT-MRS system flowchart

Table 4.4 WLR estimation by ECT-MRS dual-modality system

Real WLR (%)	Estimated WLR (%)	
	Stratified	Annular
10	9.0	10.4
20	20.6	19.2
30	31.7	30.1
40	41.5	40.6
50	47.7	49.6
60	63.1	65.5
70	71.9	74.2
80	85.1	81.1
90	93.9	93.9

The results can be evaluated in two ways, (1) comparison to real WLR and (2) comparison between flow regimes.

a. Comparison with real WLR

Figure 4.27 shows the error calculated in comparison to real and estimated WLR for stratified and annular flow. The bar graph projects the individual error for each situation. The error rate varies, but in most conditions, the error is below 5%. There is one outlier with a high error rate for both flow regimes which may be caused by measurement errors related to the manual mixing of the emulsions. The annular flow has lower error rates in many conditions compared to the stratified flow.

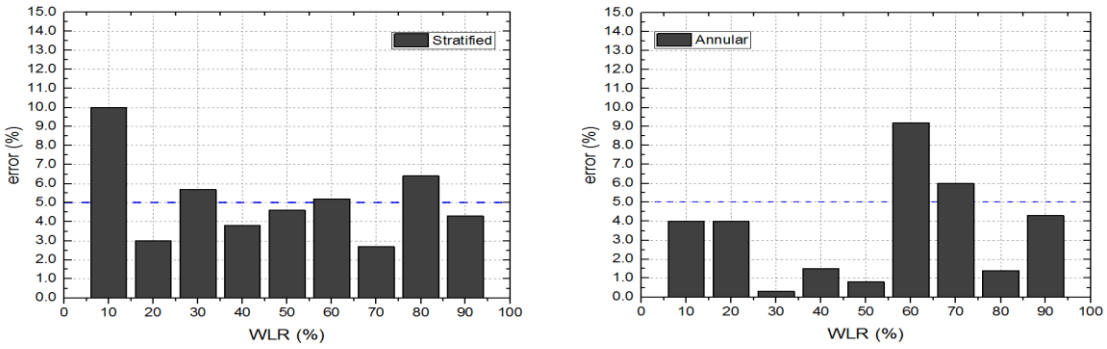

(a) Stratified (b) Annular

Figure 4.27: Error (%) between real and estimated WLR

b. Comparison between flow regime

The plot of estimated WLR against real WLR for the stratified and annular flows is shown in Figure 4.28. With a fixed volume of liquid and similar WLR, it is observed that there is no significant difference in the estimated WLR between the stratified and annular flows. Therefore, it can be concluded that the calculation of the WLR from this system is less dependent on the flow regimes.

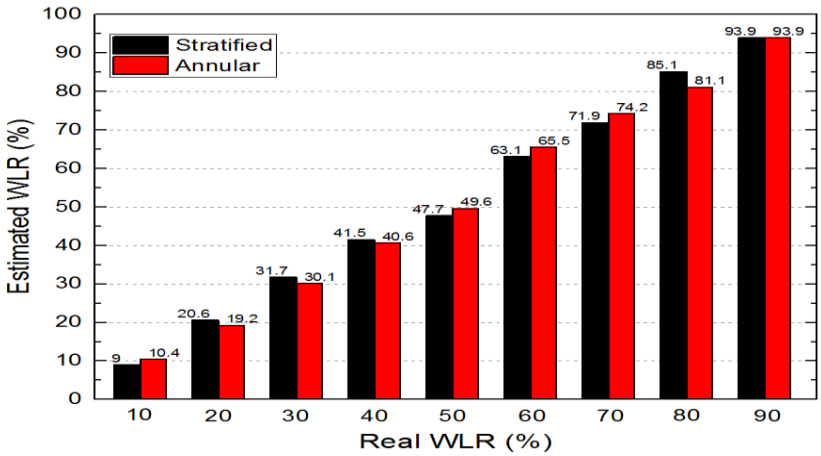

Figure 4.28: Estimated WLR (%) between flow regimes

4.6 Image generation and GUI

This graphical user interface was developed with MATLAB Version 2015b, using MATLAB Graphical User Interface Development Environment (known as Guide). It contains five major components: the Guide Control Panel, the Property Editor, the Callback Editor, the Menu Editor and the Alignment tool, all of which were used extensively during the development process. The pixel-based image is generated using common geometrical parameters with calculated minimum Euclidean distance as its variable input. Apart from the flow pattern, the image is made yellow and red to represent oil-continuous flow and water-continuous flow, respectively. Figure 4.29 illustrates examples of results when WLR is 20% and 80% for the stratified and annular flows.

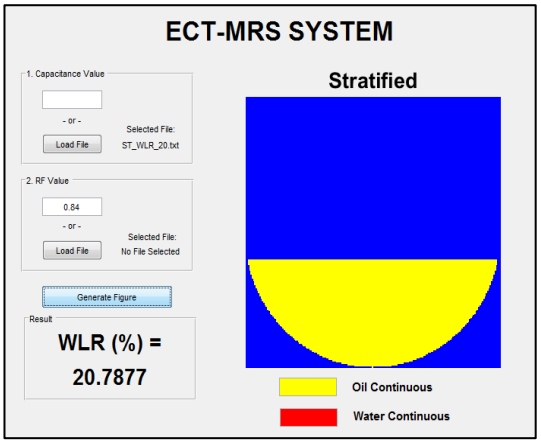

(a) Stratified, WLR 20%

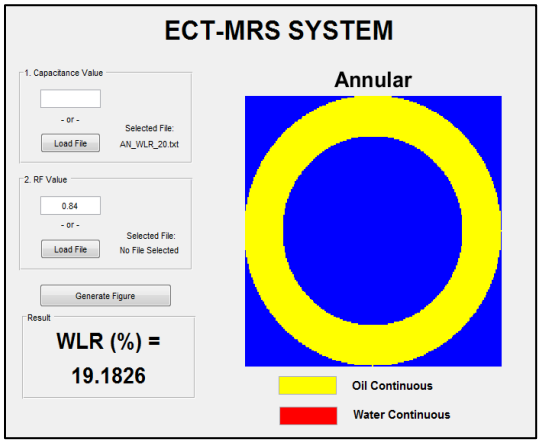

(b) Annular, WLR 20%

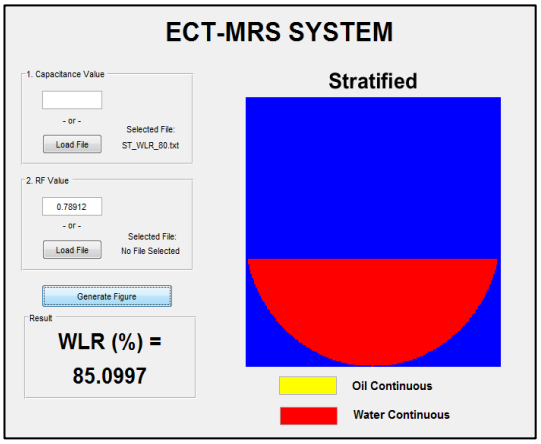

(c) Stratified, WLR 80%

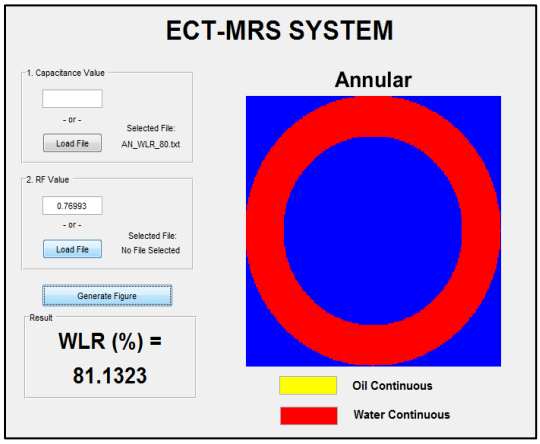

(d) Annular, WLR 80%

Figure 4.29: GUI for dual-modality ECT-MRS system (flow regime identification and WLR estimation)

4.7 Summary

This Chapter presents the first results of identifying flow regimes and estimating WLR from a dual-modality system of ECT and MRS. The characterisation was based on the capacitance and resonant frequency from the experiments conducted. From this work, it can be seen that the implementation of this new system is feasible and advantageous. The construction of such a system presents several improvements over a single modality system i.e. when ECT or MRS operates individually.

The use of this newly proposed dual-modality system provides more information on the multiphase flow in full-phase operation i.e. from oil-continuous to water-continuous flows. The system is 100% capable of identifying flow regimes (stratified or annular) at any WLR by using the capacitance data through the adaptation of the *'fingerprint'*

method and the Euclidean function. The results obtained from MRS showed similar data trend between stratified and annular flows; therefore, identification of flow regimes by MRS is not possible.

The system utilised the resonant frequency obtained from the MRS as an indicator (threshold value) of the phase transition and for estimating WLR in water-continuous flow. The overall initial estimation of WLR obtained from this ECT-MRS dual-modality system can be considered reasonable. Out of nine test conditions for each flow regime, 56% of the stratified flow and 77% of the annular flows are giving WLR error rate of less than 5%. With the same fraction and mixing ratio, there is no significant difference of estimated WLR between the stratified and annular flows. Therefore, it can be concluded that the estimation of the WLR is less dependent on the flow regimes.

The data processing uses raw capacitance and resonant frequency from the ECT and MRS; thus, a complicated calibration to specify measurement range is not needed. Unlike other proposed dual modality systems such as ECT and ERT or ECT and gamma-ray, this dual-modality of ECT and MRS is totally a non-radiation, non-intrusive and non-invasive system. The end results (flow regime and WLR) are projected instantaneously with a GUI. A simple image is visualised for the convenience of the end user. In addition, the MRS uses a portable device for measurements. Therefore, it is handy and does not need huge space for permanent and bulky machine installation.

Since this proposed system is new, there is still room for improvement. The error rate needs to be improved possibly by improvising the sensor design or by upgrading the algorithm for more control parameters. The system relies on the accuracy of the devices; therefore, it is essential that ECT and MRS have good reproducibility. For this work, device calibration has been done on both systems, and measurements with empty sensor were carried out and compared to the initial result before each session. The experiments have so far been conducted on lab-scale static flow; thus, future experiments should be more dynamic to resemble field (on-site) applications.

Chapter 5: Appraisal of sensitivity maps generated with different background

5.1 Introduction

Most researchers working on Electrical Capacitance Tomography (ECT) use only a set of generic sensitivity maps based on an empty background generated by dot multiplications. The fundamental of sensitivity map is explained in Section 2.5. A problem with the generic sensitivity maps is that in principle, they change with different permittivity distributions (Li and Yang, 2007). One possible solution to address this drawback is by updating the sensitivity maps according to the material or permittivity distribution.

This Chapter investigates whether or not a different permittivity background should be used for imaging different dielectric materials or specific flow regimes. Different types of sensitivity maps were generated and then used for image reconstruction. The appraisal was based on the image quality and numerical assessment.

The ECT is modelled with FEM solver, COMSOL Multiphysics. The generation of the sensitivity maps and image reconstruction were done in MATLAB. To verify the simulation results, an ECT sensor was used and experiments were carried out.

5.2 ECT sensor model

An ECT sensor model used for the generation and appraisal of the sensitivity map is shown in Figure 5.1. It consists of 12 measurement electrodes around a pipe of 126 mm in inner diameter. The pipe is made of glass (ε = 3.2) and the thickness is 2 mm. A copper screen is used to prevent surrounding noise and the gap between the screen and the electrodes is 10 mm. The electrode-to-gap ratio is 9:1. For 2D

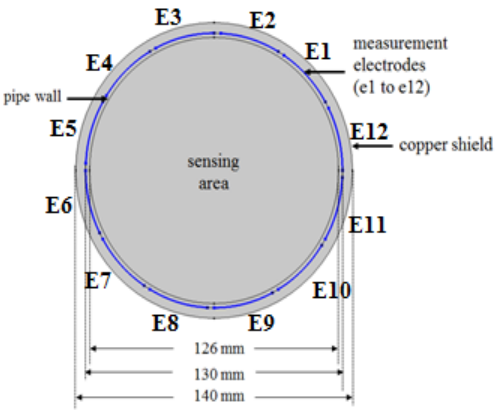

Figure 5.1: ECT sensor model

simulation, the length of the measurement electrodes is not considered. COMSOL Multiphysics software version 5.1 is used to obtain potential distributions. For a 12-electrode ECT sensor, there are 66 sensitivity maps as calculated by equation (2.1), the same number as the independent measurements. Because the ECT sensor was made symmetrical, only 6 sensitivity maps are unique in the ideal case that are the adjacent electrodes, 1-electrode apart, 2-electrodes apart, 3-electrodes apart, 4-electrodes apart and opposite electrodes. In this work, the analyses are on sensitivity maps of adjacent and opposite electrodes.

5.3 Flow regimes and test materials

To investigate the influence of sensitivity maps on reconstructed images, stratified and annular distributions are selected as shown in Figure 5.2. Images were reconstructed with two types of objects independently: (1) flour (ε = 5) and (2) de-ionized water (ε = 80) as representations of low permittivity and high permittivity materials, respectively. In the figure, red represents the material, and blue represents the empty space (ε = 1).

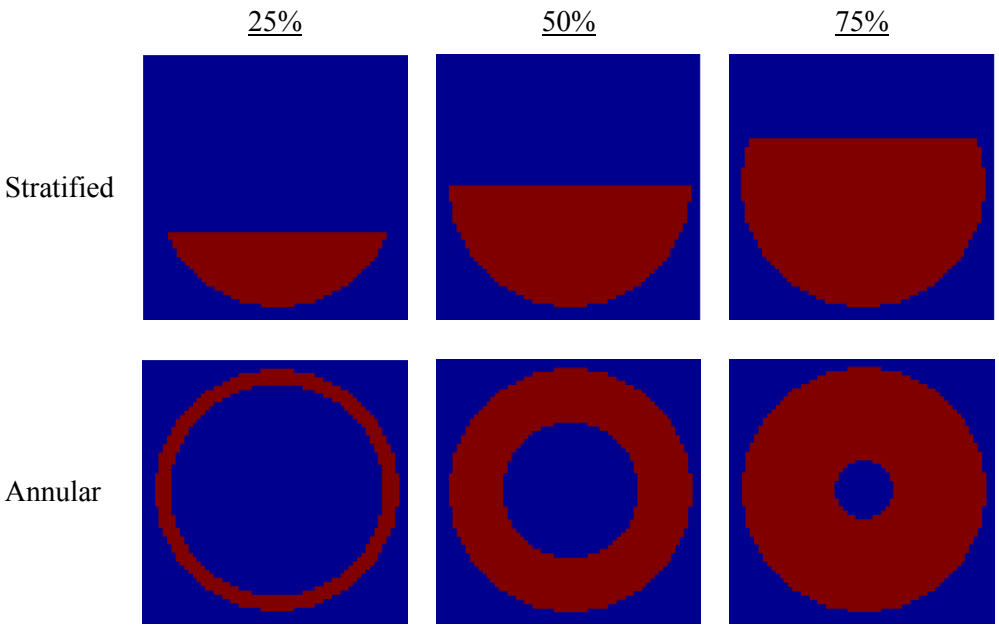

Figure 5.2: Flow regimes

5.4 Generation of sensitivity maps

Table 5.1 lists three types of sensitivity maps generated: (1) SM1, (2) SM2 and (3) SM3. Each of them was generated by dot multiplication when the sensor model is fully filled with the assigned material. SM1 was a generic sensitivity map with empty space

as the background, SM2 with wheat flour and SM3 with de-ionised water. To generate the sensitivity maps in MATLAB, the sensing area was divided into 64×64 pixels. For simplicity, in the following sections, the terms SM1, SM2 and SM3 are used as representations of the sensitivity maps. Wheat flour and de-ionized water will be referred to as flour and water.

Table 5.1: Types of sensitivity maps

	Material	Sensitivity map abbreviation
(a)	Air ($\varepsilon = 1$)	SM1
(b)	Wheat flour ($\varepsilon = 5$)	SM2
(c)	De-ionized water ($\varepsilon = 80$)	SM3

5.4.1 Potential distribution

Figure 5.3 shows the electric potential distributions obtained using COMSOL. It was observed that the potential distribution of SM1 and SM2 is similar to each other, however, the coverage and intensity of the surface potential are slightly lower with SM2. The potential distribution for SM3 is weak in the sensing region with a steep gradient at the boundary because high permittivity of water (ε=80) significantly decreases the electric field between the electrodes in the sensing area. A strong peak at the boundary is caused by the pipe wall despite being thin with 2 mm in thickness.

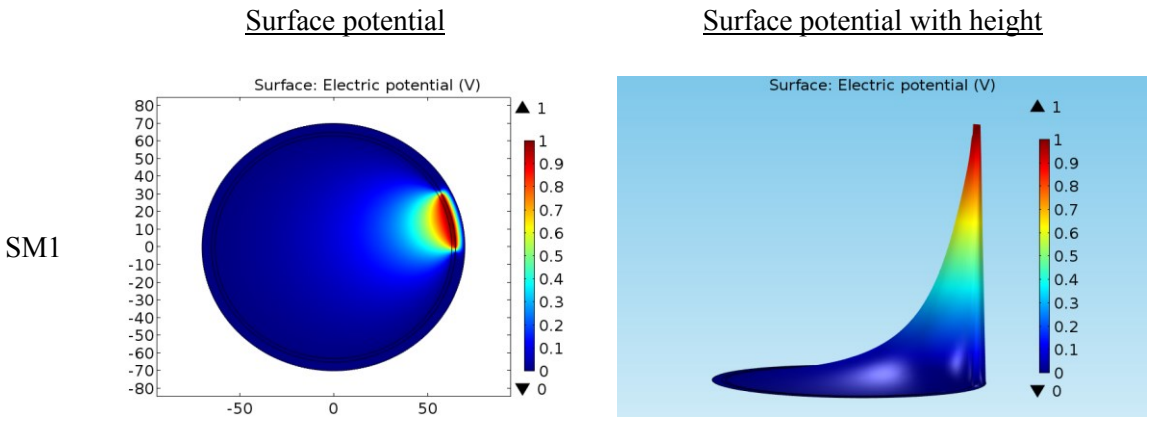

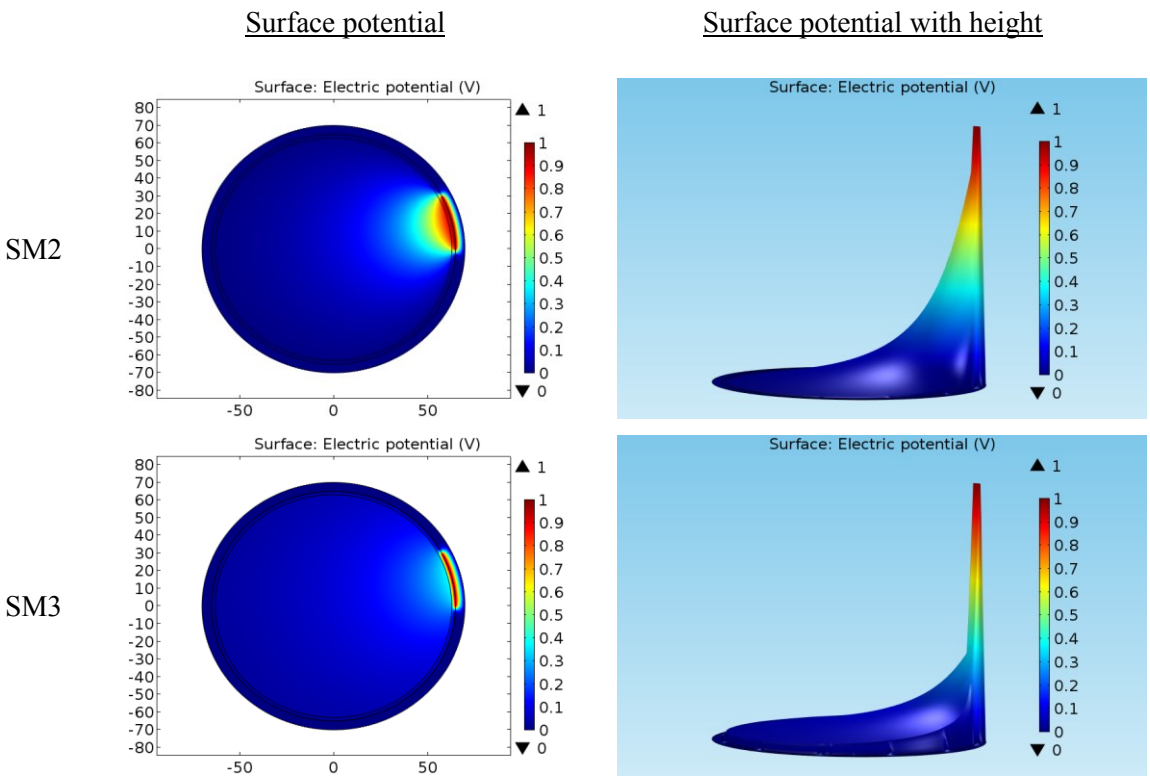

Figure 5.3: Potential distributions

5.4.2 Generated sensitivity maps

To generate a sensitivity map, the obtained electrical potential distributions between an excitation electrode and a detection electrode were dot-multiplied. Figure 5.4 shows the generated sensitivity maps: (1) SM1, (2) SM2 and (3) SM3 for adjacent and opposite electrodes. These sensitivity maps were generated exclusive of the pipe wall. In general, the sensitivity is low at the area where the potential data is weak. It can be seen that the highest sensitivity is SM1, for both adjacent and opposite electrodes. There is insignificant difference between SM1 and SM2. With water (SM3), the sensitivity continues to exist but the value is very small (*y*-scale reduced to $x10^{-5}$) in correspond to its value of electric potential data.

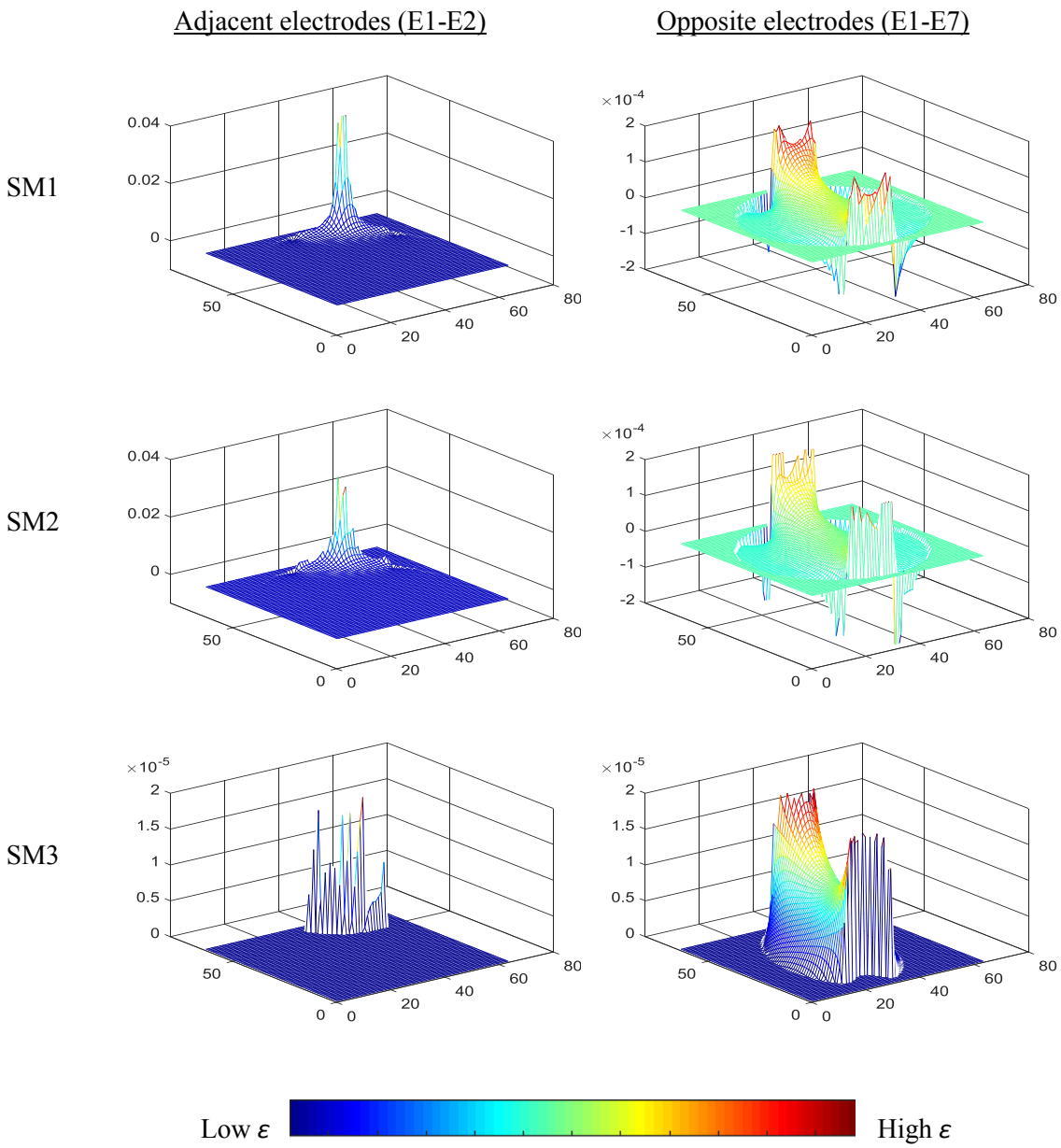

Figure 5.4: Sensitivity maps from dot multiplication

5.5 Image reconstruction

For the image reconstruction, LBP algorithm is employed because it is simple, fast and adequate for the purpose of appraising the sensitivity maps. The principle of LBP can be referred in Section 2.6. The real permittivity distributions (phantoms) are as shown in Figure 5.2.

5.5.1 Reconstructed images from simulated data

Figure 5.5 and Figure 5.6 show images of flour distribution reconstructed with SM1 in comparison with SM2. The quality of the images reconstructed with SM1 and SM2 is

similar to each other for both the stratified and annular distributions. Figure 5.7 and Figure 5.8 show the images of water distribution reconstructed with SM1 in comparison with SM3. For the stratified distribution of water, the quality of images with SM1 is good. The images of annular water layers reconstructed with SM3 are thinner in comparison with SM1. The most difference is with the annular 25% distribution where it has an extremely thin layer.

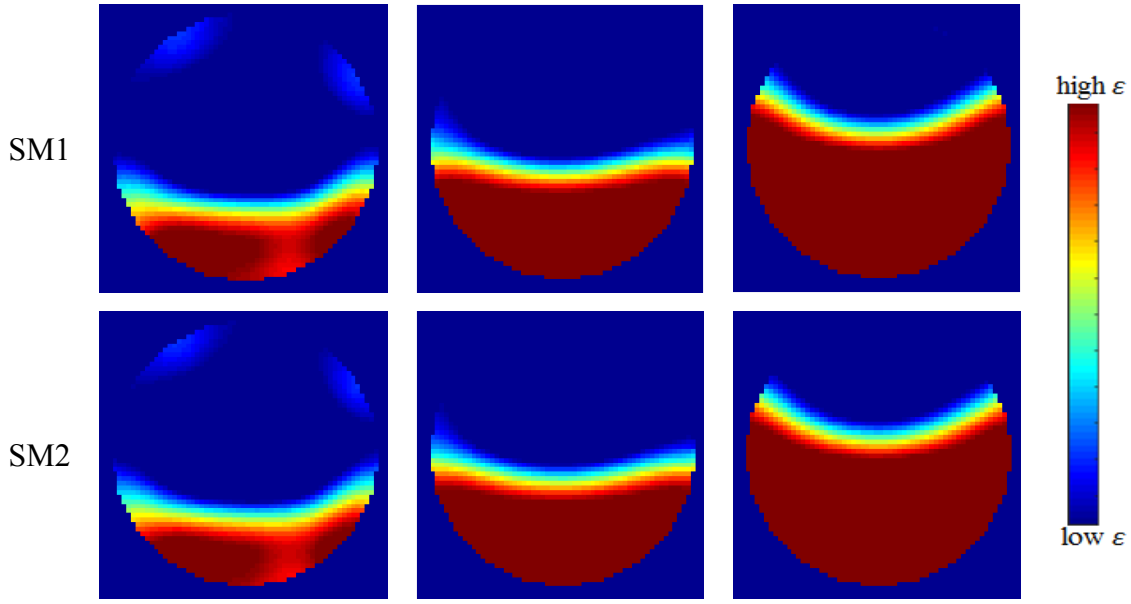

(a) 25% (b) 50% (c) 75%

Figure 5.5: Simulated stratified flour distributions

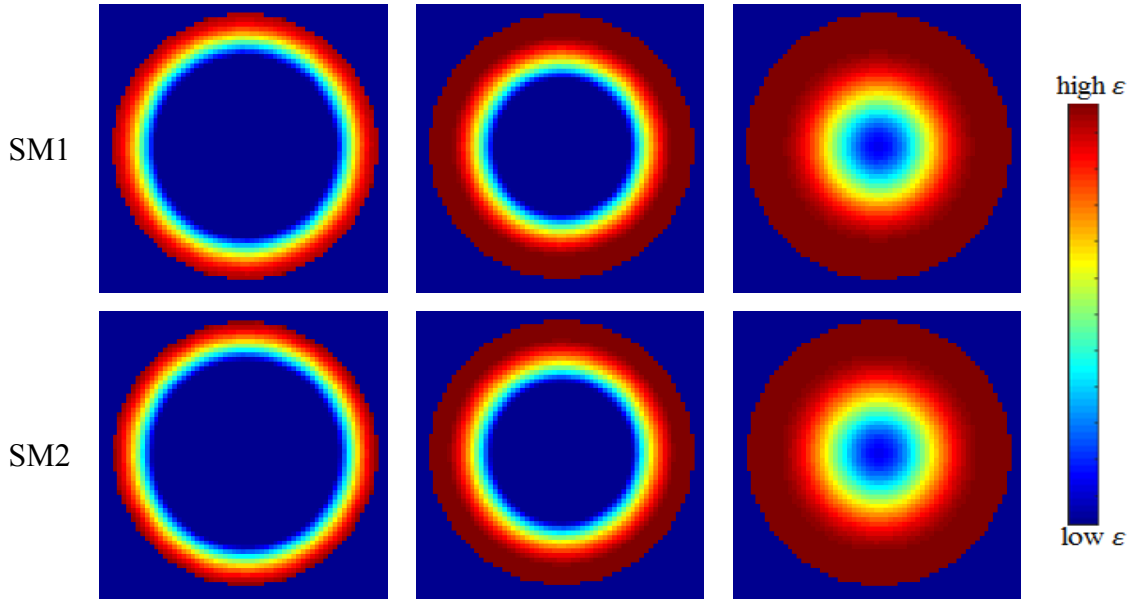

(a) 25% (b) 50% (c) 75%

Figure 5.6: Simulated annular flour distributions

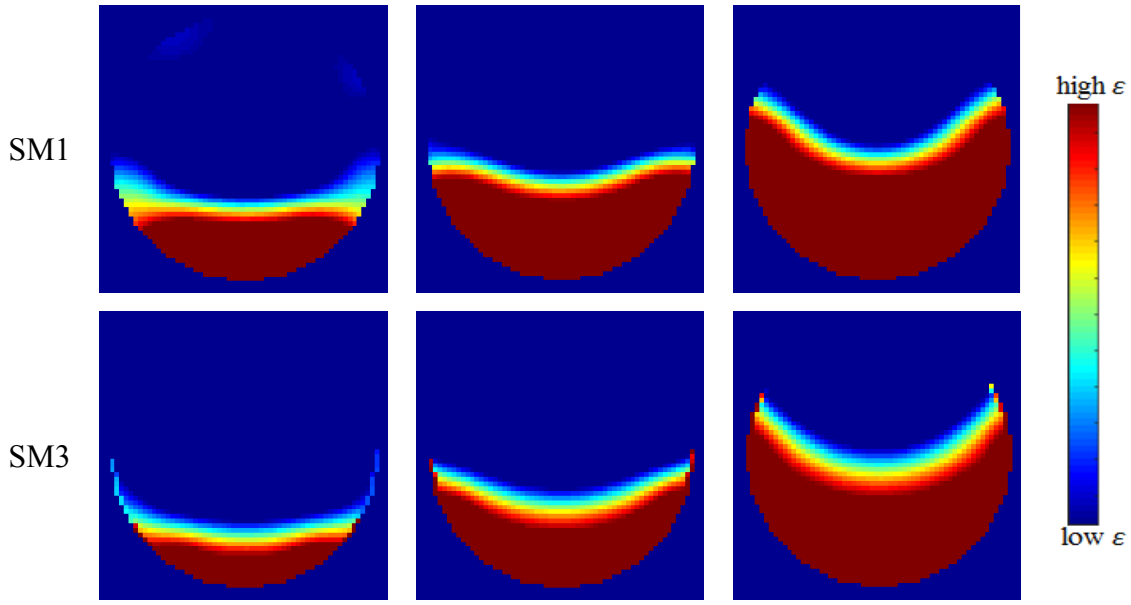

(a) 25% (b) 50% (c) 75%

Figure 5.7: Simulated stratified water distributions

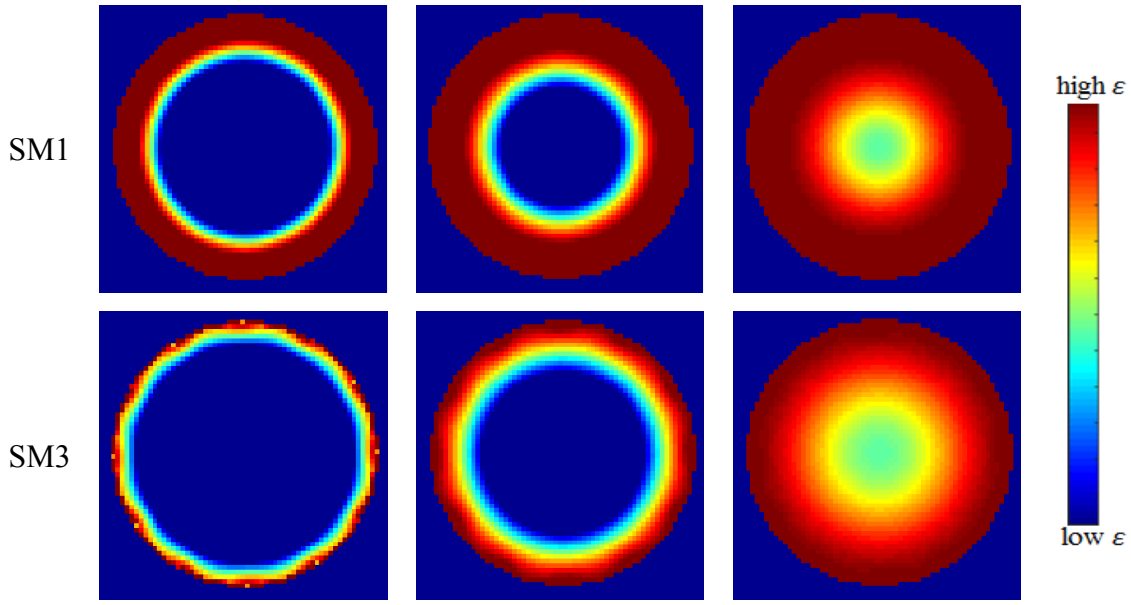

(a) 25% (b) 50% (c) 75%

Figure 5.8: Simulated annular water distributions

5.5.2 Error and correlation coefficient calculation

Although the images can be visually assessed, numerical assessment is more appropriate in estimating the measurement accuracy. To assess the quality of image reconstruction, image error and the correlation coefficient between the reconstructed and real permittivity distribution are calculated (Ye and Yang, 2013). The real permittivity distributions were obtained based on the models in Figure 5.2, simulated with COMSOL and MATLAB.

$$Image\ error = \frac{\|\hat{g} - \tilde{g}\|}{\|\tilde{g}\|} \times 100\% \tag{5.1}$$

$$Correlation\ coefficient = \frac{\sum_{i=1}^{Np}(\hat{g}_i - \bar{\hat{g}})(\tilde{g}_i - \bar{g})}{\sqrt{\sum_{i=1}^{Np}(\hat{g}_i - \bar{\hat{g}})^2 \sum_{i=1}^{Np}(\tilde{g}_i - \bar{g})^2}} \tag{5.2}$$

where $\tilde{g}$ is the normalised real permittivity distribution, $\hat{g}$ is the estimated permittivity distribution, $\bar{\hat{g}}$ and $\bar{g}$ are the mean values of $\tilde{g}$ and $\hat{g}$ respectively, N_p is the number of pixel (in this work N_p = 4096). Basically a lower image error and higher correlation coefficient indicates better image quality.

Figure 5.9 and Figure 5.10 show the calculated image errors and corresponding correlation coefficients of flour and water distributions for all fractions (25%, 50% and 75%). Each graph shows a comparison between generic sensitivity maps (SM1) and SM2 and SM3 separately according to their materials (SM1 versus SM2, SM1 versus SM3). Image error is calculated in percentage.

It is observed that for the stratified flour distribution in Figure 5.9 (a), the image errors for all fractions are less than 40% with SM1. The difference between images reconstructed with SM1 and SM2 is not significant. In Figure 5.9 (b) for the annular distribution, the highest error is found on the image with 25% flour reconstructed with SM1, that is 52% in comparison with SM2, 46%. The other 50% and 75% distributions are good with SM1.

Figure 5.9 (c and d) shows the image error for water distributions. SM1 gives lower image error for all stratified distributions. A significant difference is found in comparison of SM1 and SM3 with 25% water fraction for each of the flow regime. The image error with a huge difference between the sensitivity maps is with annular distribution and 25% water fraction. The image error is 80% with SM1 and 32% with SM3.

The correlation coefficient shown in Figure 5.10 is scaled from 0 to 1. It is observed that the results correlate to the image error for all conditions and materials i.e. a lower image error shows a higher value of correlation coefficient. The variance is minimal for flour distribution when comparing SM1 and SM2. The difference is more notable for water distribution.

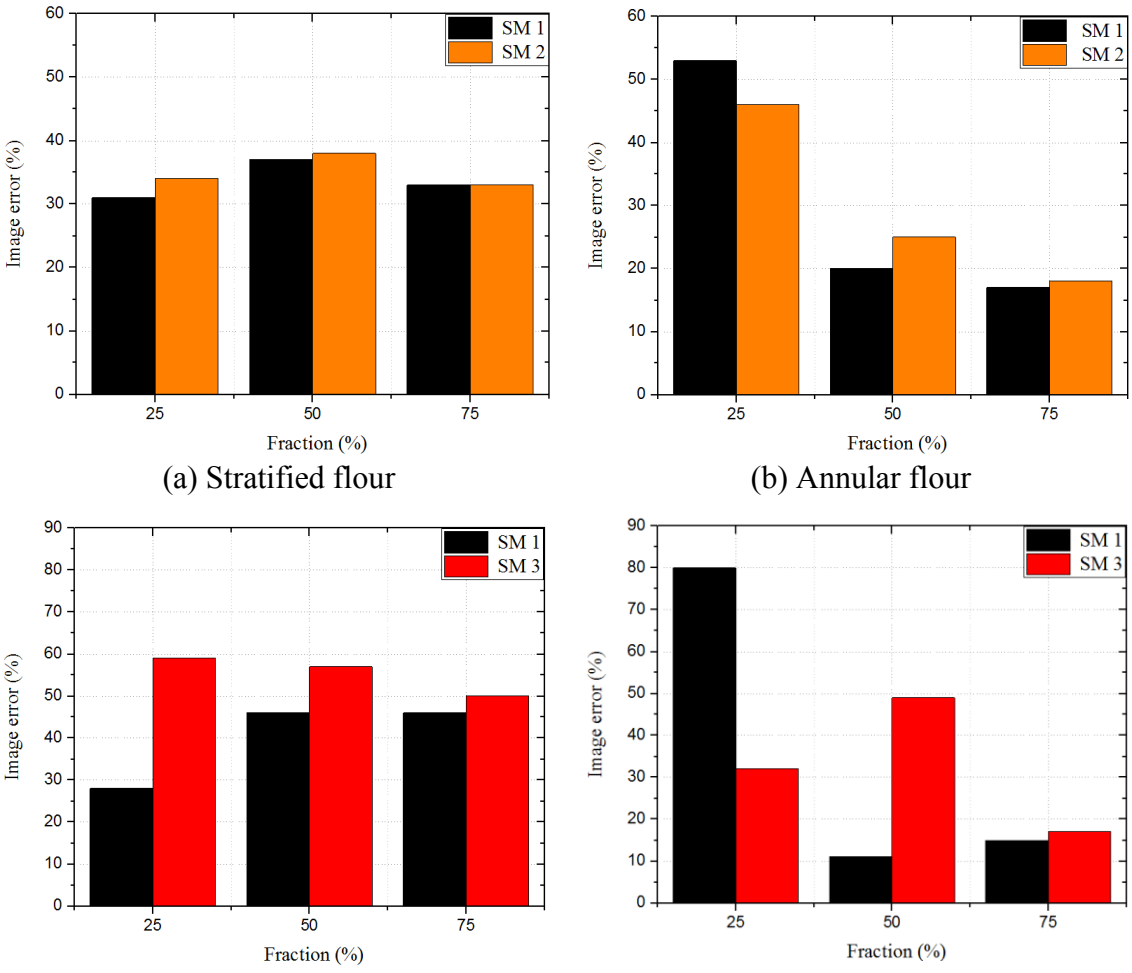

(a) Stratified flour (b) Annular flour

(c) Stratified water (d) Annular water.

Figure 5.9: Image error

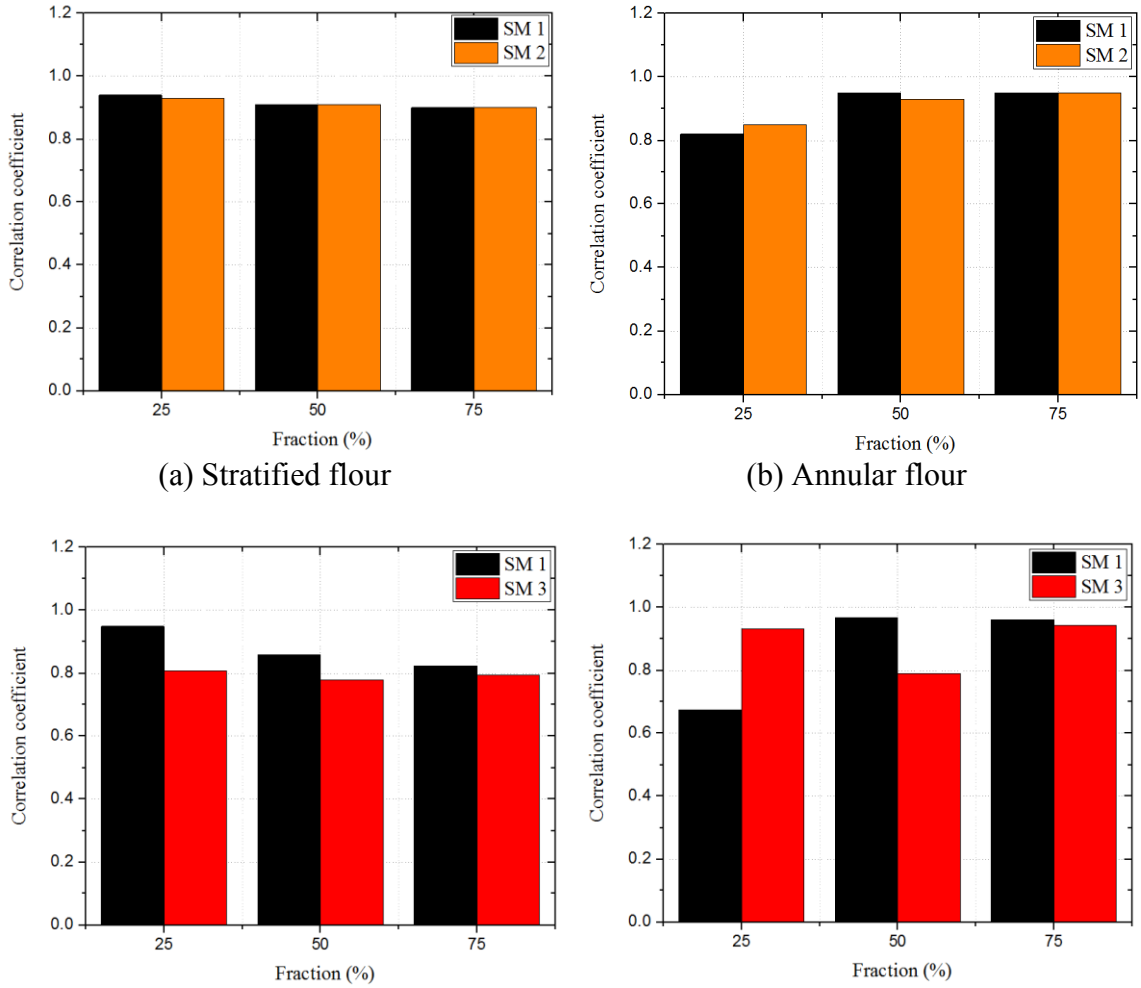

(a) Stratified flour (b) Annular flour

(c) Stratified water (d) Annular water.

Figure 5.10: Correlation coefficient

5.5.3 Reconstructed images from experimental data

Figure 5.11 shows the ECT system set-up for the experiment. To verify the simulation results, a 12-electrode ECT sensor was manually built in the lab at the University of Manchester. The sensor was fabricated using borosilicate glass beaker with 185 mm in height and 130 mm in external diameter. The electrodes and earth screen were made of copper tape and copper plate respectively. An impedance analyser (HP4192A) as described in Section 2.3 was used together with a 96-channel multiplexer to measure capacitance. The capacitance data from the sensor fully filled with flour and water were used as C_H, whilst the capacitance from empty sensor was used as C_L for the calibration purpose as according to equation (2.7).

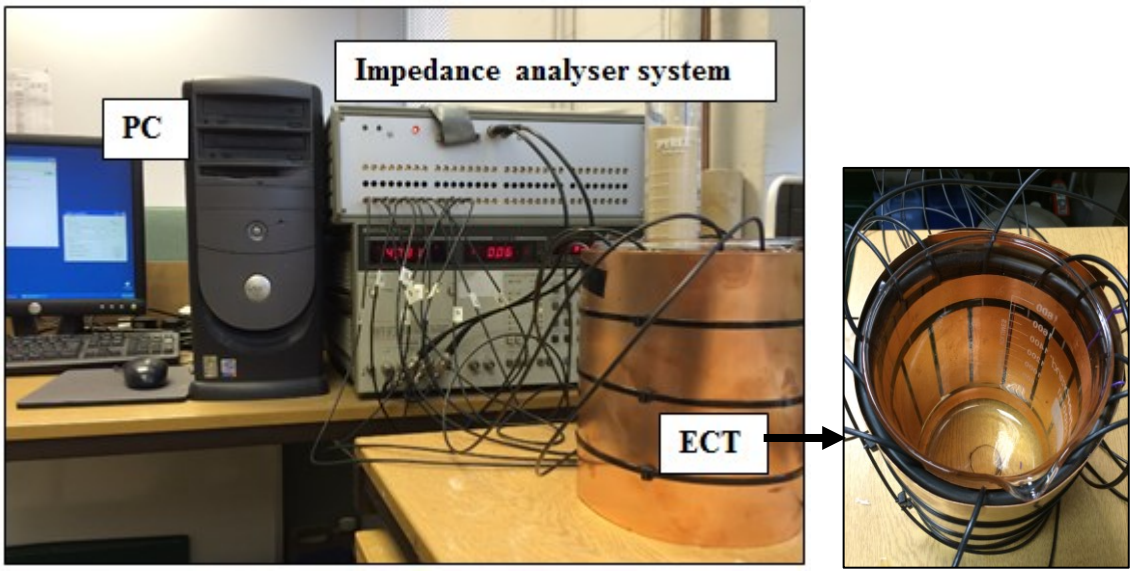

Figure 5.11: Impedance analyser-based ECT system.

Figure 5.12 and Figure 5.13 show the images reconstructed with flour distribution whilst Figure 5.14 and Figure 5.15 show the images for water distribution. All four figures show good correlation between simulation and experimental results.

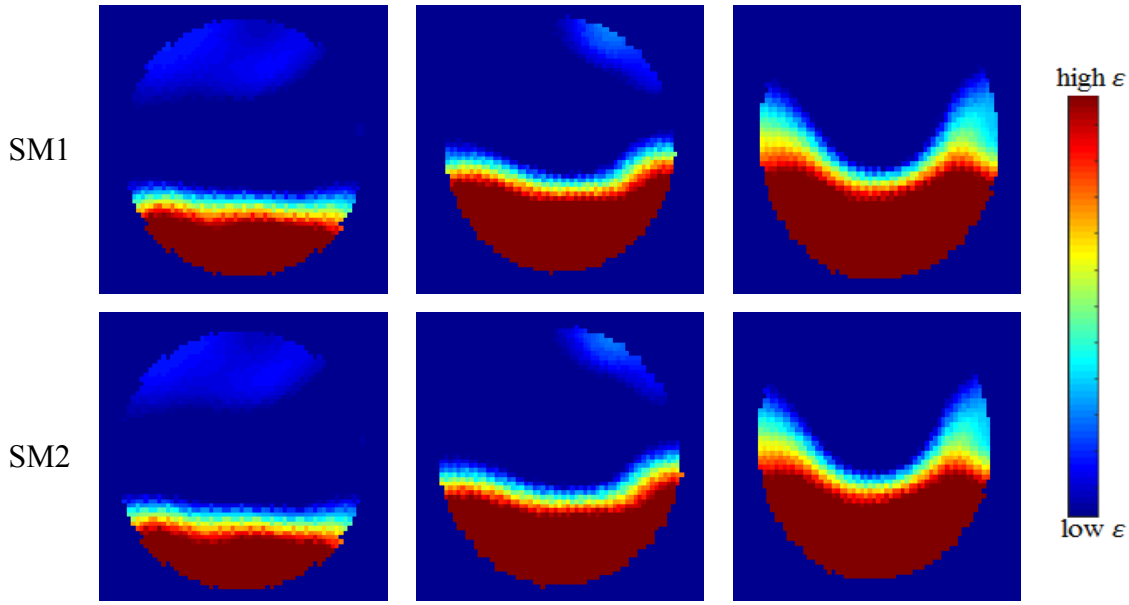

(a) 25% (b) 50% (c) 75%

Figure 5.12: Experimental stratified flour distributions

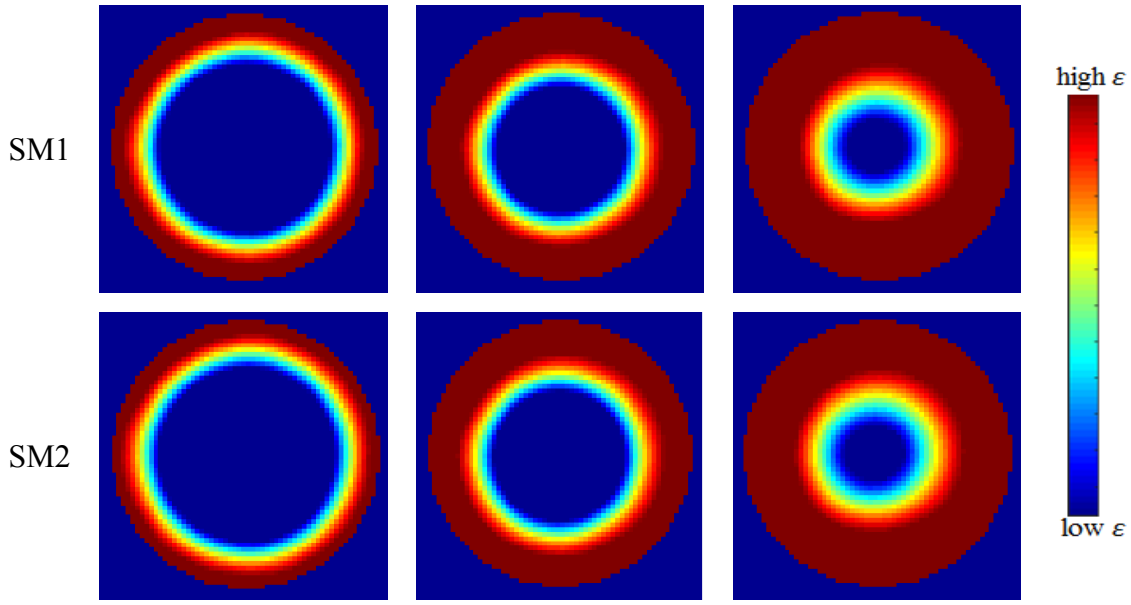

(a) 25% (b) 50% (c) 75%

Figure 5.13: Experimental annular flour distributions

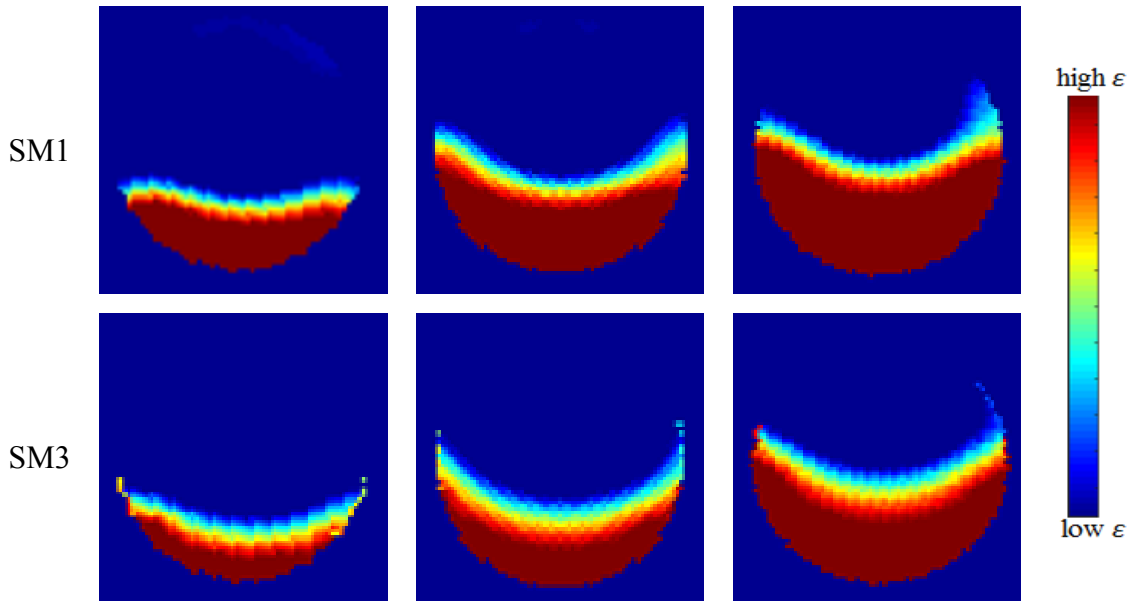

(a) 25% (b) 50% (c) 75%

Figure 5.14: Experimental stratified water distributions

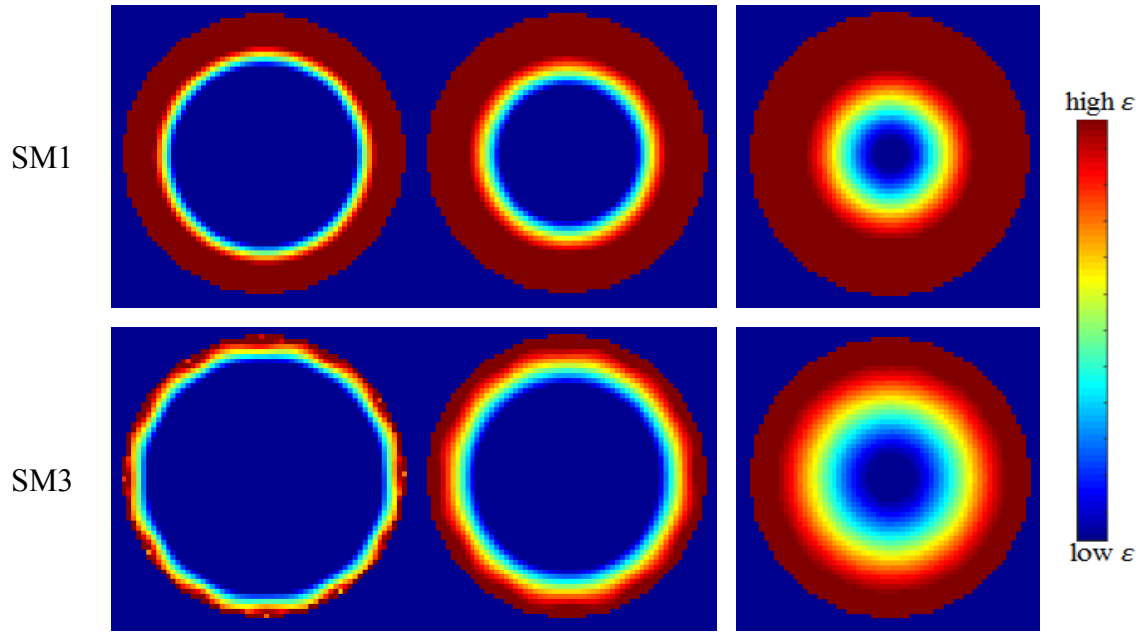

(a) 25% (b) 50% (c) 75%

Figure 5.15: Experimental annular water distributions

5.6 Summary

In this Chapter, different sensitivity maps are investigated according to the permittivity of the test material and its distribution, i.e. stratified or annular.

Three materials were used to generate sensitivity maps and as test objects, air (ε = 1), flour (ε = 5) and de-ionised water (ε = 80) that represent low and high permittivity materials respectively. The sensitivity maps are evaluated by image reconstruction using LBP algorithm. Simulation and experiment were carried out with a 12-electrode ECT sensor. The result shows that majority conditions are satisfactory with the generic sensitivity maps (SM1). The summary of recommended sensitivity map for each permittivity distribution is given in Table 5.2.

Table 5.2: Recommended sensitivity maps according to permittivity distribution

Material	Flour			Water		
Flow	25%	50%	75%	25%	50%	75%
Stratified	**SM1**	**SM1**	**SM1**	**SM1**	**SM1**	**SM1**
Annular	**SM2**	**SM1**	**SM1**	**SM2**	**SM1**	**SM1**

It is recommended to consider the sensitivity of its own material (in this case SM2 for flour and SM3 for water) if thin annular distribution is expected. A possible implementation of these sensitivity maps can be for a situation that has a thin layer of the outer pipe, for example, wet-gas separation after a pre-conditioning process.

The work is important as it helps in making a decision as to whether or not different sensitivity maps should be used for imaging different materials and flow regimes. There are more options of sensitivity maps to suit the applications rather than only one generic sensitivity map for all cases.

Chapter 6: Imaging different permittivity materials and wet granules with ECT and MWT

6.1 Introduction

This research is a collaboration project between the University of Manchester, UK and the Institute of Engineering Thermophysics (IET), Chinese Academy of Sciences, Beijing, China on the application of fluidised bed processes.

The moisture content of granules in a fluidised bed for a drying, granulation or coating process is typically between 1% and 25% which causes a change in permittivity during the process. In such a condition, the application of ECT has some limitations due to the effect of the moisture. As MWT has a wide range of frequency (1 GHz~2.5 GHz) and can be used to measure materials with high permittivity and conductivity, the aim of this research was to compare capacitance and MWT based on the characteristics of the image.

The specific objectives were to (1) analyse the effect of flow pattern and (2) analyse the effects of moisture on the quality of image reconstruction. Unlike the dual modality of ECT and MRS that uses a signal processing technique, the dual combination of ECT and MWT employed the tomographic techniques that require solving forward and inverse problem to reconstruct images as explained in Chapter 2 and Section 3.2.

6.2 ECT-MWT system

Figure 6.1 shows the overall system used in this research. A vertical Plexiglass tube of 5 mm in thickness is used to accommodate the test material and to hold the sensors. The height of the tube is 500 mm, and the inner diameter is 150 mm. A 12-electrode ECT sensor was built in the lab at the IET according to the size of the tube. The electrodes were made of copper tape and the electrode-to-gap ratio is 9:1. The length of the electrode is 100 mm. The ECT electrodes are shielded with a copper plate to reduce surrounding noise. In this experiment, the AC-based measuring circuit with 16 channels was employed, alongside with the MWT system as explained in Section 3.2. The MWT

sensor was placed at the top part of the tube. The gap between the ECT and MWT sensor is 50 mm, with insulation placed in between to avoid interference.

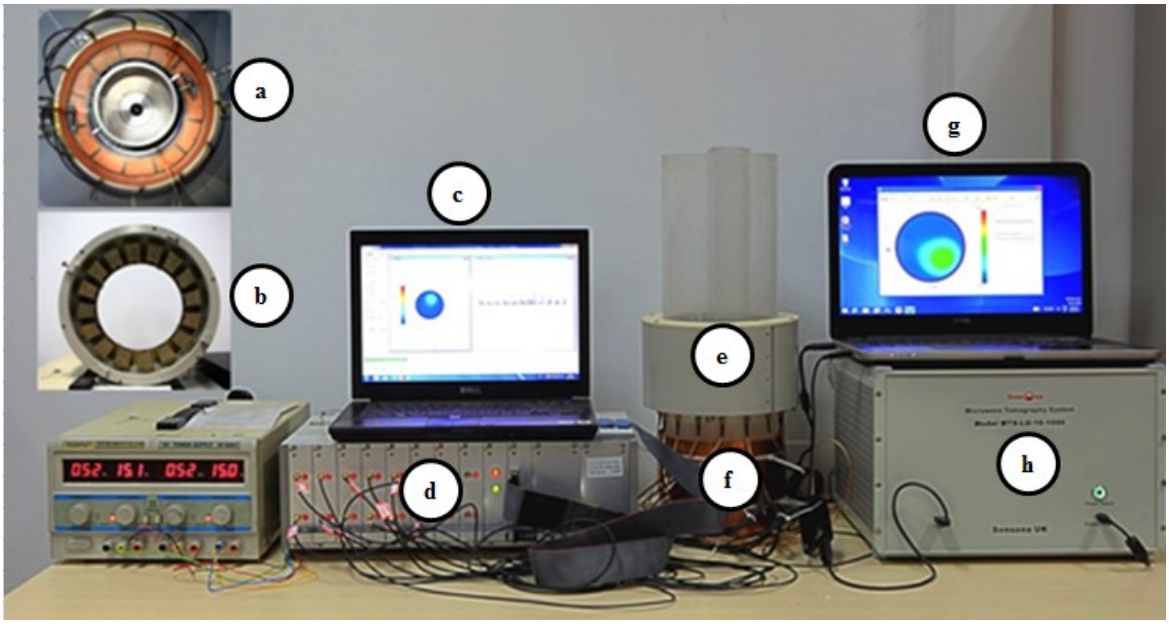

(a) Top view of ECT sensor
(b) Top view of MWT sensor
(c) Laptop for ECT image reconstruction
(d) AC-ECT for data acquisition system
(e) MWT sensor
(f) ECT sensor
(g) Laptop for MWT image reconstruction
(h) MWT data acquisition system

Figure 6.1: ECT and MWT system setup at the IET

6.3 Flow patterns and test materials

Four materials were used in the experiment: (1) air, (2) granules, (3) oil and (4) water. The permittivity and conductivity of each material are given in Table 6.1.

Table 6.1: Material characteristic

	Material	Permittivity (ε)	Conductivity (σ)
1.	Air	1	0
2.	Granules	6.4	0
3.	Oil	3.3	0
4.	Water	80	500-800 µS/cm

Before performing the measurements, the sensor was first calibrated with specific low and high permittivity materials e.g. imaging of granules and water was calibrated with granules and water as low and high permittivity respectively. The flow patterns used in the experiments are shown in Figure 6.2. The circular object is a hollow rod filled with the material other than the background of the imaging area.

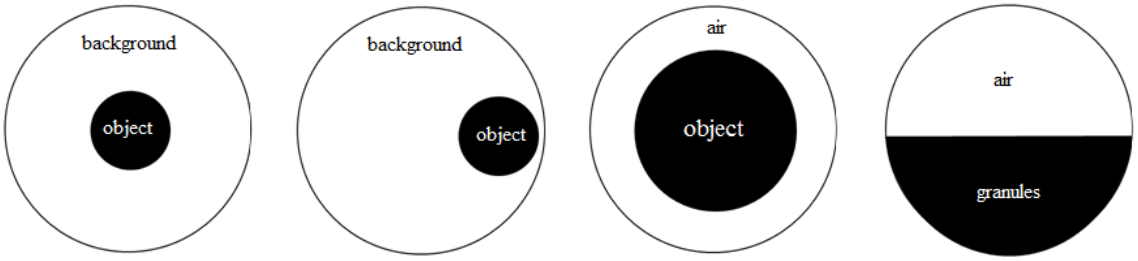

(a) Small object in the centre (b) Small object near the edge (c) Big object in the centre (d) Stratified

Figure 6.2: Flow patterns

6.4 Effect of flow patterns on image reconstruction

For the initial investigation, permittivity distribution (a) and (b) were selected to see the effect of flow patterns on image reconstruction. Air, granules, oil and water were used as a background medium for tests with other materials in the centre or near the edge of the pipe. For instance, when the air was used as the background, granules, oil and water were inserted into the pipe in the centre and near the edge. Images from ECT and MWT were then obtained and analysed. For this preliminary assessment, LBP algorithm was employed.

Figure 6.3 shows the images of the granules, oil and water placed in the centre, with air as the background. The result shows that ECT can give relatively high-quality images for granules and oil, but fails to produce the image for water. MWT, on the other hand, is able to produce images for all permittivity distributions.

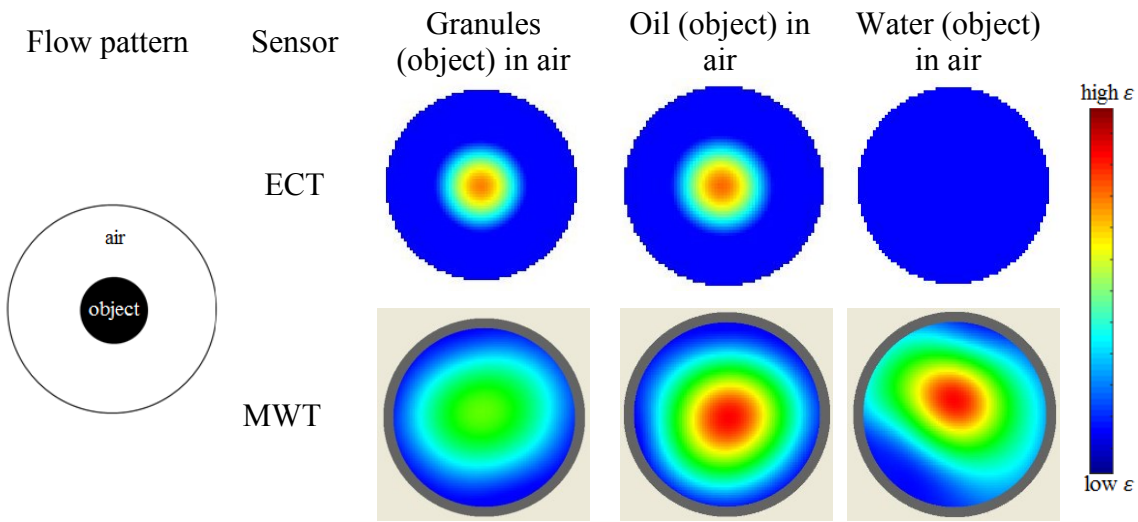

Figure 6.3: Images of object in centre with air as background

Figure 6.4 shows the reconstructed images of the same material placed near the edge. Both ECT and MWT can image permittivity distributions as the sensitivity on the edge of both sensors is strong. However, the images reconstructed by ECT have clearer boundaries.

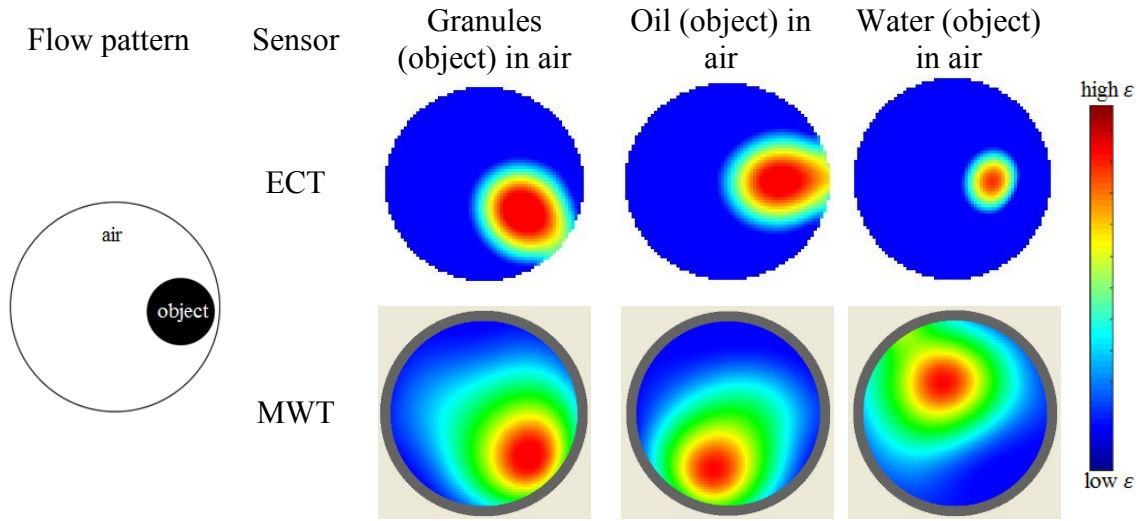

Figure 6.4: Images of object near edge with air as background

Figure 6.5 and Figure 6.6 show the reconstructed images when the sensor is filled with granules as background. With ECT, the image of oil in the centre and near the edge is good. There is a weak image of air but unacceptable image of water. Meanwhile, MWT at any condition fails to reconstruct reasonable images for the permittivity distribution, regardless of the object, material and location.

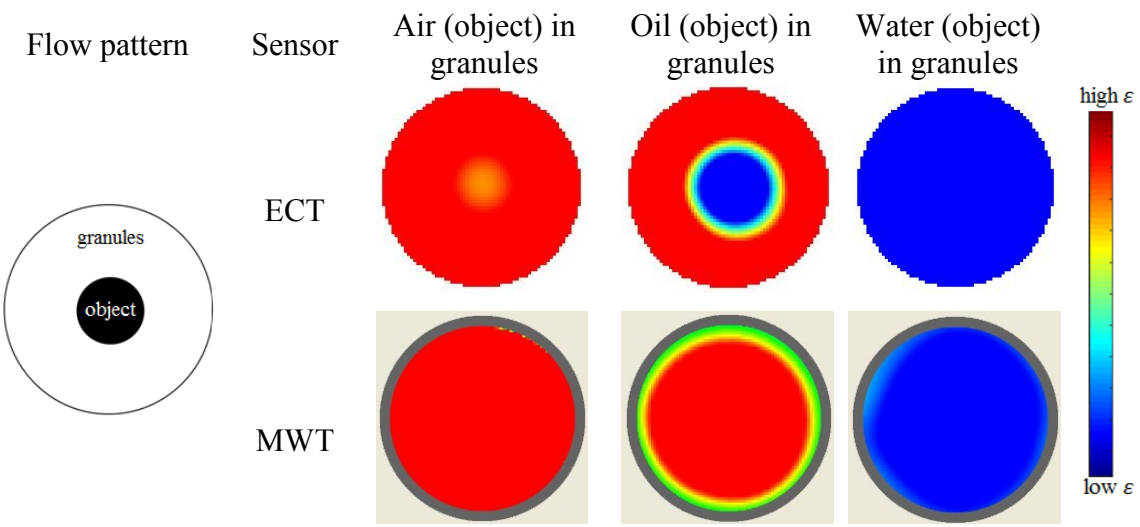

Figure 6.5: Images of object in centre with granules as background

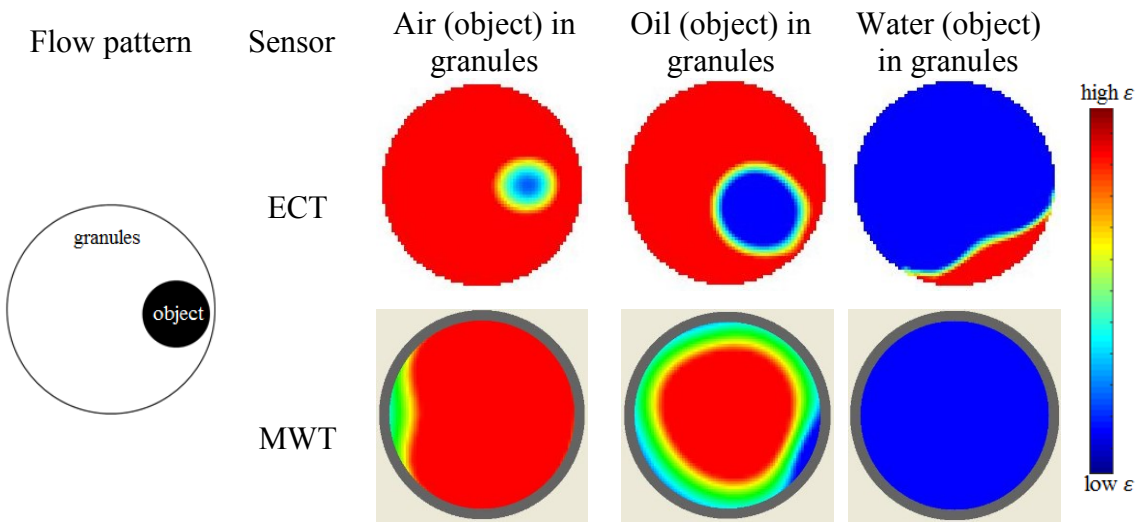

Figure 6.6: Images of object near edge with granules as background

The reconstructed images with oil as the background are shown in Figure 6.7 and Figure 6.8. Both ECT and MWT cannot generate a correct image of air in the centre. ECT has no problem in imaging every single object when it is placed near the edge of the sensor. MWT can image water at both locations although there is huge noise when the object is near the edge. A significant difference in object size is observed between the images reconstructed by ECT and MWT for granules in oil. MWT can detect different permittivity distributions of air near the edge, but the reconstructed image is strange, possibly due to measurement noise.

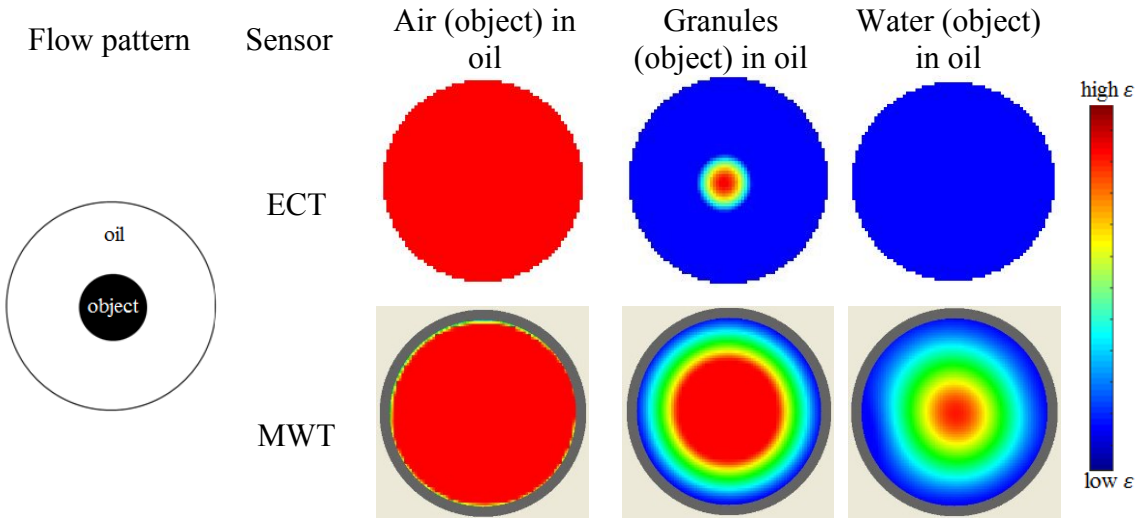

Figure 6.7: Images of object in centre with oil as background

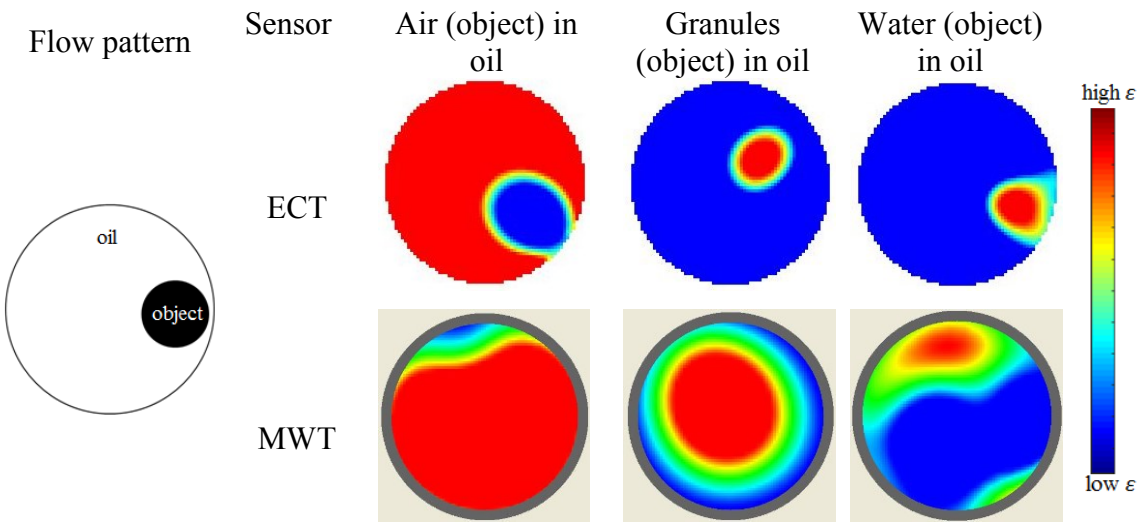

Figure 6.8: Images of object near edge with oil as background

The results of image reconstruction with a conductive background, i.e. water, are shown in Figure 6.9 and Figure 6.10. Regardless of the material and position of the objects, ECT is unable to image different permittivity distributions due to the large amount of water. MWT has the same results as the ECT for the object in the centre. MWT can image the permittivity distributions of all three materials that are air, granules and oil when they are placed near the edge where sensitivity is stronger.

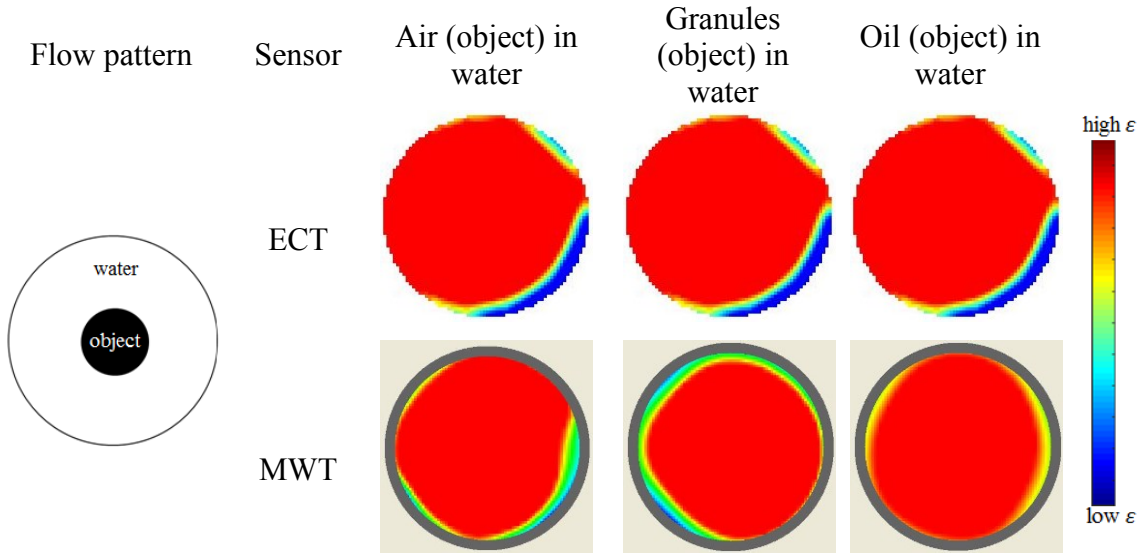

Figure 6.9: Images of object in centre with oil as background

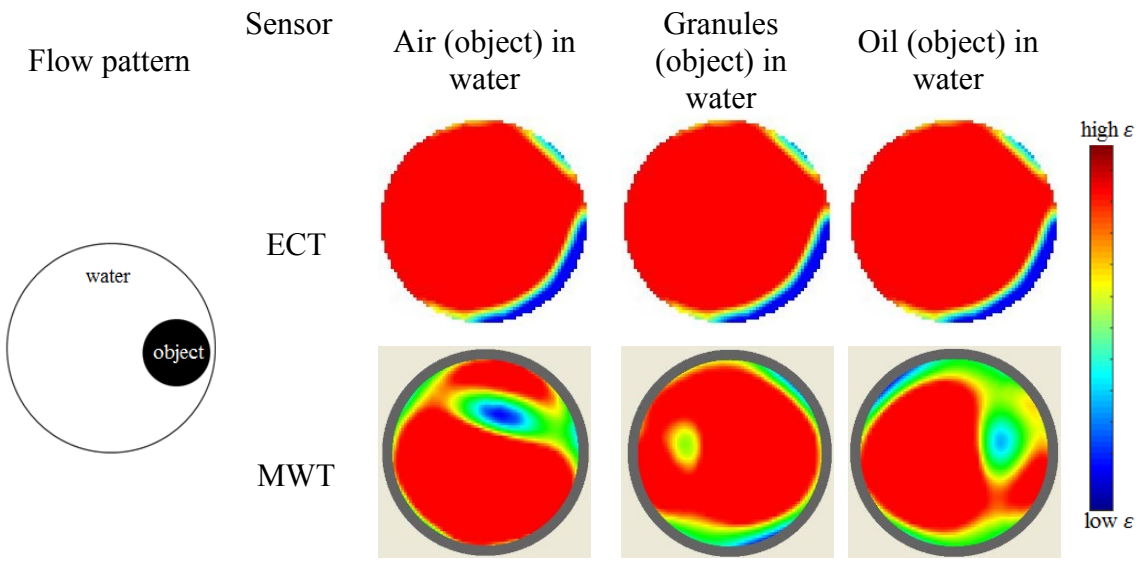

Figure 6.10: Images of object near edge with oil as background

Qualitative assessments of the image reconstruction are summarised in Table 6.2 and Table 6.3 for the object in the centre and near the edge, respectively. It can be concluded that the ECT and MWT have 50% similar capabilities and 50% complementing functions.

Table 6.2: Object in centre

Object	Air		Granules		Oil (non-conductive)		Water (conductive)	
Background	ECT	MWT	ECT	MWT	ECT	MWT	ECT	MWT
Air	NA	NA	✓	✓	✓	✓	**X**	✓
Granules	✓	**X**	NA	NA	✓	**X**	**X**	**X**
Oil (non-conductive)	**X**	**X**	✓	✓	NA	NA	**X**	✓
Water (conductive)	**X**	**X**	**X**	**X**	**X**	**X**	NA	NA

Table 6.3: Object near edge

Object	Air		Granules		Oil (non-conductive)		Water (conductive)	
Background	ECT	MWT	ECT	MWT	ECT	MWT	ECT	MWT
Air	NA	NA	✓	✓	✓	✓	✓	✓
Granules	✓	**X**	NA	NA	✓	**X**	**X**	**X**
Oil (non-conductive)	✓	**X**	✓	✓	NA	NA	✓	✓
Water (conductive)	**X**	✓	**X**	✓	**X**	✓	NA	NA

6.5 Effect of moisture on image reconstruction

To investigate the effects of moisture on image reconstruction, granules with different moisture contents, i.e. 10%, 15%, 20%, 25% and 30% were used. For this experiment, flow pattern (b), (c) and (d) were selected. For ECT, Landweber algorithm was adopted for a better quality of image reconstruction.

Figure 6.11 shows the image reconstruction results for ECT with flow pattern (b), (c) and (d) for granules with different moisture contents, ranging from 10% to 25%. As can be seen, ECT does not work well for granules with high moisture content (25%) for all of the three flows, especially for flow pattern (b) and (c). The image quality decreases with high moisture content because the capacitance gradually tends to be saturated and caused images to shrink and become blurry.

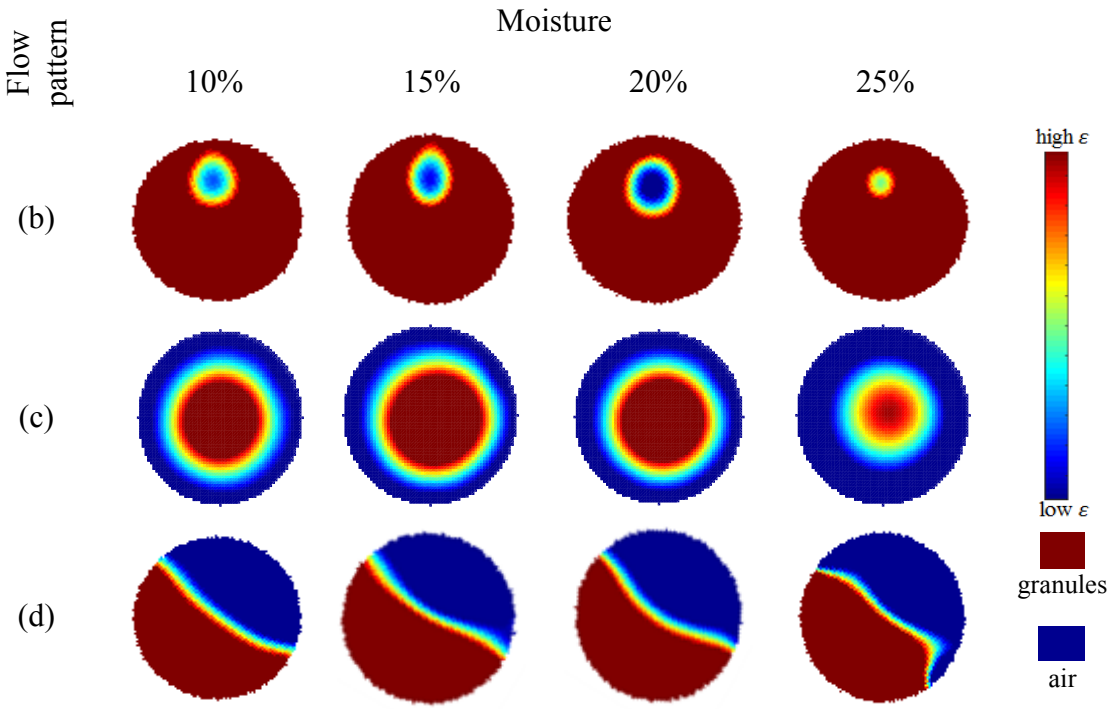

Figure 6.11: ECT image reconstructions with different moisture content

The reconstructed images by the MWT are shown in Figure 6.12. The total surface area for flow patterns (c) and (d) do not change significantly with the increase of moisture. The results indicate that moisture has little effects on microwave measurement. The effect of moisture on flow pattern (b) is more obvious where the measurement area tends to distort when the moisture content is bigger than 20%.

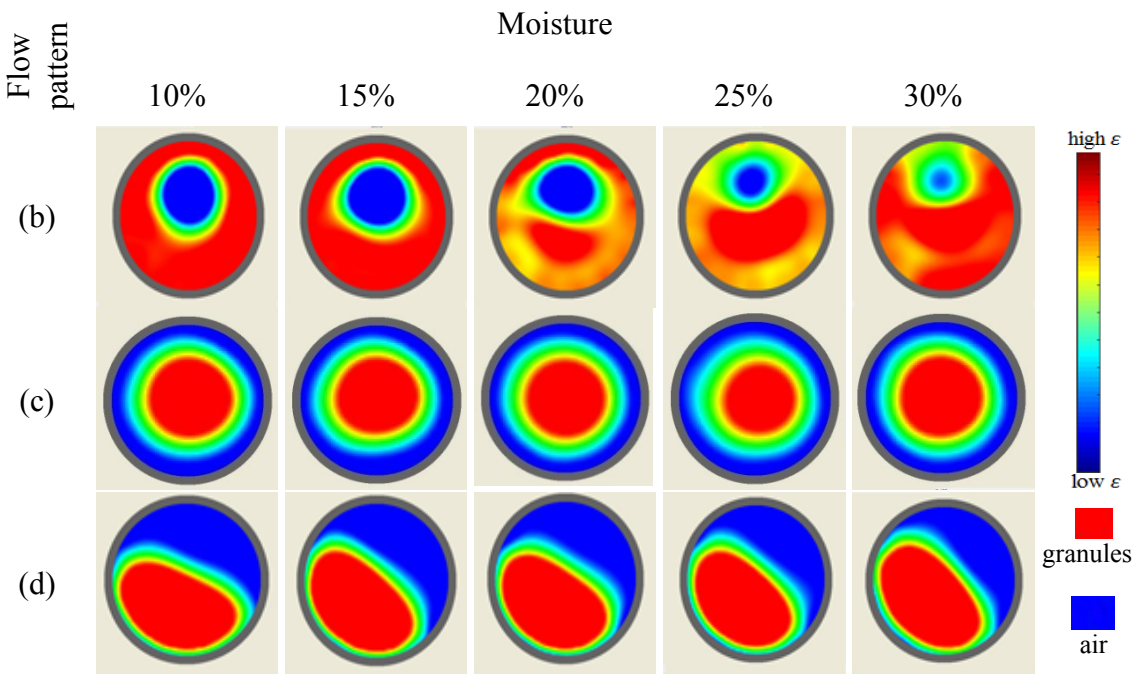

Figure 6.12: MWT image reconstructions with different moisture content

From the results shown in Figure 6.11 and Figure 6.12, it can be concluded that the moisture not only affects the ECT measurement but also affects the MWT measurement. However, the effect on MWT is weak compared to ECT.

The following experiments reconstruct different moisture granules with different moisture of high calibration moisture level for flow pattern (b). In Figure 6.13 and Figure 6.14, the red and blue indicates granules (high permittivity) and air (low permittivity background) respectively.

From the results in Figure 6.13, for a fixed moisture object (10%, 15%, 20% or 25%), the image quality is good when the high calibration moisture is 10%, 15% and 20%. However, the image quality significantly worsens when the moisture changes from 20% to 25%. The reconstructed images of the object with 30% moisture are not acceptable with any combinations. The results indicate that ECT only works in a limited range for wet granules that is up to 25% of the moisture content of the object with 20% moisture of high calibration. Figure 6.14 shows the images reconstructed with MWT. In contrast to the ECT, the reconstructed images are good when the moisture of object is high (at 30%).

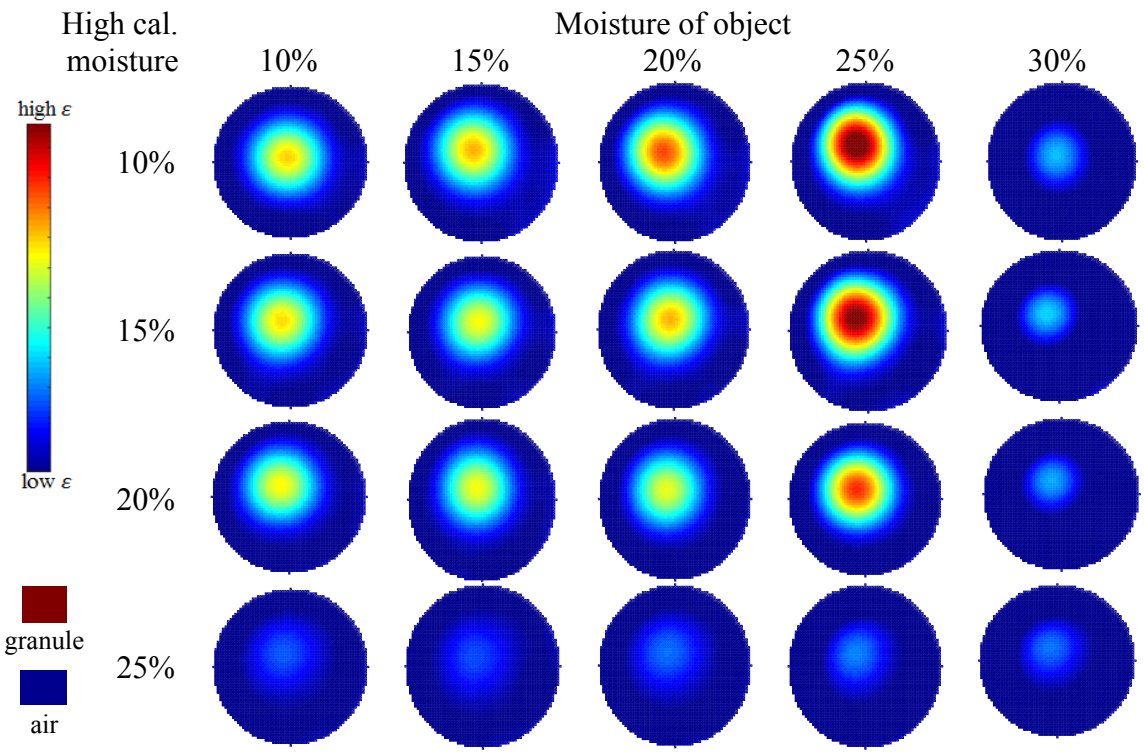

Figure 6.13: ECT image reconstructions for flow pattern (b)

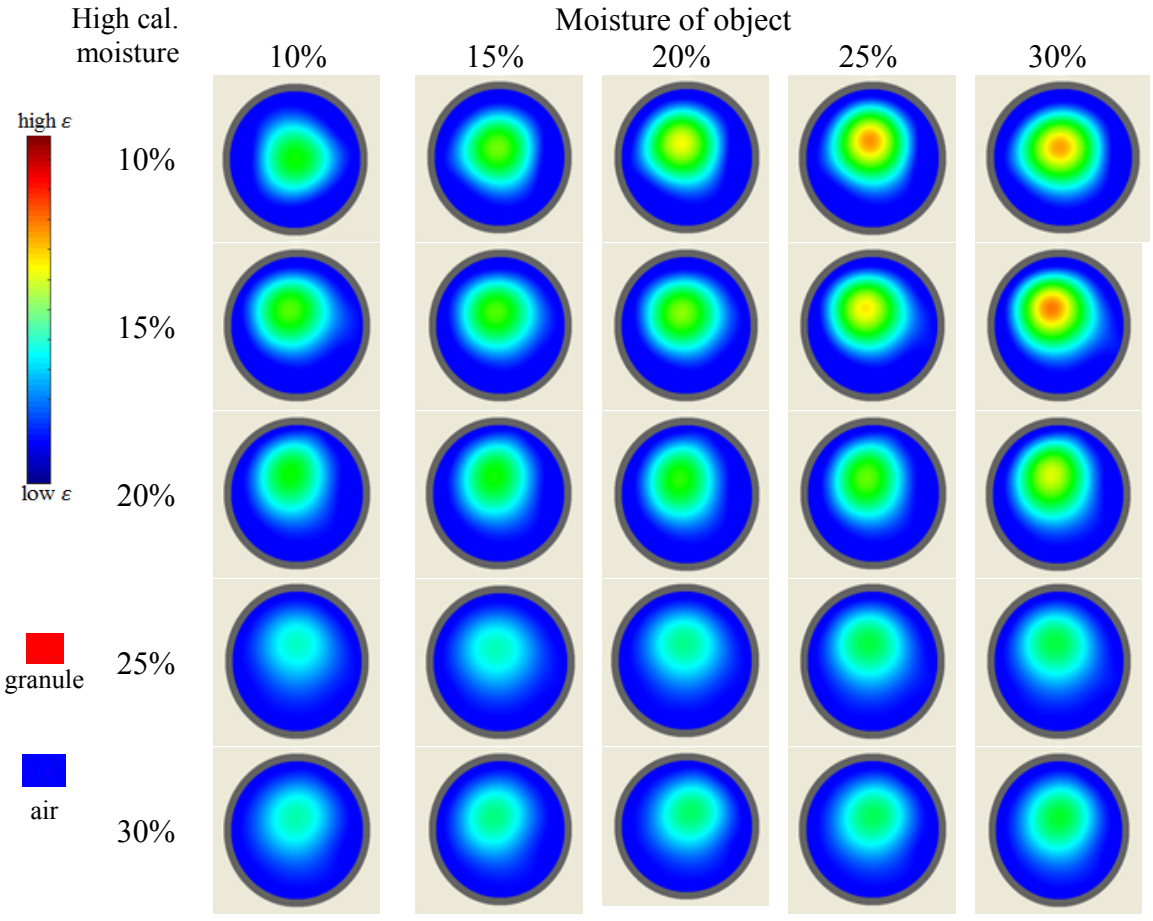

Figure 6.14: MWT image reconstructions for flow pattern (b)

6.5.1 Comparison of performance between ECT and MWT

Figure 6.15 shows the profiles of mean capacitance measured by ECT and signal strength measured by MWT. The graph shows that both of them increase with the increase in moisture.

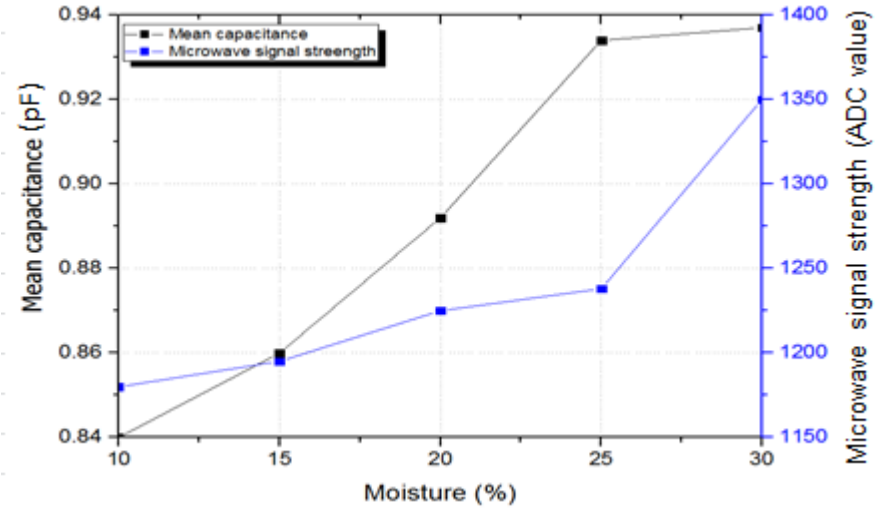

Figure 6.15: Mean capacitance and microwave signal strength with different moisture content of granules

Table 6.4 summarises the performance of ECT and MWT with different high calibration moisture and object moisture. With ECT, there is a sharp decline in the image quality when the granules moisture is higher than 25%. On the other hand, the effect of moisture on MWT is small.

Table 6.4: Comparison between ECT and MWT for wet granules

Moisture high reference	Moisture of object									
	10%		15%		20%		25%		30%	
	ECT	MWT	ECT	MWT	ECT	MWT	ECT	MWT	ECT	MWT
10%	✓	✓	✓	✓	✓	✓	✓	✓	**X**	✓
15%	✓	✓	✓	✓	✓	✓	✓	✓	**X**	✓
20%	✓	✓	✓	✓	✓	✓	✓	✓	**X**	✓
25%	**X**	✓	X	✓	**X**	✓	**X**	✓	**X**	✓
30%	**NA**	✓	**NA**	✓	**NA**	✓	**NA**	✓	**NA**	✓

Table 6.5 shows the comprehensive comparison of the two methods. As can be seen from this Table, ECT has high temporal resolution while MWT has a low temporal resolution. However, the effect of moisture on ECT is stronger than that of MWT. MWT can be used for high moisture content granules.

Table 6.5: Performance comparison between ECT and MWT

Sensor	Performance of ECT and MWT			
	The ability to measure material with low moisture	The ability to measure material with high moisture	Temporal resolution	Spatial resolution
ECT	✓	X	✓	X
MWT	✓	✓	X	✓

6.6 Summary

This Chapter presents the preliminary results for image reconstruction of permittivity distribution and wet granules with different moisture contents by ECT and MWT measurements. ECT and MWT sensors were mounted on the same tube, top and bottom, to measure similar flow pattern. The measurement was taken simultaneously but separately for both systems. Four materials (i.e. air, granules, oil and water) were used to reconstruct images of an object in the centre and near the edge.

The performance of ECT and MWT in detecting the different permittivity distributions are compared, and results indicate that ECT and MWT have 50% of similar capabilities and 50% of complementing their functions. For high moisture content granules, MWT is able to give good image reconstruction results compared to ECT, especially when the moisture content of the object is larger than 25%. Therefore, it is recommended to use ECT to image non-conductive, low moisture content materials and MWT for higher permittivity, higher water content and moderate conductivity materials.

This is the first time that these two tomography techniques have been used together and applied to image the complex solid distribution. This system is useful, in particular, as a process control of fluidised bed drying, granulation and coating process. The preliminary results are promising and show the feasibility of the system to be implemented in real field applications. However, improvements such as upgrading the temporal resolution of MWT to catch up with the speed of a gas-solids flow need to be made. In the future, it is recommended that the work is extended to be used on the dynamic flow that resembles the real process of production with a fluidised bed.

Chapter 7: Conclusions and future work

7.1 Conclusions

The results of this research show that the implementation of the dual-modality ECT and microwave sensor is feasible and advantageous. The initial development of these dual-modality systems presents several improvements over the current traditional systems.

Dual-modality of ECT and MRS

The use of a dual-modality system with ECT and MRS helps provide more information on the multiphase flow within a full-phase flow (from oil-continuous to water-continuous). Capacitance measurement from the 8-electrode sensor was successfully used in identifying the flow regime of the three-phase flow. The compliance in detecting the stratified or annular flow of the emulsion was 100% through the adaptation of the *'fingerprint'* method and the Euclidean function. The identification of flow regimes based on the data obtained from the MRS, however, is not feasible.

The estimation of WLR is difficult with ECT in the water-continuous flow; therefore, combining the function with MRS is a good option. Based on the capacitance data, the phase transition can be predicted at WLR 50% since the relationship between capacitance and WLR from this point, is no longer linear. The prediction was then confirmed by the transmission coefficient amplitude obtained by the MRS, where an obvious drop could be seen with high water content due to the effect of the higher permittivity of water. This information was used to determine a threshold value or a transition point to switch the system from ECT to MRS. In the water-continuous flow, the resonant frequency was used for WLR estimation.

The new dual modality of ECT and MRS were tested over 18 conditions, from both stratified and annular flow. Overall, the estimation of WLR was reasonable with 67% of the conditions giving error less than 5%. Five conditions gave WLR error between 5% and 10% and only one condition showed a slightly more than 10% error. This was mainly due to the measurement error that might have been caused by the inaccurate manual mixing of the emulsion that affected the stability and behaviour of the flow. The comparison of WLR between the stratified and annular flows revealed an insignificant

difference; therefore, it can be concluded that this system minimises the dependency of the flow regime.

This ECT-MRS dual-modality system uses raw capacitance and resonant frequency as measured by the devices. Therefore, it does not require a complicated calibration. It took approximately 0.14 seconds to process the data for one cycle, and this is considered as fast in comparison to a normal tomographic technique which usually takes around 6 seconds. Unlike other dual-modality systems such as the ECT-ERT, another huge advantage of the system is that it is totally non-invasive and non-intrusive.

Sensitivity map analysis

Three types of sensitivity maps with empty, powder and water background were generated using the dot-product multiplication method. Their effects on the quality of reconstructed images based on image error were then evaluated. The results show that a generic sensitivity map with the empty background is appropriate to reconstruct images for most defined permittivity flow regimes. However, for annular flow with a thin layer, especially for water, the updated sensitivity map (according to the material) should be used. These results are helpful as no study has been conducted to analyse these situations and provide options for sensitivity maps to match with specific applications, rather than only one generic sensitivity map for all cases.

Dual-modality of ECT and MWT

A 12-electrode ECT was developed and combined with the MWT to investigate the effects of 2-phase flow patterns on image reconstruction. Images reconstructed with ECT used generic sensitivity maps as recommended in the above-mentioned sensitivity map analysis. The air, granules, oil and water were used as the objects and background alternately. The experiments were then extended to investigate the solid concentration with different moisture contents. The measurement results show that both ECT and MWT functions as moisture contents and flow patterns. Their measurements in detecting the flow pattern are complementary to each other by 50%. In imaging solid concentration, ECT and MWT are recommended to be used in lower and higher water content, respectively. The information gathered is useful to be used as a process to control fluidised bed drying, granulation and coating to improve operational efficiency.

7.2 Future work

Dual-modality of ECT and MRS

1. The overall uncertainty of WLR estimation needs to be improved. To do this, a model-based algorithm can be considered.
2. To simplify the calculation, this research proposed a fixed 50% of WLR as the threshold value or transition point from oil-continuous to water-continuous flows. However, in reality, it could be anywhere in between. Thus, a study is needed to define a more accurate definition to avoid misinterpretation and wrong selection of equation for WLR estimation.
3. The next target is to study the effect of conductivity on the performance of the dual-modality system. This can be done by measuring emulsion that produced from oil emulsified with higher conductive water.
4. Future work should be extended to measure the total liquid fraction. More experiments need to be carried out with different fractions for the characterization of the sensors.
5. A centralised system needs to be developed to control the dual-modality of ECT and MWT. In this way, the system is possible to process the data from both devices in almost real time.

Sensitivity map analysis

6. For a more thorough investigation, sensitivity maps should be generated with another method i.e. the perturbation method as a comparison to the results in Chapter 5.
7. Other than generating sensitivity maps with a single material, sensitivity maps can also be generated according to the expected flow regimes and the materials. For example, sensitivity maps can be obtained from a stratified distribution to image stratified flow.

Dual-modality of ECT and MRS

8. The parameters setting can be further optimised to improve imaging results.
9. The temporal resolution of the MWT needs to be improved to cope with the fast gas-solid flows. This probably can be achieved by upgrading to a high-speed PC cluster and graphic processing unit (GPU) cards.

10. Future work should focus on the dynamic test instead of a static flow measurement.
11. Since the structure of the fluidised bed is not limited to a cylindrical shape, different geometric sensors in a shape of a conical sensor, for example, should be considered.

References

[1] Agilent Technologies (2000), 4192A LF Impedance Analyser and Service Manual

[2] Aitmehdi R, Anderson A and Sali S (1988), The determination of dielectric loss tangent by microwave phase tomography, *Inverse Problem*, 4(2), pp. 333-345

[3] Akyel C, Labelle R C, Berteaud A J and Bosisio R G (1985), Computer-Aided Permittivity Measurements of Moistened and Pyrolized Materials in Strong RF Fields, *IEEE Trans. on Instrumentation and Measurement*, 34(1), pp. 25–31

[4] Al-Hajeri S, Wylie S R, Stuart R A and Al-Shamma'a A I (2007), An electromagnetic cavity sensor for multiphase measurement in the oil and gas industry, *Journal of Physics*, 76(1), p.012007

[5] Araneta J C, Brodwin, M E and Kriegsmann, G A (1984), High-Temperature Microwave Characterization of Dielectric Rods, *IEEE Trans. on Microwave Theory and Techniques*, 32(10), pp. 1328–1335

[6] Avila H E L, Pagano D J, Sousa F R (2013), Water Fraction Measurement Using an RF Resonant Cavity Sensor, *in 19th Symposium IMEKO TC 4 Symposium and 17th IWADC Workshop*, 18-19 July, Barcelona, Spain, pp. 281–285

[7] Banasiak R and Soleimani M (2010), Shape based reconstruction of experimental data in 3D electrical capacitance tomography, *NDT and E International*, 43(3), pp. 241–249

[8] Baumann S B, Joines, W T and Berman E (1987), Feasibility Study of Batteryless Temperature Transponder Using Miniature Microwave Cavity Resonators, *IEEE Trans. on Biomedical Engineering*, 34(9), pp. 754–757

[9] Bolomey J C, Izadnegahdar A, Jofre L, Pichot CH, Peronnet G and Solaimani M (1982), Microwave Diffraction Tomography for Biomedical Applications, *IEEE Trans. on Microwave Theory and Techniques*, 30(11), pp. 1998–2000

[10] Bolomey J C (1989), Recent European Developments in Active Microwave Imaging for Industrial, Scientific, and Medical Applications, *IEEE Trans. on Microwave Theory and Techniques*, 37(12), pp. 2109–2117

[11] Broquetas A, Ferrando M, Rius J, Jofre L, de los Reyes E, Cardama A, Elias A and Ibáñez J (1987), Temperature and permittivity measurements using a cylindrical microwave imaging system, *European Microwave Conference*, 7-11 Sept., Rome, Italy, pp. 892–895

[12] Chommeloux L, Pichot C and Bolomey J C (1986), Electromagnetic Modeling for Microwave Imaging of Cylindrical Buried Inhomogeneities, *IEEE Trans. on Microwave Theory and Techniques*, 34(10), pp. 1064–1076

[13] Chrondronasios A (2003), High sensitivity electrical capacitance tomography system and its application, PhD thesis, UMIST, UK

[14] Doughty D A (1977), Determination of Water in Oil Emulsions by a Microwave Resonance Procedure, *Analytical Chemistry*, 49(6), pp. 690–694

[15] Dourthe C, Pichot C, Dauvigna J Y and Cariou J (2000), Inversion algorithm and measurement system for microwave tomography of buried object, *Radio Science*, 35(5), pp. 1097–1108

[16] Eisenstadt W R and Eo Y (1992), S-parameter-based IC interconnect transmission line characterization, *IEEE Trans. on Components, Hybrids, and Manufacturing Technology*, 15(4), pp. 483–490

[17] Falcone G, Hewitt G F and Alimonti C (2010), *Multiphase Flow Metering Principles and Applications*, Elsevier

[18] Fang W (2004), A nonlinear image reconstruction algorithm for electrical capacitance tomography, *Meas. Sc. Technol*., 15, pp. 2124–2132

[19] Franchois A and Pichot C (1997), Microwave Imaging-Complex Permittivity Reconstruction with a Levenberg-Marquardt Method, *IEEE Trans. on Antennas and Propagation*, 45(2), pp. 203–215

[20] Frias M A R (2015), Electrical Capacitance And Resistance Tomography With Voltage Excitation, MPhil thesis, The University of Manchester, UK

[21] Gennarelli G, Romeo S, Scarfi M R and Soldovieri F (2013), A microwave resonant sensor for concentration measurements of liquid solutions, *IEEE Sensors Journal*, 13(5), pp. 1857–1864

[22] Glatt Process Technology Pharma (April 2014), Fluidised Bed System

[23] Hansen, P C (1997), Rank-Deficient and Discrete Ill-Posed Problems (Philadelphia, PA: SIAM)

[24] Hoppe W, Meyer W and Schilz W (1980), Density Independent Moisture Metering In Fibrous Materials Using A Double Cut-off Gunn Oscillator, *International Microwave Symposium Digest*, pp. 419–421

[25] Hu X, Yang M, Li Y, Yang W Q, Lara M M (2008), An impedance-analyser-based multi-channel imaging system and it's applications, *IEEE International*

Workshop Imaging Systems and Techniques (IST), 10-12 September, Chania, Greece, pp. 181-186

[26] Huang S, Green R G, Plaskowski A and Beck M S (1988), A high frequency stray-immune capacitance transducer based on the charge transfer principle, *IEEE Trans. on Instrumentation and Measurement*, 37(3), pp. 368–373

[27] Huang S M, Xie C G, Thorn R, Snowden D and Beck M S (1992), Design of sensor electronics for electrical capacitance tomography, *IEE Proc., Part G: Circuits, Devices and Systems*, 139(1), pp. 83-88

[28] Huang S M, Plaskowski A B, Xie C G and Beck M S (1989), Tomographic imaging of two-component flow using capacitance sensor, *Journal of Physics E: Scientific Instruments*, 22(3), pp. 173–177

[29] Irishina N, Dorn O and Moscoso M (2008), A level set evolution strategy in microwave imaging for early breast cancer detection, *Computers & Mathematics with Applications*, 56(3), pp. 607–618

[30] Isaksen O, Dico A S and Hammer E A (1994), A capacitance-based tomography system for interface measurement in separation vessels, *Meas. Sci. Technol.*, 5(10), pp. 1262-1271

[31] Isaksen O and Nordtvedt J E (1993), A new reconstruction algorithm for process tomograph, *Meas. Sci. Technol.*, 4(12) , pp. 1464-1475

[32] Ishii T K (1989), Microwave Engineering Second Edi., Harcourt Brace Jovanovich, USA

[33] Jang J D, Lee S H, Kim K Y and Choi B Y (2006), Modified iterative Landweber method in electrical capacitance tomography, *Meas. Sci. Technol.*, 17(7), pp. 1909–1917.

[34] Jaworski A J and Bolton G T (2000), The design of an electrical capacitance tomography sensor for use with media of high dielectric permittivity, *Meas. Sc. Technol*., 743(6), pp. 743–757

[35] Jow J, Hawley M C, Finzel M, Asmussen J, Lin H H, Maring B (1987), Microwave Processing and Diagnosis of Chemically Reacting Materials in a Single-Mode Cavity Applicator, *IEEE Trans. On Microwave Theory and Techniques*, 35(12), pp. 1435–1443.

[36] Kim Y S, Lee S H, Ijaz U Z, Kim K Y and Choi B Y (2007), Sensitivity map generation in electrical capacitance tomography using mixed normalization models, *Meas. Sci. Technol.*, 18(7), pp. 2092–2102.

[37] Konopka, J and Majewski J J (1980), A New Microwave Method for Testing Nonlinear Effects in Solids, *10th European Microwave Conference*, Sept, pp. 246–250.

[38] Kurokawa K (1965), Power Waves and the Scattering Matrix, *IEEE Trans. on Microwave Theory and Techniques*, 13(2), pp. 194–202

[39] Lakshminarayana M R, Partain L D and Cook W A (1979), Simple microwave technique for independent measurement of sample size and dielectric constant with results for a gunn oscillator system, *IEEE Trans. on Microwave Theory and Techniques*, 27(7), pp. 661–665

[40] Landweber L (1951), An Iteration Formula for Fredholm Integral Equations of the First Kind*, American Journal of Mathematics*, 73(3), pp. 615–624

[41] Larsen L E and Jacobi J H (1979), Microwave scattering parameter imagery of an isolated canine kidney, *Medical Physics*, 6(5), pp. 394–403

[42] Li Y, Yang W Q, Xie C G, Huang S, Wu Z, Tsamakis D and Lenn C (2013), Gas/oil/water flow measurement by electrical capacitance tomography, *Meas. Sci. Technol.*, 24(7), p. 74001

[43] Li Y (2008), Key issues of 2D / 3D image reconstruction in electrical tomography, PhD thesis, University of Manchester, UK

[44] Li Y and Yang W Q (2008), Image reconstruction by nonlinear Landweber iteration for complicated distributions, *Meas. Sc. Technol*., 19(9), pp. 94014

[45] Li Y and Yang W Q (2007), Updating Sensitivity Maps in Landweber Iteration for Electrical Capacitance Tomography, *in Proc. of 5th World Congress on Industrial Process Tomography*, 3-6 Sept, Bergen, Norway, pp. 1116–1123.

[46] Liu S, Chen Q, Wang H G, Jiang F, Ismail I, Yang W Q (2005), Electrical capacitance tomography for gas–solids flow measurement for circulating fluidized beds, *Flow Measurement and Instrumentation*, 16(2–3), pp. 135–144.

[47] Liu S, Fu L and Yang W Q (1999), Optimization of an iterative image reconstruction algorithm for electrical capacitance tomography, *Meas. Sc. Technol.,* 10(7), pp. L37-L39

[48] Liu S, Yang W Q and Wang H G (2001), An electrical capacitance tomography sensor with internal-external electrodes, *Proc. SPIE 4188, Process Imaging for Automatic Control*, pp. 300–307

[49] Meaney P M, Paulsen K D, Hartov A and Crane R K (1996), Microwave imaging for tissue assessment: Initial evaluation in multitarget tissue-equivalent phantoms, *IEEE Trans. on Biomedical Engineering*, 43(9), pp. 878–888

[50] Merlo A L (1970), Combustion Chamber Investigation by Mean of Microwave Resonances, *IEEE Trans. on Industrial Electronics and Control Instrumentation*, 17(2), pp. 60–66

[51] Naelapa K, Veski P, Pedersen J G, Anov D, Jorgensen P, Kristensen H G and Bertensen P (2007), Acoustic monitoring of a fluidized bed coating process, *Int. J Pharm.*, 332(1), pp. 90-97

[52] Nohlert J, Rylander T and McKelvey T (2015), Microwave resonator sensor for detection of dielectric objects in metal pipes, *IEEE Instrumentation and Measurement Technology Conference*, 2015–July, pp. 914–919

[53] Nugroho A T and Wu Z (2015), Inexact Newton Backtracking Method for Solving Microwave Tomography Inverse Problem, *in IEEE International Conference on Imaging Systems and Techniques (IST)*, Macau, 16-18 Sept, pp. 1-6

[54] Nyfors E G (2000), Industrial Microwave Sensors---A Review, *Subsurface Sensing Technologies and Applications*, 1(1), pp. 23–43

[55] Nyfors E G (2000), Cylindrical Microwave Resonator Sensors For Measuring Material Under Flow, Doctor of Science in Technology thesis, Helsinki University of Technology

[56] Nyfors E and Vainikainen P (1989), Industrial Microwave Sensors, Artech House, Inc, Norwood, MA

[57] Olver A and Cuthbert L (1988), FMCW radar for hidden object detection, *in IEE Proc. F: Communications, Radar and Signal Processing*, pp. 354–361.

[58] Peiro J and Sherwin S (2005), Finite Difference, Finite Element and Finite Volume Methods for Partial Differential, *in Handbook of Materials Modeling*, Springer, pp. 1–32

[59] Peng L, Ye J, Lu G and Yang W Q (2012), Evaluation of Effect of Number of Electrodes in ECT Sensors on Image Quality, *IEEE Sensors Journal*, 12(5), pp. 1554–1565.

[60] Peng L, Merkus H and Scarlett B (2000), Using Regularization Methods for Image Reconstruction of Electrical Capacitance Tomography, *Particle & Particle Systems Characterization*, 17(3), pp. 96–104

[61] Peronnet G, Pichot Ch, Bolomey J C, Jofre L, Izadnegahdar A, Szeles C, Michel Y, Guerguin-Kern J L and Gautherie M (1983), A Microwave Diffraction Tomography System for Biomedical, *in 13th European Microwave Conference*, 3-8 Sept, Messezentrum, Nrnberg, West Germany, pp. 529–533

[62] Pichot C, Jofre L, Peronnet G, Bolomey J (1985), Active microwave imaging of inhomogeneous bodies, *IEEE Trans. Antennas and Propagation*, 33(4), pp. 416–425.

[63] Polydorides N (2002), Image reconstruction algorithms for soft-field tomography, PhD thesis, University of Manchester, UK

[64] Pozar D M (1998), Microwave Engineering Second Edi., John Wiley & Sons, Inc., USA

[65] Pradeep C (2015), Tomographic Approach to Automatic and Non-Invasive Flow Regime Identification, PhD thesis, Telemark University College, Norway

[66] Process Tomography Ltd (2001), Engineering Design Rules For ECT Sensor, Issue 4, Wilmslow, UK

[67] Ren S, Dong F, Xu Y and Tan C (2014), Reconstruction of the three-dimensional inclusion shapes using electrical capacitance tomography, *Meas. Sci. Technol.*, 25(2), p. 25403 (16pp)

[68] Ren Z (2015), Exploration of medical applications of electrical capacitance tomography, PhD thesis, University of Manchester, UK

[69] Ren Z and Yang W Q (2012), An electrical capacitance tomography system with MatLab-Simulink GUI, *in IEEE International Conference on Imaging Systems and Techniques (IST)*, 16-17 July, Manchester, UK, pp. 578–583

[70] Rius J M, Pichot C, Jofre L, Bolomey J C, Joachimowicz N, Broquetas A and Feraando M (1992), Planar and Cylindrical Active Microwave Temperature Imaging: Numerical Simulations, *IEEE Trans. on Medical Imaging*, 11(4), pp. 457–469.

[71] Sensona Ltd. UK (2013), Microwave Tomography System Model LU-16-1000 User Manual List of Contents, (December), pp 1–29

[72] Soleimani M and Lionheart W R B (2005), Nonlinear image reconstruction for electrical capacitance tomography using experimental data, *Meas. Sci. Technol.*, 16(10), pp. 1987–1996

[73] Society of Petroleum Engineers (SPE), http://petrowiki.org/Oil_emulsions, as seen on 27 March 2017

[74] Sun J and Yang W Q (2014), Evaluation of fringe effect of electrical resistance tomography sensor, *Measurement* , 53, pp. 145–160

[75] Test Equipment Plus (2010), Signal Hound USB-SA44B User Manual

[76] Thamae L Z and Wu Z P (2010), Broadband Bowtie Dielectric Resonator Antenna, *IEEE Trans. on Antenna and Propagation*, 58(11), pp. 3707-3710

[77] Tian W, Sun J, Ramli M F and Yang W Q (2016), An Electrical Capacitance Tomography Sensor with Variable Diameter, *IEEE Sensors Journal*, 17(7), pp. 2089-2099

[78] Tikhonov A N and Arsenin V Y (1978), Reviewed Work: Solutions of Ill-posed Problems, Mathematics of Computation, 3(3), pp. 301-319

[79] Thorn R, Johansen G A and Hjertaker B T (2013), Three-phase flow measurement in petroleum industry, *Meas. Sci. Technol.*, 24(1), p. 012003 (17pp)

[80] Toropainen A, Vainikainen P and Nyfors E (1987), Microwave Humidity Sensor for Difficult Environmental Conditions, *17th European Microwave Conference*, 7-11 Sept, pp. 887–891

[81] TUV NEL (2003), National Measurement System Three-Year Programme for Flow 1999-2002 Programme Review Report

[82] Twister, http://twisterbv.com/, as seen on 27 Mar 2017

[83] Walker G M, Bell S E J, Greene K, Jones D S and Andrews G P (2009), Characterisation of fluidised bed granulation processes using in-situ Raman spectroscopy, *Chemical Engineering Science*, 64(1), pp. 91-98

[84] Wang H, Tang L and Cao Z (2007), An image reconstruction algorithm based on total variation with adaptive mesh refinement for ECT, *Flow Measurement and Instrumentation*, 18 (5–6), pp. 262–267

[85] Wang H G. Zhang J L, Ramli M F, Mao M X, Ye J M, Yang W Q and Wu Z P (2016), Imaging wet granules with different flow patterns by electrical capacitance tomography and microwave tomography, *Meas. Sci. Technol.*, 27(11), p. 114007 (12 pp)

[86] Wang H G, Yang W Q, Senior P, Raghavan R S and Duncan S R (2008), Investigation of batch fluidized-bed drying by mathematical modeling, CFD simulation and ECT measurement, *AIChE Journal*, 54(2), pp. 427–444

[87] Wang H G, Senior P R and Yang W Q (2009), Online measurement and control of solids moisture in fluidised bed dryers, *Chemical Engineering Science*, 64(12), pp. 2893–2902

[88] Wang H G and Yang W Q (2010), Measurement of fluidised bed dryer by different frequency and different normalisation methods with electrical capacitance tomography, *Powder Technology*, 199(1), pp. 60–69

[89] Waterfall R C, Hes R. and Beck M (1997), Visualizing combustion using electrical impedance tomography, *Chemical Engineering Science*, 52(13) pp. 2129-2138

[90] Wu Z, McCann H, Davis L E, Hu J, Fontes A and Xie C G (2009), Microwave-tomographic system for oil- and gas-multiphase-flow imaging, *Meas. Sci. Technol.*, 20(10), p.104026 (8pp)

[91] Wylie S R, Shaw A and Al-Shamma'a A I (2006), RF sensor for multiphase flow measurement through an oil pipeline, *Meas. Sci. Technol.*, 17(8), pp. 2141–2149

[92] Xie C G, Huang S M, Hoyle B S, Thorn R, Lenn C, Snowden D and Beck M S (1992), Electrical capacitance tomography for flow imaging: system model for development of image reconstruction algorithms and design of primary sensors, *IEE Proc. G Circuits, Devices and Systems*, 139(1), pp. 89-98

[93] Xie C G (2007), Measurement of multiphase flow water fraction and water-cut., *AIP Conference Proc.*, 914, pp. 232–239

[94] Xie C G, Beck M S and Plaskowski A (1989), 8-electrode capacitance system for two-component flow identification, *IEE Proc.*, 136, pp. 173-183

[95] Xu, M, Thulasiraman P and Noghanian S (2012), Microwave tomography for breast cancer detection on Cell broadband engine processors, *Journal of Parallel and Distributed Computing*, 72(9), pp. 1106–1116

[96] Yan H, Shao F Q, Xu H and Wang S (1999), Three-dimensional analysis of electrical capacitance tomography sensing fields, *Meas. Sci. Technol.*, 10(8), pp. 717-725

[97] Yang M (2007), Electrical Tomography: Impedance-analyser-based Electrical Tomography System User's Manual, Version 1.0a, The University of Manchester

[98] Yang W Q (2010), Design of electrical capacitance tomography sensors, *Meas. Sci. Technol.*, 21(4), pp. 42001

[99] Yang W Q, Nguyen T, Betting M, Chondronasios A, Nattrass S, Okimoto F and McCann H (2002), Imaging wet gas separation process by capacitance tomography, *SPIE- The international Society for Optical Engineering*, 4665, pp. 347-358

[100] Yang W Q and Peng L (2003), Image reconstruction algorithms for electrical capacitance tomography, *Meas. Sc. Technol*., 14(1), pp. R1-R13

[101] Yang W Q, Chondronasios A, Nattrass S, Nguyen V T, Betting M, Ismail I and McCann H (2004), Adaptive calibration of a capacitance tomography system for imaging water droplet distribution, *Flow Measurement and Instrumentation*, 15(5–6), pp. 249–258

[102] Yang W Q, Spink D M, York T A and McCann H (1999), An image-reconstruction algorithm based on Landweber's iteration method for electrical-capacitance tomography, *Meas. Sci. Technol.*, 10(11), pp. 1065–1069

[103] Yang W Q, Scott A L, Beck M S and Xie C G (1995), Development of capacitance tomographic imaging systems for oil pipeline measurements, *Review of Scientific Instruments*, 66(8), pp. 4326–4332

[104] Yang W Q (1996), Hardware design of electrical capacitance tomography systems, *Meas. Sci. Technol.*, 7(3), pp. 225-232

[105] Yang W Q (1997), Modelling of capacitance tomography sensors, IEE *Proc.*-Science, Measurement and. Technology., 144(5), pp. 203–208

[106] Yang W Q and Conway W F (1998), Measurement of sensitivity distributions of capacitance tomography sensors, *Review of Scientific Instruments*, 69(1), pp. 233-236

[107] Yang W Q and Liu S (1999), Electrical Capacitance Tomography with a Square Sensor, *Electronic Letters*, 35(4), pp. 295-296

[108] Yang W Q and Liu S (2000), Role of tomography in gas/solids flow measurement, *Flow Measurement and Instrumentation*, 11(3), pp. 237–244

[109] Yang W Q, Li Y, Wu Z P, Tsamakis D, Xie C G, Huang S and Lenn C (2011), Multiphase Flow Measurement by Electrical Capacitance Tomography, *in IEEE International Conference on Imaging Systems and Techniques*, 17-18 May 2011, Batu Ferringhi, Malaysia, pp. 108-111

[110] Ye J and Yang W Q (2013), Evaluation of Electrical Capacitance Tomography Sensors for Concentric Annulus, *IEEE Sensors Journal*, 13(2), pp. 446–456